

UNCLASSIFIED

AD NUMBER
ADB283518
NEW LIMITATION CHANGE
TO Approved for public release, distribution unlimited
FROM Distribution authorized to U.S. Gov't. agencies only; Proprietary Info.; Jul 2001. Other requests shall be referred to U.S. Army Medical Research and Materiel Command, 504 Scott St., Ft. Detrick, MD 21702-5012.
AUTHORITY
USAMRMC ltr, dtd 28 July 2003

THIS PAGE IS UNCLASSIFIED

AD _____

Award Number: DAMD17-99-1-9227

TITLE: Prediction of Malignancy in Breast Tumors Using Diffusion Weighted Magnetic Resonance Imaging

PRINCIPAL INVESTIGATOR: Paula J. Gareau, Ph.D.
Brian K. Rutt, Ph.D.

CONTRACTING ORGANIZATION: The John P. Roberts Research Institute
London, Ontario, Canada N6A 5K8

REPORT DATE: July 2001

TYPE OF REPORT: Annual Summary

PREPARED FOR: U.S. Army Medical Research and Materiel Command
Fort Detrick, Maryland 21702-5012

DISTRIBUTION STATEMENT: Distribution authorized to U.S. Government agencies only (proprietary information, Jul 01). Other requests for this document shall be referred to U.S. Army Medical Research and Materiel Command, 504 Scott Street, Fort Detrick, Maryland 21702-5012.

The views, opinions and/or findings contained in this report are those of the author(s) and should not be construed as an official Department of the Army position, policy or decision unless so designated by other documentation.

20021001 032

NOTICE

USING GOVERNMENT DRAWINGS, SPECIFICATIONS, OR OTHER DATA INCLUDED IN THIS DOCUMENT FOR ANY PURPOSE OTHER THAN GOVERNMENT PROCUREMENT DOES NOT IN ANY WAY OBLIGATE THE U.S. GOVERNMENT. THE FACT THAT THE GOVERNMENT FORMULATED OR SUPPLIED THE DRAWINGS, SPECIFICATIONS, OR OTHER DATA DOES NOT LICENSE THE HOLDER OR ANY OTHER PERSON OR CORPORATION; OR CONVEY ANY RIGHTS OR PERMISSION TO MANUFACTURE, USE, OR SELL ANY PATENTED INVENTION THAT MAY RELATE TO THEM.

LIMITED RIGHTS LEGEND

Award Number: DAMD17-99-1-9227
Organization: The John P. Robarts Research Institute

Those portions of the technical data contained in this report marked as limited rights data shall not, without the written permission of the above contractor, be (a) released or disclosed outside the government, (b) used by the Government for manufacture or, in the case of computer software documentation, for preparing the same or similar computer software, or (c) used by a party other than the Government, except that the Government may release or disclose technical data to persons outside the Government, or permit the use of technical data by such persons, if (i) such release, disclosure, or use is necessary for emergency repair or overhaul or (ii) is a release or disclosure of technical data (other than detailed manufacturing or process data) to, or use of such data by, a foreign government that is in the interest of the Government and is required for evaluational or informational purposes, provided in either case that such release, disclosure or use is made subject to a prohibition that the person to whom the data is released or disclosed may not further use, release or disclose such data, and the contractor or subcontractor or subcontractor asserting the restriction is notified of such release, disclosure or use. This legend, together with the indications of the portions of this data which are subject to such limitations, shall be included on any reproduction hereof which includes any part of the portions subject to such limitations.

THIS TECHNICAL REPORT HAS BEEN REVIEWED AND IS APPROVED FOR PUBLICATION.

Carole B. Christian

6/11/02

REPORT DOCUMENTATION PAGE

Form Approved
OMB No. 074-0188

Public reporting burden for this collection of information is estimated to average 1 hour per response, including the time for reviewing instructions, searching existing data sources, gathering and maintaining the data needed, and completing and reviewing this collection of information. Send comments regarding this burden estimate or any other aspect of this collection of information, including suggestions for reducing this burden to Washington Headquarters Services, Directorate for Information Operations and Reports, 1215 Jefferson Davis Highway, Suite 1204, Arlington, VA 22202-4302, and to the Office of Management and Budget, Paperwork Reduction Project (0704-0188), Washington, DC 20503

1. AGENCY USE ONLY (Leave blank)		2. REPORT DATE July 2001	3. REPORT TYPE AND DATES COVERED Annual Summary (1 Jul 00 - 30 Jun 01)	
4. TITLE AND SUBTITLE Prediction of Malignancy in Breast Tumors Using Diffusion Weighted Magnetic Resonance Imaging			5. FUNDING NUMBERS DAMD17-99-1-9227	
6. AUTHOR(S) Paula J. Gareau, Ph.D.				
7. PERFORMING ORGANIZATION NAME(S) AND ADDRESS(ES) The John P. Robarts Research Institute London, Ontario, Canada N6A 5K8 E-mail: pgareau@irus.ri.on.ca			8. PERFORMING ORGANIZATION REPORT NUMBER	
9. SPONSORING / MONITORING AGENCY NAME(S) AND ADDRESS(ES) U.S. Army Medical Research and Materiel Command Fort Detrick, Maryland 21702-5012			10. SPONSORING / MONITORING AGENCY REPORT NUMBER	
11. SUPPLEMENTARY NOTES				
12a. DISTRIBUTION / AVAILABILITY STATEMENT Distribution authorized to U.S. Government agencies only (proprietary information, Jul 01). Other requests for this document shall be referred to U.S. Army Medical Research and Materiel Command, 504 Scott Street, Fort Detrick, Maryland 21702-5012.				12b. DISTRIBUTION CODE
13. ABSTRACT (Maximum 200 Words) The purpose of this research is to develop a non-invasive predictor of malignancy in breast tumors using novel magnetic resonance imaging (MRI) techniques. The hypothesis is that the spatial distribution of microvasculature around a breast lesion is specific for malignancy and can be reliably measured by a completely non-invasive MRI method. This hypothesis is being tested by: 1) The design and construction of ultra-high gradient coils for MRI. 2) The implementation of advanced MRI pulse sequences for mapping of microvascular parameters 3) The correlation of MRI-derived vascular parameters (diffusion and perfusion) with histological parameters (tumor grade and microvessel density) in an animal model of human breast cancer.				
14. SUBJECT TERMS Breast Cancer, magnetic resonance imaging, angiogenesis, microvessel density, high strength gradient coils, diagnosis				15. NUMBER OF PAGES 60
				16. PRICE CODE
17. SECURITY CLASSIFICATION OF REPORT Unclassified	18. SECURITY CLASSIFICATION OF THIS PAGE Unclassified	19. SECURITY CLASSIFICATION OF ABSTRACT Unclassified	20. LIMITATION OF ABSTRACT Unlimited	

FOREWORD

Opinions, interpretations, conclusions and recommendations are those of the author and are not necessarily endorsed by the U.S. Army.

___ Where copyrighted material is quoted, permission has been obtained to use such material.

___ Where material from documents designated for limited distribution is quoted, permission has been obtained to use the material.

___ Citations of commercial organizations and trade names in this report do not constitute an official Department of Army endorsement or approval of the products or services of these organizations.

X In conducting research using animals, the investigator(s) adhered to the "Guide for the Care and Use of Laboratory Animals," prepared by the Committee on Care and use of Laboratory Animals of the Institute of Laboratory Resources, national Research Council (NIH Publication No. 86-23, Revised 1985).

___ For the protection of human subjects, the investigator(s) adhered to policies of applicable Federal Law 45 CFR 46.

___ In conducting research utilizing recombinant DNA technology, the investigator(s) adhered to current guidelines promulgated by the National Institutes of Health.

___ In the conduct of research utilizing recombinant DNA, the investigator(s) adhered to the NIH Guidelines for Research Involving Recombinant DNA Molecules.

___ In the conduct of research involving hazardous organisms, the investigator(s) adhered to the CDC-NIH Guide for Biosafety in Microbiological and Biomedical Laboratories.

Paula Goren March 4, 02
PI - Signature Date

Table of Contents

Cover	
SF 298	2
Foreword	3
Table of Contents	4
Introduction	5
Body	6
Key Research Accomplishments	9
Reportable Outcomes	10
Conclusions	11
Appendices	15

Introduction

X-ray mammography is currently the clinically accepted modality for breast cancer screening. Mammography, however, is particularly unreliable and recent trials have shown that 70-80% of mammographically indeterminate lesions that progress to surgical biopsy are benign.¹⁻⁴ Development of an accurate, non-invasive imaging test with low false negative rates would allow reduction of the two step process of surgical biopsy followed by surgical lesion removal to a single step, as well as providing a tool for guiding treatment decisions. It may be possible to achieve this through the development of a non-invasive technique that measures microvessel density. Tumour progression is known to be dependent on the ability to stimulate the growth of new blood vessels that supply nutrients and oxygen to the expanding tumour. Based on recent studies that indicate that the onset of angiogenesis can occur before a tumour reaches its maximum diffusion-limited growth potential (1-2 mm diameter) and may occur well before the switch to a malignant phenotype,⁵⁻¹⁵ it has been hypothesized that the characteristic new vessel growth associated with tumour angiogenesis should allow differentiation between malignant and benign breast lesions.¹⁶⁻²¹ The purpose of this research is to develop a non-invasive predictor of malignancy through the design and preliminary validation of a new form of magnetic resonance imaging (MRI) called the IntraVoxel Incoherent Motion (IVIM) method which utilises high main magnetic field strength and ultra-strong magnetic field gradients. This technology will permit completely non-invasive, quantitative characterization of tumour microvasculature at high spatial resolution over the entire breast.

Body

Hardware Development

A high strength gradient coil has been designed. The prototype coil was built with an inner diameter of 5 cm, which is ideal for mice. A second coil has now been built that is more suitable for rats. This coil has an inner diameter of 24 cm, which can accommodate a rat plus the equipment used to monitor the animal. The maximum gradient strength achievable with this coil is 300 mT/m, which is almost ten times greater than typical clinical systems and is sufficient for the high-resolution imaging experiments proposed in this grant. Testing of the coil on a 1.5 Tesla (T) clinical MRI system is nearly completed. It was found that wire density and power dissipation considerations required that the coil be constructed in a multilayer configuration. Details regarding the design and construction of the coil are given in the paper²⁷ in Appendix I.

Pulse Sequence Development

An IVIM pulse sequence has been designed based on a standard diffusion-weighted imaging sequence. The sequence consists of a spin echo, echo planar imaging sequence with the addition of strong magnetic field gradients that cause the contrast in the images to be weighted based on the diffusion of water in the microvascular and extravascular compartments. We have incorporated a phase correction method that allows post-acquisition correction of the images for small-scale motion of the object being imaged.

A computer program has been written in an interactive windows environment that allows analysis of the diffusion-weighted images obtained with the IVIM pulse sequence. The program allows calculation of the diffusion coefficients either for each pixel in the images, or for the average values in a region of interest. Validation of the program has been performed using simulated data. Further validation of both the program and the IVIM sequence has been performed using phantoms that are spherical containers filled with water and acetone. The results obtained (see Appendix II) agree well with those found in the literature.

Validation of Microvascular Imaging

A tumour model has been implemented in rats using N-ethyl-N-nitrosourea (ENU). ENU is known to be a potent carcinogen that induces well vascularised mammary tumours in rats.²² This tumour model was chosen because a range of benign and malignant tumours develop depending on the dose of ENU administered and because the tumour morphology and angiogenic behavior closely mimic breast tumours in humans. Tumours have been successfully grown in rats using both high dose and low dose injections of ENU. IVIM images of the tumours have been obtained for each rat. High signal to noise ratios (SNR) are required in the images in order to observe the microvascular component of the measured signal. The mean SNR in the images of the tumours was 392 ± 126 , which was sufficient for this study.

Seven rats were sacrificed immediately after imaging of the tumour, and imaging was repeated on the sacrificed animal. The diffusion decay curves obtained pre-sacrifice were not mono-exponential, but rather, were at least bi-exponential. Sample decay curves for one tumour showing the diffusion decay pre- and post-sacrifice are shown in Appendix III, Figure 1. The magnitude of the diffusion coefficient corresponding to the fast decay in the pre-sacrifice curves was on the order of that expected for the microvascular blood flow. Post-sacrifice, the fast decay component disappeared, but the curves were not mono-exponential as was expected. An intermediate diffusion coefficient, or a diffusion rate intermediate to the pre-sacrifice low and high rates, was present post-sacrifice. A plot of the two diffusion coefficients versus the fractional volumes contributing to the coefficients for each of the seven tumours pre- and post-sacrifice is shown in Appendix III, Figure 2. These results suggested that while the fast decay component appears to be related to the flow of blood in the microvasculature, a third diffusion rate may be present.

Initially, the diffusion decay curves were acquired to a maximum b-value of 1000 s/mm^2 . In order to determine if a third diffusion rate was present, diffusion decay curves were acquired to a maximum b-value of 5000 s/mm^2 . The decay curves were fit using a linear non-negative least squares (NNLS) fitting algorithm. This algorithm does not require *a priori* knowledge of the number of components present in the decay curve, but rather chooses the number of components that best fits the data. A plot of the

Unpublished Results – Please Protect

diffusion coefficients versus the fractional volumes contributing to the coefficients obtained using the NNLS algorithm for four tumours pre- and post-sacrifice is shown in Appendix III, Figure 3. The NNLS algorithm found three distinct diffusion decay coefficients in three of the four pre-sacrifice decay curves. In one presacrifice curve, only the low and intermediate diffusion coefficients were present. In all four post-sacrifice curves, only two coefficients were found – the low and intermediate values. The absence of the high diffusion coefficient in the post-sacrifice decay curves suggest that the high diffusion rate is due to the flow of blood in the microvasculature and that the IVIM method is capable of measuring the tumour microvasculature. Decay curves extending to a maximum of 5000 s/mm^2 have been collected from additional tumours, and analysis of this data is underway.

The tumours used in this study have been resected and pathology is currently being performed on each tumour to determine the degree of malignancy and the density of microvessels in the tumours. The pathological results will be correlated with the diffusion coefficients.

Unpublished Results – Please Protect

Key Research Accomplishments

- Design of a mouse-sized gradient coil with gradient strengths that exceed 2000 mT/m. (Approximately 50 to 100 times higher than typical clinical MRI systems.)
- Design and construction of a gradient coil with an inner diameter of 24 cm, which is large enough to accommodate a rat and animal monitoring equipment. Maximum gradient strengths achieved with this coil are 300 mT/m.
- Implementation of a fast IVIM pulse sequence that allows acquisition of diffusion weighted images with high signal to noise.
- Design and coding of a computer program that allows automated analysis of the diffusion weighted images for the calculation of diffusion coefficients.
- Validation of the MR pulse sequence analysis program using simulated data and images acquired from substances with known diffusion coefficients.
- Implementation of a breast tumour model in rats that produces tumours with a range of malignancies from benign to malignant.
- Acquisition of high signal to noise ratio, *in vivo*, diffusion weighted images of tumours in the rats using the IVIM method.
- Verification of three unique diffusion rates in the pre-sacrifice tumours.
- Verification that the highest diffusion rate is related to the flow of blood in the microvasculature.

Reportable Outcomes

Presentations and Publications

1. The design and construction of the gradient coils resulted in three peer-reviewed publications^{23,24,27} and two conference presentations.^{25,26} These three publications are appended.
2. The preliminary results of the acquisition and analysis of the images acquired from the animal tumour model were presented at the Era of Hope Meeting, Atlanta, June 8-12, 2000.
3. The results of multi-component MR diffusion imaging of ENU-induced breast tumors are being presented this year, first in March, as a poster presentation at the Workshop for Diffusion MRI and second, in May, as an oral presentation at the 10th Meeting of the International Society for Magnetic Resonance in Medicine. These abstracts are appended.
4. At least two additional papers are planned for submission after the analysis of the decay curves and the pathology of the resected tumours has been completed. It is projected that these papers will be submitted by September 2002.

Funding

Dr. Lanette Friesen-Waldner was recently awarded a postdoctoral traineeship from the Department of Defense U.S. Army Medical Research and Materiel Command's 2000 Breast Cancer Research Program. Grand Number BC000657. The research proposed in this traineeship is based on the preliminary data outlined in this report.

Conclusions

We designed a mouse-sized gradient coil and a gradient coil large enough to accommodate rats and animal monitoring equipment. Both coils achieve gradient strengths significantly higher than typical clinical MRI systems. Based on wire density and power dissipation considerations, we concluded that small coils with high gradient strengths, such as those required for high resolution IVIM imaging, require multi-layer configurations. The design for the coils constructed here should be scalable to a breast-sized coil. Such a coil will allow imaging of the human breast at resolutions that, until now, have been unattainable, thus allowing visualisation of very small lesions within the breast.

The IVIM pulse sequence was implemented on our 1.5T clinical MRI system. We are able to acquire IVIM images with high signal to noise ratios (at least 200). A computer program was written to analyse the IVIM images. The pulse sequence and analysis program were validated using substances with known diffusion coefficients.

An animal tumour model was implemented, and IVIM images of the tumours were acquired. We have shown that three diffusion rates exist in the tumours and that, in order to properly separate and accurately classify all three components, the diffusion decay curve must be sampled to a maximum b-value of at least 5000 s/mm². A multi-exponential fitting algorithm, such as NNLS, capable of more than bi-exponential fitting, must be used to determine accurately the diffusion coefficients from the decay curves. The largest of the three diffusion rates detected by the IVIM method is absent after cessation of blood flow. For this reason, we believe that this large diffusion rate arises from the tumour vasculature. Our results suggest that the tools developed here should be able to measure non-invasively the microvasculature in breast tumours. This would allow diagnosis of breast lesions *in vivo* and would also provide a means of following the effects of treatments, particularly treatment with anti-angiogenic pharmaceuticals.

References

1. Williams SM, Kaplan PA, Petersen JC, Lieberman RP. Mammography in women under age 30: Is there clinical benefit? *Radiology* **161**:49-51, (1986).
2. Ciatto S, Cataliotti L, Distante V. Nonpalpable lesions detected with mammography: Review of 512 consecutive cases. *Radiology* **165**:99-102 (1987).
3. Dershaw DD, Shank B, Reisinger S. Mammographic findings after breast cancer treatment with local excision and definitive irradiation. *Radiology* **164**:455-461 (1987).
4. Rosen PP, Braun DW, Kinne DG. The clinical significance of breast cancer. *Cancer* **46**:919-929 (1980).
5. Folkman J. What is the evidence that tumors are angiogenesis dependent? *JNCI* **82**:4-6 (1990).
6. Sutherland RM, McCredie JA, Inch WR. Growth of multicell spheroids in tissue culture as a model of nodular carcinomas. *JNCI* **46**:113-120 (1971).
7. Folkman J, Hochberg M. Self-regulation of growth in three dimensions. *J Exp Med* **138**:745-753 (1973).
8. Sutherland RM. Cell and environment interactions in tumour microregions: The multicell spheroid model. *Science* **240**:177-184 (1988).
9. Folkman J. Angiogenesis and breast cancer. *J Clin Oncol* **12**:441-443 (1994).
10. Guidi AJ, Fischer L, Harris JR, Schnitt SJ. Microvessel density and distribution in ductal carcinoma in situ of the breast. *JNCI* **86**:614-619 (1994).
11. Bose S, Lesseer ML, Norton L, Rosen PP. Immunophenotype of intraductal carcinoma. *Arch Pathol Lab Med* **110**:81-85 (1996).
12. Chodak GW, Haudenschild C, Gittes RF, Folkman J. Angiogenic activity as a marker of neoplastic and preneoplastic lesions of the human bladder. *Ann Surg* **192**:762-771 (1980).
13. Jensen HM, Chen I, DeVault MR, Lewis AE. Angiogenesis induced by "normal" human breast tissue: A probably marker for precancer. *Science* **218**:293-295 (1982).
14. Ziche M, Gullino PM. Angiogenesis and neoplastic progression in vitro. *JNCI* **69**:483-487 (1982).

15. Folkman J, Watson K, Ingber D, Hanahan D. Induction of angiogenesis during transition from hyperplasia to neoplasia. *Nature* **339**:58-61 (1989).
16. Lawson RN. Implications of surface temperatures in the diagnosis of breast cancer. *Can Med Ass J* **75**:309-310 (1956).
17. Sterns EE, Curtis A, Miller S. Thermography in breast diagnosis. *Cancer* **50**:323-325 (1982).
18. Amalric R, Girand D, Thommasin L. The persistently abnormal isolated infrared thermogram: The highest known risk of breast cancer. *Acta Thermographia* **3**:118-124 (1982).
19. El Yousef SJ. MRI of the breast. *Radiology* **150**:761-766 (1984).
20. Heywang SH, Wolf A, Pruss E, Hilbertz T, Eiermann W, Permanetter W. MRI of the breast with Gd-DTPA: Use and limitations. *Radiology* **171**:95-103 (1989).
21. Burns PN, Halliwell M, Wells PN, Webb AJ. Ultrasonic doppler studies of the breast. *Ultrasound in Medicine and Biology* **8**:127-143 (1982).
22. Stoica G, Koestner A, Capen C. Characterization of N-ethyl-N-nitrosourea induced mammary tumors in the rat. *Am J Pathol* **110**:161-167 (1983).
23. Maier CF, Nikolov HN, Chu KC, Chronik BA, Rutt BK. Practical design of a high-strength breast gradient coil. *MRM* **39**:392-401 (1998).
24. Chronik BA, Rutt BK. Constrained length minimum inductance gradient coil design. *MRM* **39**:270-278 (1998).
25. Rutt BK, Maier CVF. Design and construction of gradient coils for diffusion breast imaging. Invited presentation at the *Society of Magnetic Resonance Breast Imaging Workshop*, Washington D.C., June 24-25, 1995.
26. Chronik BA, Alejski A, Rutt BK. A 2000mT/m multilayer gradient coil for mouse imaging. *Proceeding of the International Society for Magnetic Resonance in Medicine* **7**:496 (1999).
27. Chronik BA, Rutt BK. Constrained Length Minimum Inductance Gradient Coil Design. *MRM* **44**:955-963 (2000).

Bibliography of Publications and Meeting Abstracts

Publications

28. Chronik BA, Rutt BK. Constrained Length Minimum Inductance Gradient Coil Design. *MRM* 44:955-963 (2000).
29. Maier CF, Nikolov HN, Chu KC, Chronik BA, Rutt BK. Practical design of a high-strength breast gradient coil. *MRM* 39:392-401 (1998).
30. Chronik BA, Rutt BK. Constrained length minimum inductance gradient coil design. *MRM* 39:270-278 (1998).

Meeting Abstracts

1. Friesen-Waldner L, **Gareau PJ**, Rutt BK. Multicomponent magnetic resonance diffusion imaging of breast tumors. Invited presentation at the 10th Meeting of the International Society of Magnetic Resonance in Medicine, Honolulu, USA May 18-24, 2002.
2. Friesen-Waldner L, **Gareau PJ**, Rutt BK. Multicomponent magnetic resonance diffusion imaging of breast tumors. Invited presentation at the *ISMRM Workshop on Diffusion MRI: Biophysical Issues*, Saint-Malo, France, March 10-12, 2002.
3. Friesen-Waldner L, **Gareau PJ**, Chronik B, Rutt B. Magnetic resonance imaging techniques for the examination of tumour vasculature. *Era of Hope, Department of Defense Breast Cancer Research Program Meeting* 1:191 (2000).
4. Chronik BA, Alejski A, Rutt BK. A 2000mT/m multilayer gradient coil for mouse imaging. *Proceeding of the International Society for Magnetic Resonance in Medicine* 7:496 (1999).
5. Rutt BK, Maier CVF. Design and construction of gradient coils for diffusion breast imaging. Invited presentation at the *Society of Magnetic Resonance Breast Imaging Workshop*, Washington D.C., June 24-25, 1995.

Appendices

Appendix I

Multi-Component Magnetic Resonance Diffusion Imaging of Breast Tumours

Lanette J. Friesen Waldner

Research Associate (Presenting Author)
Imaging Research Laboratories
The John P. Robarts Research Institute
P.O. Box 5015, 100 Perth Drive
London, Ontario
Canada N6A 5K8
Phone: (519)-663-5777 Ext. 34004
Fax: (519)-663-3403
Email: Lfriesen@irus.ri.ca

Paula J. Gareau

Scientist
Imaging Research Laboratories
The John P. Robarts Research Institute
P.O. Box 5015, 100 Perth Drive
London, Ontario
Canada N6A 5K8
Phone: (519)-663-5777 Ext. 34040
Fax: (519)-663-3403
Email: pgareau@irus.ri.ca

Brian K. Rutt

Scientist
Imaging Research Laboratories
The John P. Robarts Research Institute
P.O. Box 5015, 100 Perth Drive
London, Ontario
Canada N6A 5K8
Phone: (519)-663-5777 Ext. 35818
Fax: (519)-663-3403
Email: brutt@irus.ri.ca

Introduction

Breast cancer has the highest incidence of all cancers affecting women in both Canada and the United States. Despite significant gains made in characterizing the role of molecular biology and genetics in cancer progression, overall mortality rates from breast cancer have remained disturbingly constant over the past fifty years. Breast cancer is now the second leading cause of cancer death among women in both Canada and the United States [1, 2]. While X-ray mammography is the most effective breast screening method for older women, it is not clearly beneficial for younger women or women with dense breasts. The ability of mammography to diagnose is also particularly unreliable, which is evidenced by the fact that the majority of mammographically indeterminate lesions that progress to surgical biopsy are benign.

Tumor progression is known to be dependent on angiogenesis, the ability to stimulate the growth of new blood vessels that supply nutrients and oxygen to the expanding tumor. The density of microvessels in 'hotspots' in the periphery of invasive breast tumors has been shown to outperform lymph-node positivity as a predictor for the development of distant metastatic disease. Moreover, microvessel density is the only prognostic indicator that is a statistically significant predictor of overall survival for node-negative women [3, 4]. The development of new non-invasive imaging methods that can serially monitor microvessel density at high resolution over entire tumours, is of great importance. Both contrast-enhanced MR and color Doppler ultrasound imaging methods have been developed and applied to breast cancer diagnosis, but neither provides a direct measure of microvessel density [5, 6]. At present, there is no single non-invasive imaging method that produces quantitative maps of microvessel density.

Recent diffusion-weighted magnetic resonance imaging (DW-MRI) studies that sample the diffusion decay curve to large b-values ($\geq 5000 \text{ s/mm}^2$) have shown that more than one rate of diffusion (D) of water molecules is observed in tissue. The source of these multiple diffusion components has sparked much debate. In the mid 1980's, Le Bihan [7] suggested that at low b-values ($< 100 \text{ s/mm}^2$) another fast diffusion rate could be observed that arises from microvascular blood flow. The premise here is that microvascular blood flow can be modelled as a pseudo-diffusion process.

We have developed a new form of MR diffusion imaging (MRDI) which allows quantitative assessment of *both* the multi-exponential decay of water in tissue *and* the pseudo-diffusive motion of microcirculatory blood. We have chosen a breast tumour model for this study because pathological examination of breast tumours has shown that the density and distribution of microvessels is different in benign and malignant tumours.

Hypothesis

We hypothesize that the diffusion decay curve observed in breast tumours is at least tri-exponential and that a fast diffusion rate exists which arises from the microvasculature.

Methods:

Tumour Model: N-ethyl-N-nitrosourea (ENU) was injected intraperitoneally (180mg/kg body weight) into 30 days old Sprague-Dawley rats [8]. Vascularized mammary tumours developed spontaneously in approximately 90 days. The degree of malignancy, and the density and distribution of microvessels is dependent on the dose of ENU.

Imaging Protocol: Ten rats were anaesthetised using ketamine/xylazine. One rat had 2 tumours for a total of 11 tumours imaged. Imaging was performed on a 1.5T GE CV/i MRI system, 40mT gradient strength and a quadrature surface RF coil (4cm loops). Diffusion weighted (DW) images (single shot SE-EPI, TE/TR=111.3ms/2500ms, FOV=16x8cm, matrix=80x80, slice thickness=5.0mm, 8 averages) were acquired with 18 b-values (0, 30, 61, 90, 139, 239, 366, 529, 736, 1000, 1500, 2000, 2500, 3000, 3500, 4000, 4500, 5000s/mm²) according to the method of Stejskal and Tanner [9]. Diffusion encoding was performed along the X, Y, and Z axes to obtain the trace of the diffusion tensor. Rats were euthanised in the magnet and DW images re-acquired immediately.

Analysis: S_i/S_0 was calculated pixel-by-pixel for each b where S_i = signal at the i^{th} b-value ($i=0, \dots, 17$). The diffusion decay curve (S_i/S_0 vs b) was determined for a region of interest encompassing the entire tumour, and was fit using the non-negative, least squares (NNLS) algorithm. NNLS produces the minimal distribution of D's that best fits the multi-exponential decay without the need for *a priori* assumptions of the number of D's present, but does require knowledge of the range of D values. Seventy-five logarithmically spaced values were chosen between 0.10×10^{-3} and 50.0×10^{-3} mm²/s.

Results

Signal to noise ratios (SNRs) in the b=0 images (for voxels in the tumour) ranged from 214 to 636 (mean 395). Representative diffusion decay curves for one tumour, pre- and post-sacrifice are shown in Figure 1. NNLS fitting of the diffusion decay curves identified three diffusion components (closed symbols in Figure 2) in 7 of the 11 pre-sacrifice curves, and two components in the remaining 4 curves. Post-sacrifice (open symbols in Figure 2), 9 of the 11 tumours exhibited only the two lower diffusion rates. In the remaining 2 tumours, D_3 was detected post-sacrifice, but the corresponding fractional amplitudes (f_3) were less than 0.01. Table 1 contains the mean values and standard deviations for the D's and f's. Paired student t-tests comparing pre- and post-sacrifice values for D_1 , D_2 , f_1 , and f_2 showed no significant differences ($p > 0.1$).

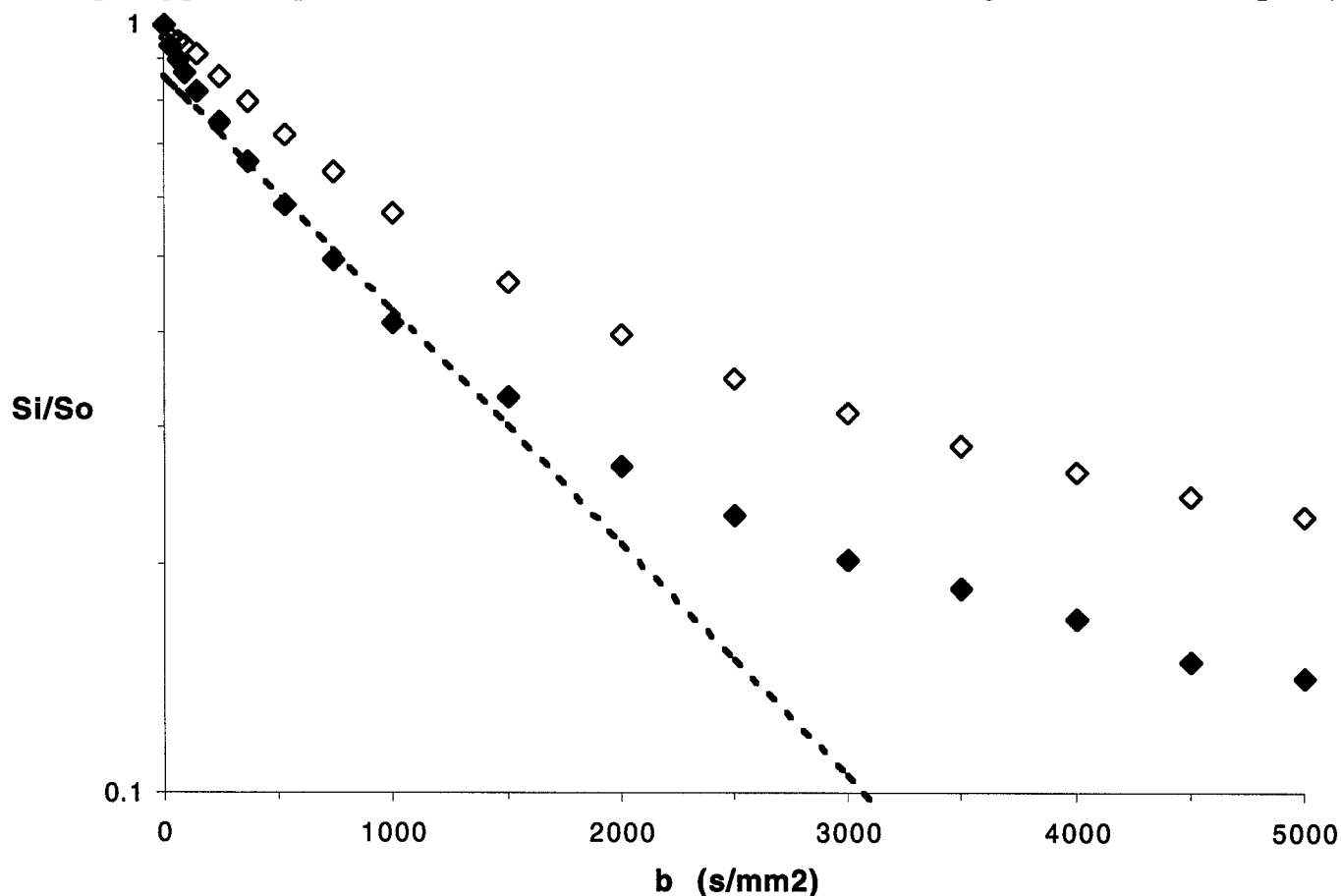


Figure 1: Diffusion decay curves for one animal, pre- (closed diamonds) and post- (open diamonds) sacrifice. The dashed line represents a theoretical mono-exponential decay.

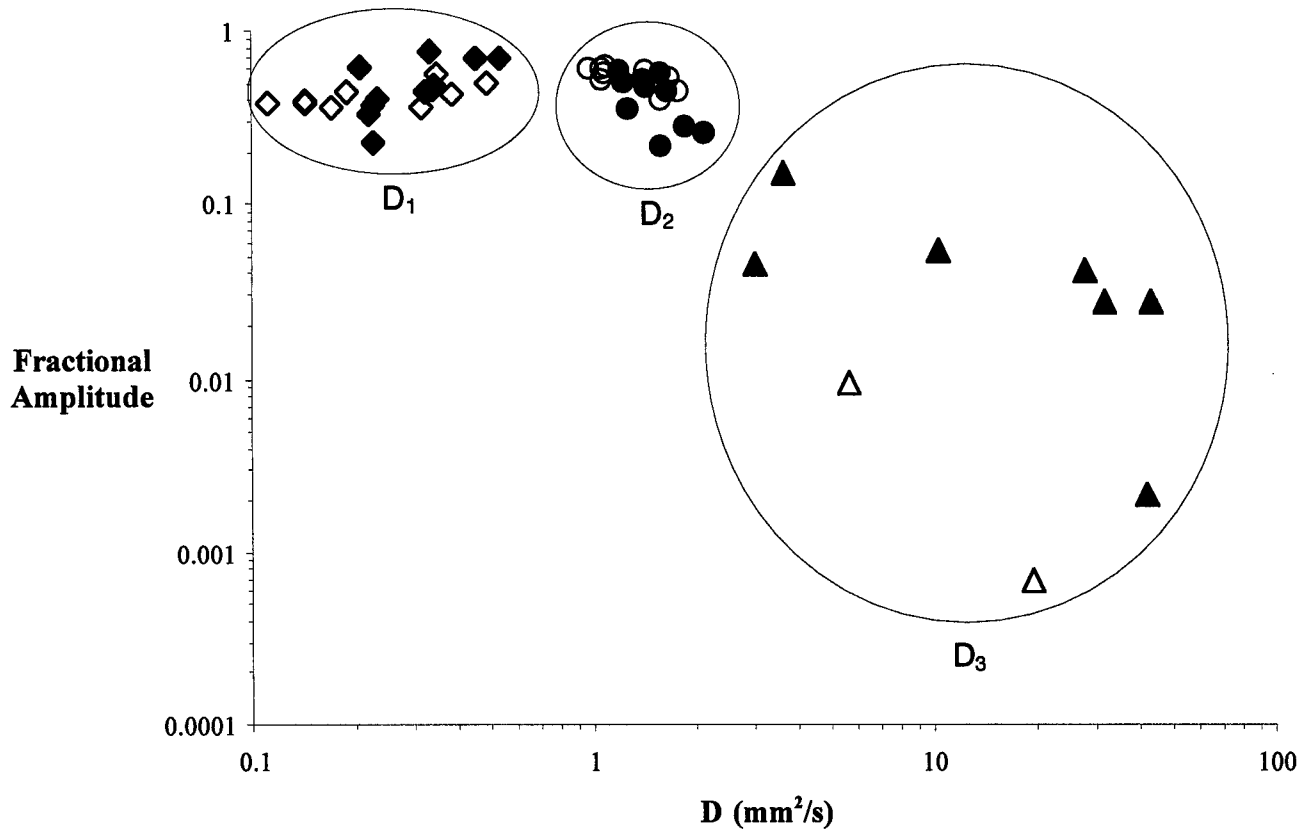


Figure 2: Diffusion coefficients obtained from 11 tumours pre- (closed symbols) and post-sacrifice (open symbols).

Table 1: Mean diffusion coefficients (D , in units of $\times 10^{-3} \text{mm}^2/\text{s}$) and fractional amplitudes (f) \pm standard deviations pre- and post-sacrifice.

	D_1	D_2	D_3	f_1	f_2	f_3
Pre	0.31 ± 0.10	1.50 ± 0.30	22.99 ± 17.27	0.51 ± 0.17	0.44 ± 0.14	0.05 ± 0.05
Post	0.26 ± 0.12	1.30 ± 0.30	12.56 ± 9.81	0.50 ± 0.19	0.52 ± 0.09	0.00 ± 0.01

Discussion

The fraction of the total volume of a tumour that is composed of microvasculature is relatively low ($<20\%$) and is dependent on the degree of malignancy of the tumour. Due to this low fractional volume, it is necessary to achieve very high SNRs in order to detect and quantify accurately the pseudo-diffusion of blood flow in the microvasculature. The high SNRs obtained in this study show that the diffusion decay curve is more than bi-exponential (Figure 1).

If D_3 originates from the blood flow in the microvasculature, this component should disappear post-sacrifice. This was observed, by and large. In two of the tumours (Figure 2), a third diffusion component persisted post-sacrifice; however, the corresponding fractional amplitudes, f_3 , were low enough to be attributed to noise in the decay curves at low b -values. Due to the disappearance of D_3 when the only change in the tumour is the cessation of blood flow, we conclude that this fast diffusion rate arises from the microcirculatory blood flow.

No significant changes were observed in D_1 , D_2 , f_1 , and f_2 post-sacrifice. In brain tissue, cellular micro-architecture begins to change immediately post-ischemia and it is these changes that are believed to give rise to changes in the diffusive properties of water that can be observed using diffusion weighted MRI. Unlike brain tissue, cellular swelling and breakdown of cellular membranes in breast tumours does not begin until several hours post-cessation of blood flow. In this study, post-sacrifice scanning was completed before one hour post-sacrifice. For this reason, it is not surprising that no significant changes were observed in the two lowest diffusion rates and fractional amplitudes post-sacrifice.

Pathological analysis of the samples will be performed to determine if a correlation exists between the diffusion coefficients and degree of malignancy.

Conclusions

Our MRDI method, combined with the NNLS fitting algorithm, detects three diffusion components in breast tumours. We have presented evidence that the large diffusion coefficient arises from the microcirculatory blood flow. The ability to detect the microvasculature in breast tumours may lead to a non-invasive method of diagnosing tumour malignancy. Studies are continuing with respect to assigning the other two D components.

Acknowledgements

The authors wish to thank Jamie Thomas and Adam Rankin for their assistance. This work was supported by the U.S. Army Medical Research and Materiel Command and the Natural Sciences and Engineering Research Council of Canada.

References

- 1) American Cancer Society: <http://www2.cancer.org/epi>.
- 2) National Cancer Institute of Canada: **Canadian Cancer Statistics 2000**, Toronto, Canada, 2000.
- 3) Weidner N *et al.* JNCI 1992, **84**:1875.
- 4) Fox SB *et al.* Breast Cancer Research and Treatment 1994, **29**:109.
- 5) Nunes LW *et al.* Radiology 1997, **202**:833.
- 6) Lee WJ *et al.* Ann Surg Oncol 1995, **2**:246.
- 7) D. Le Bihan *et al.* Radiology 1988, **168**:497.
- 8) G. Stoica *et al.* Am J Pathol 1983, **110**:161.
- 9) E. Stejskal and J. Tanner. J Chem Phys 1965, **42**:28

Practical Design of a High-Strength Breast Gradient Coil

Cynthia F. Maier, Hristo N. Nikolov, Kenneth C. Chu, Blaine A. Chronik, Brian K. Rutt

A high-strength three-axis local gradient coil set was constructed for MRI of the breast. Gradient fields with good uniformity (<10% deviation from the desired gradient) over most of the volume required for breast imaging were generated with efficiencies of up to 3.3 mT/m/A. The coils will allow diffusion breast imaging in clinically acceptable examination times. The electrical design, water cooling system, and fabrication techniques are described. Preliminary tests of the coil included images of a grid phantom and diffusion measurements in a short- T_2 agarose gel phantom.

Key words: breast imaging; diffusion imaging; gradient coils.

INTRODUCTION

In this paper, we present a specialized gradient coil design for breast imaging and demonstrate the utility of this coil for performing MR diffusion imaging with short-duration, high-strength gradient pulses. Sensitization of an MR pulse sequence to motion can be achieved using conventionally available gradient hardware; however, measurement of water diffusion (or slow flow in microvessels) with this hardware requires long echo times to achieve large gradient moments and therefore suffers from significant signal loss due to T_2 relaxation and system nonidealities. In addition, increasing the time between motion-sensitizing gradient pulses allows more macroscopic motion to occur in this interval, resulting in pixel misregistration, motion-induced ghost artifacts, and diffusion/flow measurement artifacts. Higher-strength gradients will allow adequate sensitization to small motions (i.e., large gradient moments) with very short, high-amplitude gradient pulses and minimal time delay between these pulses.

METHODS

The gradient coil assembly was designed in a cylindrical geometry, with each gradient coil built onto a separate cylindrical former. The three-axis coil set was composed of concentrically nested coils, oriented vertically such that their common axis was transverse to the main field as shown in Fig. 1. Space restrictions within the magnet bore require that the coils be as short as possible in the vertical direction to allow a patient to lie comfortably above the top edge of the cylinders. Unfortunately, decreasing the height of the coils (relative to their diame-

ters) makes the creation of uniform gradients within the coils much more difficult. To satisfy the competing demands of good gradient uniformity and height restrictions, we used an aspect ratio of approximately 1:1 for our cylindrical coils. The height of the complete coil assembly was 16 cm, leaving 34-cm clearance in the vertical direction in our General Electric (GE) Signa Horizon scanner (General Electric Medical Systems, Milwaukee, WI), and the largest coil diameter was 21.6 cm.

To generate the winding densities required for high gradient strengths, relatively small-diameter wire (AWG no. 20) was used to construct the coils. The resistivity of this wire is high, requiring an active cooling system to remove heat and maintain temperatures inside the coils within a range comfortable for the patient. Water-cooling jackets with very thin walls were sandwiched between the gradient coils, so that resistive heat could be removed efficiently while maintaining the compact construction of the coil assembly. A dedicated RF coil and shield were mounted inside the innermost gradient coil with an approximately 1.3-cm space between the RF coil and closest gradient coil. The entire assembly is depicted in cross-section in Fig. 2.

Electrical Design

The highly efficient quadrupolar current distribution (1–3) was used to provide gradients in B_z along both the x and z directions (G_x and G_z). This current density varies azimuthally as $\cos(2\theta)$ and is entirely directed along the axial direction on the surface of the cylindrical former. Discrete wire positions approximating the continuous quadrupolar current density were calculated by sampling the current density $\cos(2\theta)$ at θ_i such that $\cos(2\theta_{i+1}) - \cos(2\theta_i)$ was constant. A schematic diagram showing this ideal wire distribution is given in Fig. 3a. The current pattern in Fig. 3a is nonphysical in that the current is discontinuous at the ends of the coil, and therefore, connecting paths between the wires ("return wires") must be provided. In most imaging applications in which local gradient coils have been used previously, the volume to be imaged has been located at the center of the coil, and placing return paths near the ends of the cylinder had a minimal effect on the desired field within the object. For breast imaging applications, the required location for the region of good gradient uniformity is near the top edge of the coils and a conventional return wire arrangement would corrupt the gradient field uniformity within this volume. We chose to place the return wire components instead on horizontal plates at the tops and bottoms of the coils. Close to the cylinders on the plates, the return paths were extended along the z direction for at least 5 cm (no B_z is generated by current in the z direction). The bottom set of return wires for the G_z coil were strung across the bottom of the cylinder in the z direction. The quadrupole current distribution for G_x is rotated 45° with respect to G_z , and the return wires for G_x could not be strung in the z direction; therefore, these wires were located on a horizontal plate.

MRR 39:392-401 (1998)

From the Departments of Medical Biophysics and Diagnostic Radiology, University of Western Ontario, London, Ontario, Canada; and Tom Lawson Family Imaging Research Laboratories, John P. Robarts Research Institute, London, Ontario, Canada.

Address correspondence to: B. K. Rutt, Ph.D., Department of Diagnostic Radiology, University Hospital, London, Ontario, Canada N6A 5A5.

Received March 10, 1997; revised August 21, 1997; accepted August 22, 1997.

This work was supported by the Breast Cancer Society of Canada and the Canadian Breast Cancer Research Initiative, National Cancer Institute of Canada. C.M. was supported by a W.T. McEachern Scholarship and by a U.S. Army Breast Cancer Predoctoral Fellowship.

0740-3194/98 \$3.00

Copyright © 1998 by Williams & Wilkins

All rights of reproduction in any form reserved.

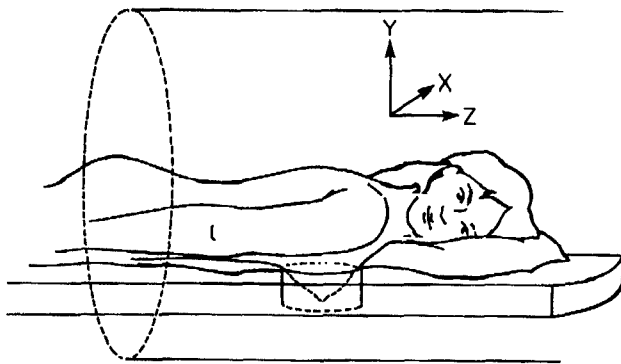


FIG. 1. Schematic showing orientation of local breast gradient coil in magnet.

The design of the G_y gradient makes use of the fact that $\nabla \times B = 0$ throughout any region in which the current density is 0. This means that a transverse gradient coil with its axis along z (the conventional orientation) can be turned 90° about the x axis so that its axis is along the y direction and used to produce a gradient in B_z along the y direction. We designed a transverse gradient coil in the conventional orientation using the target field method (4, 5) and then rotated the coil to produce G_y . Although a wide range of breast sizes exist, we defined an average volume of interest (VOI) for breast imaging (by comparison with commercially available breast RF coils) as a cylindrical volume with length equal to 60% of the coil height (11.5 cm), a diameter equal to 90% of the RF coil diameter (13.5 cm), and location flush with the top surface of the gradient coil assembly. The target field coil was designed to have its region of good gradient uniformity centered on this VOI. This design consisted of only two sets of closed current loops (Fig. 3b). For the target-field coil in its conventional orientation with its axis along z , the desired gradient is created almost entirely by the current in half of the wire loops only (the "primary" component of the loop as indicated in Fig. 3b), and return wires are an intrinsic part of the design (labeled "return" in Fig. 3b). For this coil, only one set of "return paths" is required for current continuity, and in the vertical orien-

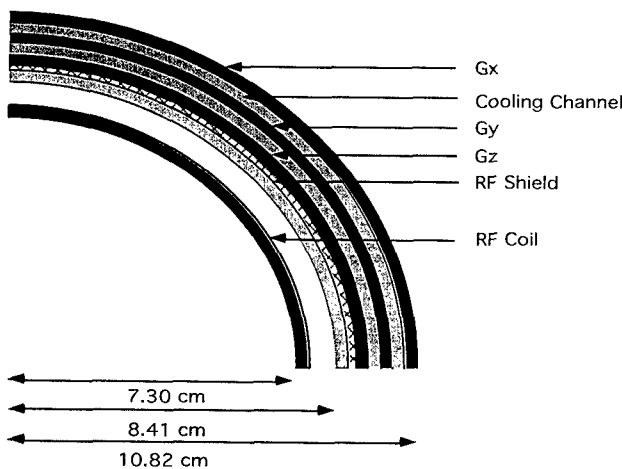


FIG. 2. Cross-section of complete gradient coil assembly showing location of RF coil and water-cooling modules.

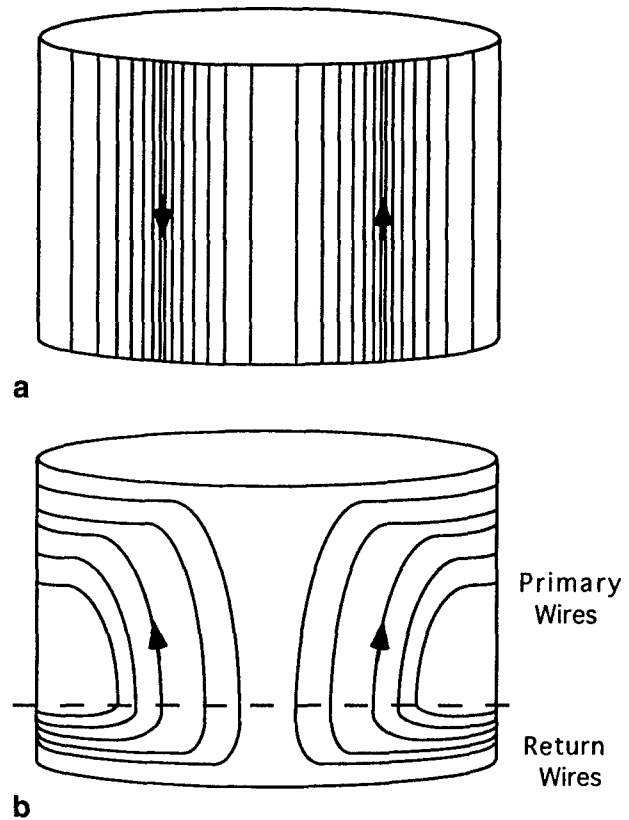


FIG. 3. (a) Quadrupolar current density with 56 windings. (b) Target-field-design transverse coil. The "primary wire" component is almost entirely responsible for generation of the transverse gradient for the conventional coil orientation with its axis along z .

tation, these wires are located at the bottom of the cylinder. In our coil design, such a large number of loops was required to generate the desired gradient efficiency that these return wires would have occupied a large fraction of the space available on the surface of the cylinder. Due to the strict limitations on coil height, we believed that this space could be used more efficiently if only the primary component of the coil design was present on the cylinder itself and the return paths were located on a horizontal plate as for the quadrupole coils. A complication that arises from truncating the wire pattern in the vertical dimension in this way is that the reciprocity relations from Maxwell's equations no longer hold for a nonphysical current distribution (i.e., $\nabla \times B \neq 0$ for a current distribution with nonzero divergence). This means that the gradient field calculated for the truncated design is not identical in the conventional and transverse orientations unless the return wires are included in the calculation. We shall see in the Results section that the truncated coil in the transverse orientation has both an increased gradient efficiency compared to the full design for the same coil height and, additionally, the region of acceptable gradient uniformity (<20% deviation from uniformity) is significantly larger for the truncated coil.

One undesirable side effect that arises from locating the return wires on horizontal surfaces is that the torque on the coils from interaction with the main static field is greatly increased. This effect is significant. For our 1.5-T

magnet, current is only supplied when the coils are positioned near the central, highly homogeneous region of the magnet (typical clinical imaging systems have a 50-cm-diameter spherical volume of better than 10 ppm B_0 uniformity) and the upward (downward) force on the $+z$ ($-z$) half of the horizontal plate for the G_z coil is approximately 15 N/A (3.5 lb/A) increasing linearly with applied current. As the gradients are switched, the effect of this force is to create an alternating torque of approximately 3 Nm/A in size. For many pulse sequences, the direction of the current is switched rapidly, resulting in a torque that alternates direction rapidly and causes significant vibrational stress on the coils. For our preliminary experiments, a temporary coil support was constructed from wood- and glass-reinforced phenolic. The horizontal plates were rigidly attached to the support, and the support structure itself served to mount the coil assembly inside the bore of the imager, thereby preventing any bulk coil motions that could arise from the magnetic forces on the wires. The wires themselves were potted securely in the milled grooves using epoxy and were prevented from vibrating loose from these grooves by the next adjacent layer of cooling channels, since all layers were tightly sandwiched together.

Coil Construction

To produce high gradient efficiencies, it is advantageous to use the maximum number of wires possible. This number is constrained in an obvious way by the wire diameter, minimum spacing between wires, and circumference of the cylindrical former. To obtain the desired gradient efficiencies for these coils, it was necessary to use relatively small wires (AWG no. 20) with a diameter of ~ 1 mm and an interwire spacing of 0.5 mm. The G_x (outermost) coil was wound with a single length of wire such that 216 axially directed segments generated the required current density, and for the G_z (innermost) coil, 200 axially directed segments were wound. For the middle coil (G_y), constraining the closest separation of the wires to be 0.5 mm allowed 48 loops per side. For all three coils, the wire paths were milled (numerically controlled) into the surface of polycarbonate/acrylic formers. Wire was then wound into these grooves and epoxied in place. Figure 4a shows the constructed G_x coil, complete with horizontal plates after winding with (dielectric) insulated copper wire. The upper plates were curved downward at the superior and inferior ends to provide a more comfortable structure for patient support. Figure 4b shows the middle coil (G_y) before assembly of the complete gradient coil unit.

The resistivity of the small-diameter wire used to construct the coils is relatively high, increasing from 33.3 m Ω /m at room temperature to 40.5 m Ω /m at 75°C (our specified upper limit on temperature at the wire). The additional length of wire required to extend the return paths away from the main cylinders also contributed to high coil total resistances. Since high root-mean-squared (RMS) currents are required for the desired imaging applications, the power dissipated by the coils is significant (~ 1250 W for one coil @ 25A RMS). In a mock-up of one quadrant of a coil, when a 25A RMS current was applied

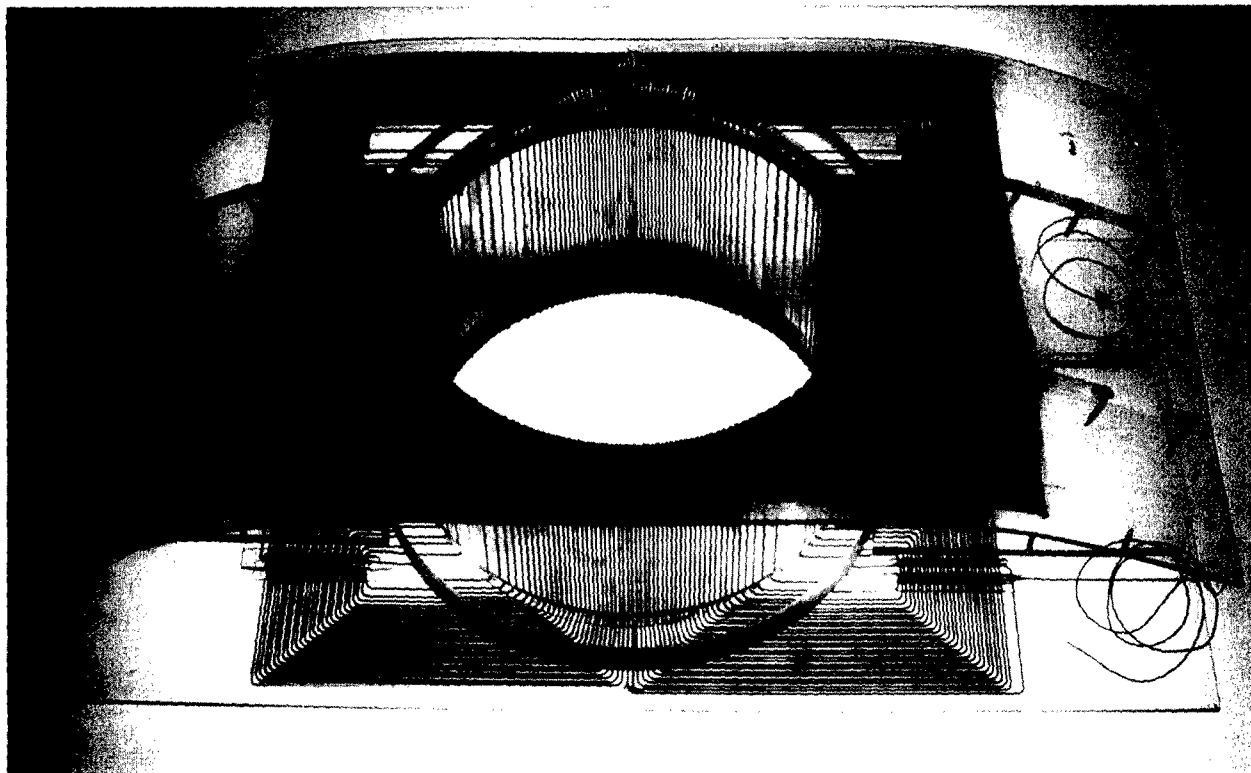
with no cooling, the temperature of the quadrant rose from 10°C to 100°C in 2.5 minutes. With air cooling only, a temperature rise from 10°C to 35°C in 4 minutes was observed. A more efficient cooling system was therefore required to ensure patient safety.

Water is one of the most efficient and economical cooling fluids available. Its heat capacity ($C_p = 4.18$ J/g/°C) is approximately two times higher than other commonly available cooling fluids such as hydrocarbon oils (e.g., ethylene glycol). Assuming that all heat generated is transferred to the cooling water and the maximum allowable temperature rise of the water is 5°C, a water flow of 3.6 liter/min is required to remove 1250 W of heat. Conventionally, water-cooling channels for gradient coils are constructed from copper tubing. For a compact gradient coil set, the competing demands of space limitations and the requirement of a large cooling channel cross-section to ensure adequate volume flow rates necessitated the design of a novel cooling system. We designed this cooling system in separate modules, each module corresponding to a quadrant of a single gradient coil. Each module consisted of a skeleton of cooling channel spacers that were milled from a 3.0-mm-thick polycarbonate sheet. This was covered on both sides with a very thin (0.25-mm-thick) polycarbonate film (GE Plastics, General Electric Company, Pittsfield, MA) to allow close thermal contact of the wires with the cooling water while ensuring electrical insulation. The film was bonded to the skeleton using ultraviolet-curing polyvinyl chloride-based bonding adhesive (Loctite 3311, Loctite Corporation, Mississauga, Canada). The tensile strength (to break) of the polycarbonate film was rated at 9000 psi, according to American Standards of Testing Materials (ASTM) D882, and the burst strength was 200 psi (ASTM D774). The modules were tested for flow uniformity and resistance to leaks by flowing water at 13 liter/min for >5 hours before permanent incorporation into the gradient coil structure. After incorporation into the gradient coil set, the modules were connected in parallel to lower the fluid resistance of the network of cooling channels and thereby allow increased water flow rates.

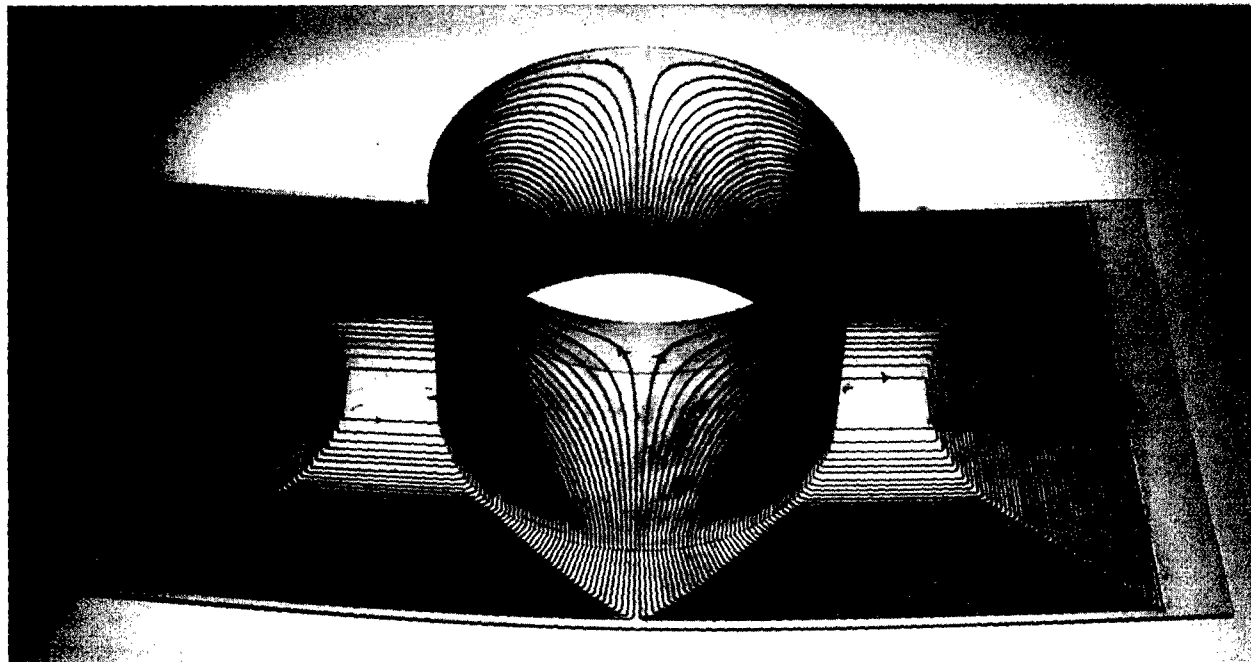
This design allowed very close thermal contact between the wires and water in the cooling channels (while maintaining electrical isolation) and also provided a large surface area over which heat could be transferred to the water. The ability to test the cooling channel integrity separate from the gradient coil structure was vital in ensuring no electrical shorting due to water leakage. An additional benefit of constructing the cooling system from polycarbonate is that no electrical currents can be created in this material, and it is therefore not susceptible to eddy current generation like some copper systems. Since the thickness of the cooling channel module was only 3.5 mm, the maximum total wall thickness of the gradient coil structure was less than 3 cm. The assembled gradient coil structure, including RF coil and water connections, is shown in Fig. 5.

RF Coil

Several cylindrical RF coil designs exist that can be used in a transverse geometry for imaging the breast (i.e., with



a



b

FIG. 4. (a) G_x quadrupole coil with 216 windings. (b) G_y coil showing placement of the "return wires" on a horizontal plate.

the coil axis perpendicular to the main magnetic field B_0). These coils, when oriented vertically, produce B_1 fields directed along either the horizontal x direction (e.g., saddle coils (6)) or along the vertical direction (e.g., solenoidal coils (7, 8)).

The construction of an RF coil for operation inside our breast gradient coils is a difficult problem, in that the

proximity of the RF coil to the gradient coils results in very strong inductive coupling and detuning of the RF coil (given that the gradient coil radius is constrained to be as small as possible for maximum efficiency). To determine the best RF coil design for our gradient coil set, two different RF coils were constructed and tested. The first coil constructed was a quadrature RF coil with

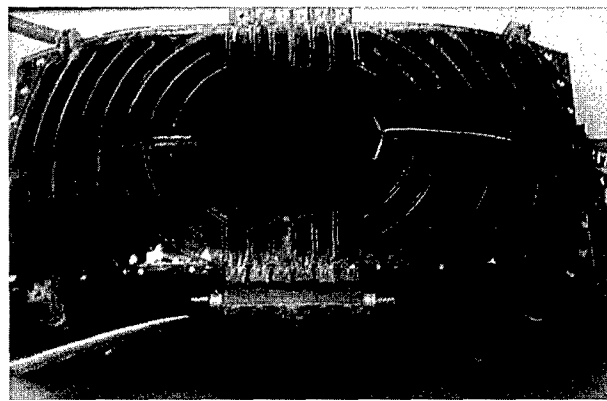


FIG. 5. Assembled gradient coil module showing RF coil and cooling channels.

two separate coils providing the perpendicular B_1 components. In this arrangement, a simple three-loop solenoidal coil provided the vertical mode, and a saddle coil built onto the same former provided the horizontal mode. The second coil constructed was a 16-rung high-pass birdcage RF coil designed for operation in a linear mode (recall that a birdcage coil cannot be used in quadrature mode in the vertical orientation because one of the modes would be parallel to B_0). We chose this design over a saddle-coil arrangement because of the superior uniformity of B_1 produced by the birdcage coil over the volume enclosed by the coil. A split cylindrical RF shield was constructed from fine copper screen and located immediately inside the smallest diameter gradient coil. The coils were tested for coupling to the gradient coils. The quality factors, Q , were measured, and the coil performances were compared.

Diffusion Imaging

Preliminary diffusion measurements were made using a short- T_2 phantom consisting of NiSO_4 -doped agarose gel ($T_2 = 60$ ms at 1.89 T) with a diffusion-sensitized spin-echo sequence (pulsed gradient spin-echo sequence (9)). Apparent diffusion coefficient (ADC) maps were calculated from a series of 10 diffusion-weighted images with diffusion b factors between 0 and 1000 s/mm^2 . Each of these images was the geometrical average of two images with equal diffusion-weighting but with opposite diffusion gradient polarity to remove the effects of diffusion-weighting cross-terms from interaction between the diffusion and imaging gradients (10). The ADC maps were obtained under three conditions: (1) using the standard whole-body manufacturer-supplied gradient coils for all imaging and diffusion-weighting gradients; (2) using our custom coils for all imaging and diffusion-weighting gradients, with the gradient strengths matched to those of the whole-body coils by applying an appropriately scaled current to the coils; and (3) using our custom coils for all imaging and diffusion-weighting gradients, with the imaging gradient strengths matched to those of the whole-body coils, but taking advantage of the increased gradient efficiency to apply higher strength, shorter diffusion-weighting gradients, thereby shortening the scan TE. In the first two experiments, the minimum TE required for

diffusion weighting of $b = 995$ s/mm^2 was TE = 80 ms (with diffusion gradient strength of 22 mT/m). TR was set to 600 ms, the matrix size for the scan was 256×128 , and the image size was 8×8 cm, for a total scan time of 2.5 minutes for each image (5 minutes for each b factor). Diffusion gradients were applied along the readout axis, x , for all experiments. For the third experiment, the TE was decreased to TE = 46 ms by increasing the strength of the diffusion-weighting gradient pulses by a factor of four (88 mT/m) to obtain much larger b factors with shorter diffusion pulses. All other parameters (including slice thickness) were matched to the first two experiments.

RESULTS

Coil Performance

The field produced by each of the three coils was calculated by direct numerical solution of the Biot-Savart Law for the wire paths, including return wire contributions. Calculated gradient efficiency for all three coils, together with the measured resistance and inductance, are summarized in Table 1. Contour plots of calculated gradient uniformity for the G_z quadrupole coil are shown in Fig. 6. Figure 6a shows the percentage deviation from gradient uniformity for a y - x plane through the center of the coils. A similar plot is shown in Fig. 6b for a x - z plane, transverse to the coil axis, at a height equal to the center of the VOI (i.e., located 5.9 cm below the top surface of the coils). These plots show the excellent gradient uniformity within the VOI that is predicted for the G_z coil. The gradient strength decreases near the ends of the coil, because the finite length of the coil causes a decrease in field strength. Similar results were obtained for the G_x gradient coil, with appropriate scaling for the number of wires and the coil radius. The performance of the modified target field G_y coil is shown in Figs. 6c and 6d. A larger deviation from gradient uniformity is present for this coil, compared to the G_x and G_z coils. This problem is inherent to any design for a G_y coil in the transverse orientation, since there is an additional gradient in the y direction due to the natural field fall-off that occurs as the ends of the coil are approached. To create a G_y coil with optimum gradient efficiency, we would like to maximize $|B_z|$ at both ends of the coil, with B_z a maximum in the $+z$ direction at one end of the coil, and a maximum in the $-z$ direction at the opposite coil end. The field fall-off inherent in this coil orientation works against the gradient we desire to create, since it necessarily results in a decrease in the magnitude of B_z as the coil ends are approached. Instead of working against the natural field fall-off toward the ends of the coil, we have designed a

Table 1
Coil Performance Characteristics

	Mean diameter (cm)	Efficiency (mT/m/A)	Inductance (μH)	Resistance (Ω)
G_x (quadrupole)	21.1	2.9	754	2.3
G_y (fingerprint)	19.5	1.7	829	2.6
G_z (quadrupole)	18.1	3.3	1024	1.9

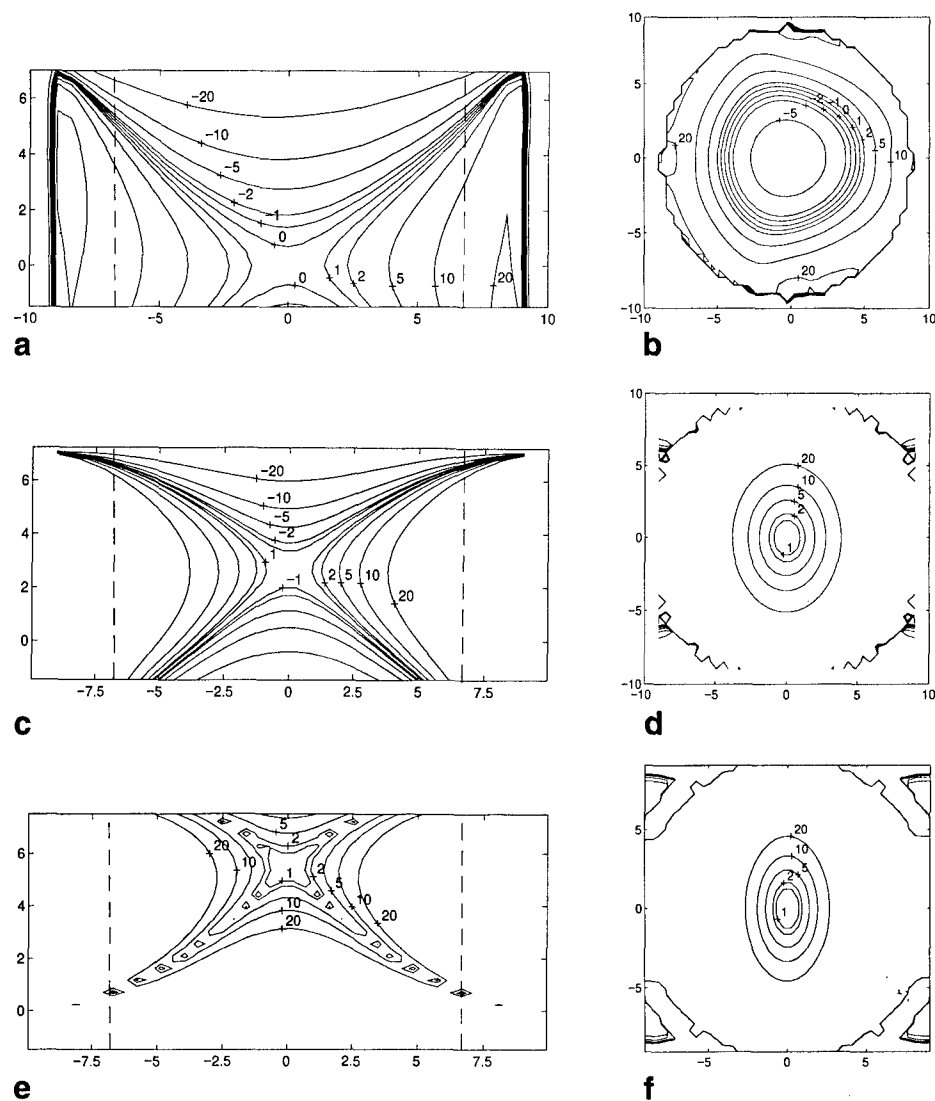


FIG. 6. Contour plots showing percentage deviations from gradient uniformity for the G_z coil over (a) an axial plane (x - y) showing the entire VOI with the top edge of the plot corresponding to the top surface of the coils. The outer circumference of the VOI is at 6.75 cm, as indicated by dashed lines. (b) A coronal plane (x - z) located at the center of the defined VOI, i.e., at ~ 3 cm above the geometric coil center. In Fig. 6a, the contours are symmetric around $y = 0$ cm with some small deviations due to return-wire contributions. (c, d) The corresponding plots for the constructed G_y coil shown in Fig. 4b. (e, f) The corresponding plots for a conventional transverse coil with return wires on the cylinder, as in Fig. 3b.

coil to produce $B_z = 0$ at the upper end of the coil, and a maximum in B_z toward the bottom end, similar to the asymmetric head coil design by Roemer (11). We used the target field approach to optimize the rate at which the field falls off toward the upper end of the coil to produce a linear variation in B_z . Although the region of acceptable gradient uniformity for our truncated target field coil is not as large as for the quadrupole coils, it compares favorably to the performance of the full target field design. We show in Figs. 6e and 6f the corresponding plots from a complete 40 loop per side target field coil with the same dimensions as our modified coil (i.e., with return wire paths at the bottom of the cylinder as in Fig. 3b). The region of acceptable gradient uniformity for our truncated target field coil is much larger than for the complete target field coil. In addition, the gradient efficiency is better for our truncated coil by a factor of 1.7, due to

the larger number of windings that could be placed on the cylinder for our coil.

To verify the field simulations, gradient uniformity was tested by acquiring images of grid phantoms. Deviations from gradient uniformity are manifest in the images as geometric distortions. The phantoms consisted of acrylic cylinders filled with square plastic gridding and CuSO_4 -doped 0.9% saline solution. The grid spacing was 1.7×1.7 cm, whereas the phantoms had an outer diameter of 12.5 cm and a height of 15 cm (extending 3 cm higher than the top surface when placed inside the coils). The coil performance was tested on a clinical GE Signa imager, using our coils for all imaging gradients (with gradient strengths matched to the whole-body coils) in a standard spin-echo pulse sequence. In general, local gradient coils often require modification of the compensation network for the gradient coil amplifiers since the

coil inductances are quite different from the whole-body coils. Because the inductances of our breast coils were very similar to the whole-body coils, no modification of the network was necessary. Images of a grid phantom are shown in Fig. 7 for planes corresponding approximately to the theoretical field plots shown in Figs. 6a and 6b and are evidence of the good gradient uniformity achieved over most of the VOI. These images were acquired using a spin-echo sequence with $TE = 20$ ms, $TR = 500$ ms, matrix size = 256×256 , and 2 NEX. The image size is 16×16 cm, and the VOI vertical extent is marked with arrows.

The first RF coil we constructed was a quadrature coil consisting of a solenoidal coil to provide the vertical mode and a saddle coil to provide the horizontal coil. Unfortunately, the vertical mode was inductively coupled to both the y-gradient coil and to the RF shield and could not be tuned to the proton resonant frequency at 1.5 T. We therefore chose to construct a coil that would operate in linear mode, with only a horizontal B_1 component present. We constructed a birdcage coil that creates a horizontal mode B_1 field with a high degree of homogeneity over a large volume. The unloaded Q of this coil (when located inside the gradient coil structure) was 80, whereas the Q for loading with a 0.9% saline phantom was 29.

Although the gradient strengths required for conventional imaging (10 mT/m) can be generated at less than 6 A using these coils, higher currents are required for more demanding applications such as flow imaging and diffusion imaging. To test the effectiveness of the water cooling system, a DC current was applied to the coil with the highest total resistance, G_y , and the temperature rise was measured for different water flow rates by monitoring a thermocouple located on the surface of the wires. The temperature was monitored until equilibrium was

achieved. Measured temperature rises are shown in Fig. 8 for DC currents between 0 and 22 A and a cooling water flow rate of 8 liter/min. Similar results were obtained for other flow rates, at which the equilibrium temperature increased with decreasing flow rates but did not change significantly from the results shown in Fig. 8 for higher flow rates. This behavior has also been demonstrated in purely cylindrical gradient coils and was modeled by Chu and Rutt (12) using an analysis based on fundamental heat transfer theory.

Diffusion Imaging

ADC maps for a $T_2 = 60$ ms $NiSO_4$ -doped agar phantom are shown in Fig. 9; Fig. 9a shows the results obtained using the GE gradient coils, and Fig. 9b shows the results obtained using our gradient coils with diffusion gradient strengths four times higher than that of the GE coils. The mean ADC for all three experiments was the same within experimental error: $(1.8 \pm 0.3) \times 10^{-3}$ mm²/s for the GE coils ($\pm 30\%$ peak-to-peak), $(1.8 \pm 0.3) \times 10^{-3}$ mm²/s for our gradient coils with diffusion gradient strengths matched to the GE coils, $(1.9 \pm 0.2) \times 10^{-3}$ mm²/s for our gradient coils with diffusion gradient strengths four times higher than that of the GE coils and $TE = 46$ ms. As expected, the observed signal-to-noise ratio was increased by nearly a factor of 2 for the $TE = 46$ ms images compared to the corresponding b -factor images at $TE = 80$ ms.

DISCUSSION

The performance and homogeneity of the gradient coils were in excellent agreement with theoretical predictions. The volume of acceptable gradient uniformity ($<20\%$ deviation) extended over most of our defined VOI for all

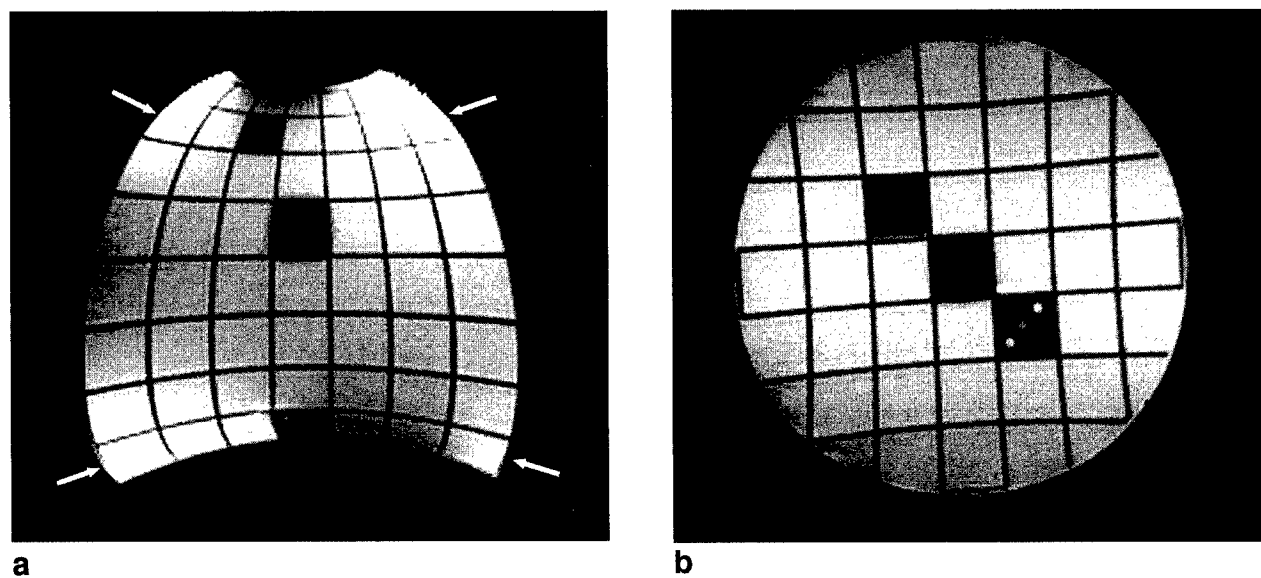


FIG. 7. Spin-echo images of a grid phantom acquired (a) for an axial plane (x - y) and (b) for a coronal plane (x - z) with the specialized breast quadrupole gradient coils. The input current strength required for the least efficient (G_y) coil was approximately 14 times less than that required for the corresponding GE coil.

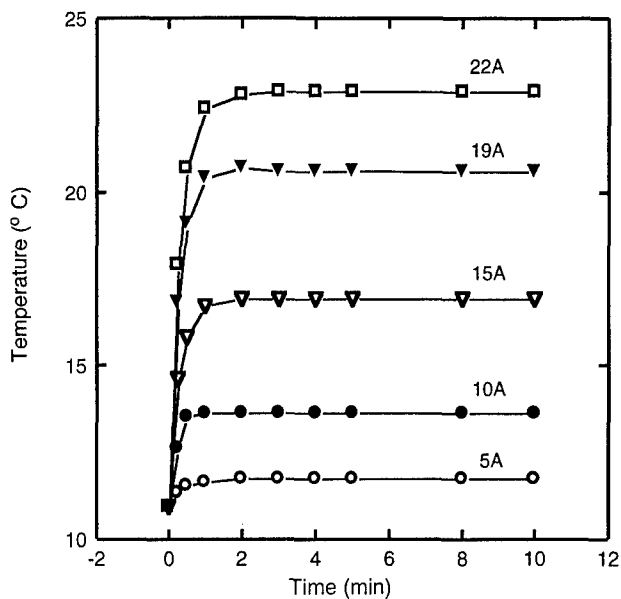


FIG. 8. Temperature response of assembled gradient coils to a DC current applied to the coil with the highest resistance (G_y) monitored at the surface of the G_y coil where the winding density was greatest.

three gradient coils. For this region, the theoretical plots of B_z can be used to generate a gradient-warping algorithm for the coils (13) to correct spatial distortions in the images. Additionally, the known deviations from gradient uniformity can be used to correct calculations of diffusion-weighting b factors (which will vary spatially across the VOI for our coils). Unfortunately, greater deviations from uniformity could not be avoided for the top 1 cm of the VOI near the upper edges of the coils for our coil designs. Deviations from uniformity of more than 20% lead to large image distortions and likely cannot be satisfactorily corrected using conventional schemes. Many breast lesions occur close to the chest wall; to be clinically useful, it is important to image accurately as close to the chest wall as possible. Several new gradient coils with improved gradient uniformity at the top edge of the coil have been reported recently (14, 15). Future improvements on our coil design will focus on extending the region of usable gradient beyond the top edge of the coil (16) as far as possible. For our preliminary clinical work with these coils, we will limit our study to patients with known lesions occurring in a region of the breast that falls within the 20% uniformity region of our gradient coils. This approach will allow us to implement pulse sequences under ideal conditions, (a) to determine the best parameters for visualizing breast lesions, (b) to determine the minimum required gradient strengths and uniformities, and (c) to make an initial assessment of the clinical utility of this approach.

In future coil designs, it may be possible to extend the region of usable gradient farther into the cylinder in the $-y$ direction by recessing the coils in the patient table or by constructing a dedicated breast imaging table, thereby allowing higher aspect ratio coils. In this design, the coil assembly would be constructed to allow positioning on

either side of the table, depending on which breast was being imaged. A fiberglass or Kevlar sheath covering the coil assembly and running the length of the patient table would serve the dual functions of isolating the patient from the electrical and cooling circuits and providing an additional form of mechanical fixation to secure the coils on the table. Because the coils are not torque-balanced, it will be necessary to anchor the structure firmly, both from the point of view of vibration-induced imaging artifacts and of patient safety.

The high gradient efficiencies of these coils will allow much higher spatial-resolution imaging than can currently be achieved in a clinical setting, and additionally, will provide very large amplitude motion-sensitizing gradients, thus facilitating diffusion imaging (or flow imaging) in small blood vessels with short echo times. T_2 has been measured for human breast tissue, with reported values ranging between 60 and 150 ms (17, 18). Recently, we reported T_2 approximately 70 ms for human breast tumor (MCF7 human breast carcinoma) growing in a mouse mammary fat pad (19). More fibrous tumors can have significantly shorter T_2 s. For this reason, initial signal loss at $b = 0$ s/mm² due to T_2 weighting of the image can severely limit the range of b factors for which images can be obtained, which has the result of limiting the precision of the ADC measurement. Our approach is to shorten TE while maintaining diffusion weighting by increasing diffusion gradient amplitudes. This gives a substantial increase in initial signal intensity for $b = 0$ s/mm², allowing high-quality images to be obtained for much higher b factors. Even in cases in which signal loss from T_2 weighting is not so severe as to limit ADC precision, the ability to obtain high diffusion weighting with short TE reduces dramatically the T_2 contrast in an image. This will allow acquisition of a diffusion-weighted image in which the contrast is determined mainly by tissue ADC rather than by a mix of ADC and T_2 .

A secondary important benefit that can be gained using high-efficiency gradient coils is that the ramp time required to attain imaging gradient strengths (10–25 mT/m) is decreased from that required by whole-body coils by a factor of the efficiency (since the current slew rate is similar to whole-body coils, and the required peak current is decreased). This will enable echo-planar imaging (and other fast imaging techniques) using conventional gradient amplifiers. Echo-planar imaging techniques have been proven to be much less susceptible to motion artifacts than conventional imaging sequences (20) and have recently been applied to diffusion imaging *in vivo* (21) with good results.

For rapid imaging pulse sequences, and for high-amplitude bipolar pulses, very rapid changes in gradient polarity are required. Although the magnetic field amplitudes drop off quickly in the region above the coils, magnetic fields are also generated by the return wires on the horizontal plate, and excitation thresholds for cardiac stimulation must be considered. As an upper limit for one coil, $|B|$ was calculated for the G_z coil at various distances above the return wires at the location of the highest wire density. The maximum dI/dt from our gradient coil amplifiers is 200 A in 184 μ s. This produces $dB/dt = 156$ T/s at 1 cm above the coil return wire plate

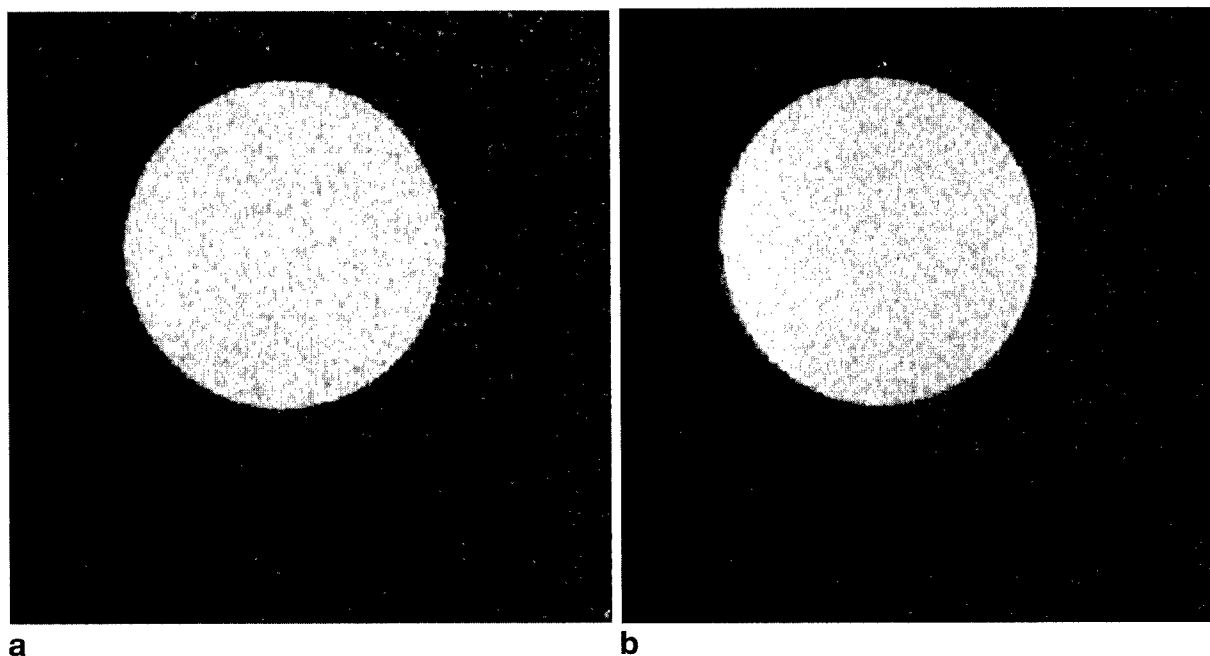


FIG. 9. ADC maps of a $T_2 = 60$ ms agar phantom obtained (a) using the whole-body coils to provide all diffusion and imaging gradients, $TE = 80$ ms, and (b) using the breast gradient coils to provide all gradients, where the diffusion gradient strengths were four times the whole-body gradient strengths and $TE = 46$ ms. In all cases, the ADC maps were constructed from 10 images with $b = 0$ to $b = 1000$ s/mm^2 .

and $dB/dt = 50$ T/s at 10 cm, compared to a recommended upper limit of 400 T/s for cardiac stimulation (22). The magnitude of these fields is relatively small at regions of concern with respect to magnetic stimulation such as the heart; however, peripheral nerve stimulation has been reported at dB/dt as low as 40 T/s in some patients (22). Theoretical field calculations will allow prediction of $|B|$ and dB/dt for all pulse sequences before implementation, and pulse sequences will be tailored to adhere to maximum dB/dt and peak $|B|$ guidelines. Additionally, if peripheral nerve stimulation is reported for individual patients, dB/dt will be reduced below the stimulation threshold by increasing gradient switching times.

SUMMARY

We have constructed a three-axis gradient coil set for imaging human breast tumors. These coils create gradient efficiencies of up to 3.3 mT/m/A with relatively low inductance (≤ 1000 μH), and good gradient uniformity over most of the volume required for breast imaging. Preliminary diffusion results were obtained in a water phantom for b factors as high as ~ 1000 s/mm^2 for $TE = 46$ ms. A compact, efficient water-cooling system was presented, which maintained coil temperatures at or below room temperature, even for RMS currents as high as 20 A. This gradient/cooling module will allow, for the first time, clinical breast imaging using diffusion and microvascular flow-weighted protocols with high spatial resolution.

REFERENCES

1. D. S. Webster, K. H. Marsden, Improved apparatus for the NMR measurement of self-diffusion coefficients using pulsed field gradients. *Rev. Sci. Instrum.* **45**, 1232-1234 (1974).
2. K. C. Chu, B. K. Rutt, Quadrupole gradient coil design and optimization: a printed circuit board approach. *Magn. Reson. Med.* **31**, 652-659 (1994).
3. W. G. O'Dell, J. S. Schoeniger, S. J. Blackband, E. R. McVeigh, A modified quadrupole gradient set for use in high resolution MRI tagging. *Magn. Reson. Med.* **32**, 246-250 (1994).
4. R. Turner, A target field approach to optimal coil design. *J. Phys. D. Appl. Phys.* **19**, L147-151 (1986).
5. R. Turner, Gradient coil design: a review of methods. *Magn. Reson. Med.* **11**, 903-920 (1993).
6. P. W. McOwan, T. W. Redpath, A specialised receiver coil for NMR imaging of female breasts. *Phys. Med. Biol.* **32**, 259-263 (1987).
7. J. P. Hornak, J. Szumowski, R. G. Bryant, Elementary single turn solenoids used as the transmitter and receiver in MRI. *Magn. Reson. Imaging* **5**, 233-237 (1987).
8. L. Sun, L. O. Olsen, P. L. Robitaille, Design and optimization of a breast coil for magnetic resonance imaging. *Magn. Reson. Imaging* **11**, 73-80 (1993).
9. E. O. Stejskal, J. E. Tanner, Spin diffusion measurements: spin echoes in the presence of a time-dependent field gradient. *J. Chem. Phys.* **42**, 288-292 (1965).
10. M. Neeman, J. P. Freyer, L. O. Sillerud, A simple method for obtaining cross-term-free images for diffusion anisotropy studies in NMR microimaging. *Magn. Reson. Med.* **21**, 138-143 (1991).
11. P. B. Roemer, Transverse gradient coils for imaging the head. United States Patent No. 5177442, January 5, 1993.
12. K. C. Chu, B. K. Rutt, MR gradient coil heat dissipation. *Magn. Reson. Med.* **34**, 125-132 (1995).
13. M. O'Donnell, W. A. Edelstein, NMR imaging in the presence of magnetic field inhomogeneities and gradient field nonlinearities. *Med. Phys.* **12**, 20-26 (1985).
14. A. Ersahin, H. K. Lee, O. Nalcioglu, Asymmetric gradient coil design for high resolution breast imaging, in "Proc., SMR and ESMRMB, 3rd

- Annual Meeting, Nice, 1995," p. 954.
15. H. K. Lee, R. Raman, R. Slates, A. Ersahin, O. Nalcioglu, An optimized gradient coil for breast imaging, in "Proc., SMR and ESMRMB, 3rd Annual Meeting, Nice, 1995," p. 955.
 16. B. A. Chronik, B. K. Rutt, Constrained length minimum inductance gradient coil design, in "Proc., ISMRM, 5th Annual Meeting, Vancouver, B.C., Canada, 1997," p. 53.
 17. D. Z. J. Chu, W. S. Yamanashi, J. Frazer, C. F. Hazlewood, H. S. Gallager, A. W. Boddie, R. G. Martin, Proton NMR of human breast tumors: correlation with clinical prognostic parameters. *J. Surg. Oncol.* **36**, 1-4 (1987).
 18. S. J. Graham, M. J. Bronskill, J. W. Byng, M. J. Yaffe, N. F. Boyd, Quantitative correlation of breast tissue parameters using MR and X-ray mammography. *Br. J. Cancer* **73**, 162-168 (1996).
 19. C. F. Maier, Y. Paran, P. Bendel, B. K. Rutt, H. Degani, Quantitative diffusion imaging in implanted human breast tumors. *Magn. Reson. Med.* **37**, 576-581 (1997).
 20. R. Turner, D. LeBihan, Single-shot diffusion imaging at 2.0 Tesla. *J. Magn. Reson.* **86**, 445-452 (1990).
 21. R. Turner, D. LeBihan, A. S. Chesnick, Echo-planar imaging of diffusion and perfusion. *Magn. Reson. Med.* **19**, 247-253 (1991).
 22. J. P. Reilly, Principles of nerve and heart excitation by time-varying magnetic fields, in "Biological effects and safety aspects of NMRI and spectroscopy." *Ann. N. Y. Acad. Sci.* **649**, 96-107 (1993).

Design and Fabrication of a Three-Axis Edge ROU Head and Neck Gradient Coil

Blaine A. Chronik,^{1,3} Andrew Alejski,³ and Brian K. Rutt^{1,2,3*}

The design, fabrication, and testing of a complete three-axis gradient coil capable of imaging the human neck is described. The analytic method of constrained current minimum inductance (CCMI) was used to position the uniform region of the gradient coil adjacent to and extending beyond the physical edge of the coil. The average gradient efficiency of the three balanced axes is 0.37 mT/m/A and the average inductance is 827 μ H. With maximum amplifier current of 200A and receive signal sweep width of ± 125 kHz, the average minimum FOV using this gradient set is 7.9 cm. The completed coil has an inner diameter of 32 cm, an outer diameter of 42 cm, and a length (including cabling connections) of 80 cm. The entire coil was built in-house. The structure is actively water cooled. Heating measurements were made to characterize the thermal response of the coil under various operating conditions and it was determined that a continuous current of 100A could be passed through all three axes simultaneously without increasing the internal coil temperature by more than 23°C. Eddy current measurements were made for all axes. With digital compensation, the gradient eddy current components could be adequately compensated. A large B_z eddy current field is produced by the Gz axis that could be corrected through the use of an auxiliary B_z compensation coil. Preliminary imaging results are shown in both phantoms and human subjects. *Magn Reson Med* 44: 955–963, 2000. © 2000 Wiley-Liss, Inc.

Key words: gradient coil; neck; head; minimum inductance; carotid artery; constraints; optimization; eddy current; heating; construction; MRI; edge coil; ROU; region of uniformity; coil design

There are many important imaging applications that stand to benefit from the application of higher gradient strengths and increased switching speeds produced over the human neck and head. In the neck, velocity imaging techniques are applied to examine blood flow through the carotid artery in the vicinity of the carotid bifurcation (1). It has also been demonstrated that diffusion weighted, high resolution imaging of the carotid artery atherosclerotic plaque structure is of importance in identifying plaques at risk of rupture (2). It can be shown that to achieve a b -value of 1000 sec/mm² using a square bipolar pair of gradient lobes with no inter-lobe delay in a total time of 20 msec (10 msec per lobe), a gradient strength of 145 mT/m is required (3).

This exceeds the capabilities of present-day body gradient coils by a factor of more than 3.

A brain-specific application in which gradient switching speed is important is functional MRI (fMRI). An important goal is to obtain high spatial resolution in single-shot EPI images over a brain-sized FOV (20 cm) with an echo time yielding optimal T_2^* contrast-to-noise ratio (4). For an EPI sequence without ramp sampling, a received signal sampling rate of 500 kHz and a 20-cm FOV requires a 58-mT/m gradient strength. If a 128-lobe EPI readout train is to be played out in 64 msec, trapezoidal ramp times of 150 μ s or less are required.

A gradient efficiency of 0.4 mT/m/A with an inductance of less than 1000 μ H was chosen as the design goal for this work, as a compromise between serving applications in need of gradient speed such as fMRI (which would argue for minimizing inductance at the expense of gradient strength), and those that demand strength such as diffusion or flow imaging (which would argue for higher gradient efficiency at the cost of increased inductance). An additional stipulation was that this strength needed to be achieved over a region of uniformity (ROU) that covered the human neck. The anatomical region of interest is centered on the carotid bifurcation, and must be large enough to image the most common sites of carotid atherosclerosis. This region spans a cylindrical volume approximately 16 cm long (inferior to superior) and 16 cm in diameter, and extends into the torso, inferior to the level of the shoulders (Fig. 1). This "edge" gradient coil can be operated in a configuration compatible with brain imaging by inserting the subject only half as far into the coil. This would provide improved visual communication with the subject during scanning, a capability of considerable importance in many fMRI studies. While commercial head-only gradient insert systems are available that meet the speed and strength specifications, they are designed for brain imaging only and are incompatible with imaging the carotid artery.

A minimum inner coil diameter of 32 cm was chosen. This is considered to be compatible with human imaging, taking into account the space required for an RF coil assembly. The total coil length was specified to be less than 80 cm, based on the need to keep the coil (which would be positioned asymmetrically within the magnet bore during operation) within a uniform region of the main magnet, thereby preventing net forces on the structure.

A recently developed gradient design algorithm was applied to obtain a three-axis gradient coil meeting the specifications described above. A prototype coil was constructed, and the thermal response was tested to determine whether heating represents a significant limitation to operation. The coil was not shielded and the eddy currents were measured in order to determine the required com-

¹Department of Physics and Astronomy, University of Western Ontario, London, Ontario, Canada.

²Department of Diagnostic Radiology and Nuclear Medicine, University of Western Ontario, London, Ontario, Canada.

³Imaging Research Laboratories, The John P. Robarts Research Institute, London, Ontario, Canada.

Grant sponsor: Canadian Institutes of Health Research; Grant number: GR-14973.

*Correspondence to: Dr. Brian K. Rutt, Ph.D., Imaging Research Laboratories, The John P. Robarts Research Institute, P.O. Box 5015, 100 Perth Drive, London, Ontario N6A 5K8, Canada. E-mail: brutt@irus.ri.on.ca

Received 1 May 2000; revised 2 August 2000; accepted 3 August 2000.

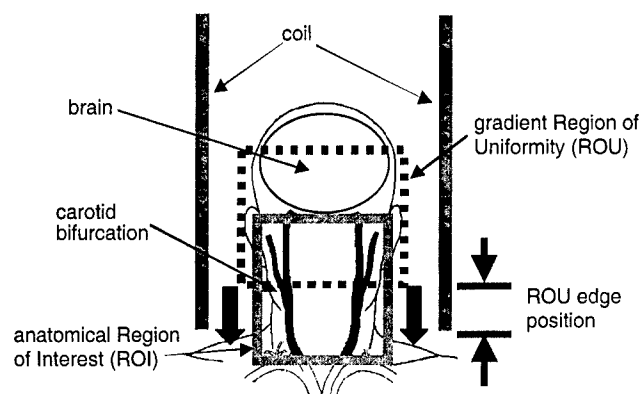


FIG. 1. Summary of the design problem. The ROU (dashed box) must be positioned to overlap the anatomic ROI (solid box) covering the carotid bifurcation. For a head-sized gradient coil, the ROU must be placed such that it extends beyond the edge of the coil.

compensation. The coil was operated in magnets of three different field strengths (0.5T, 1.5T, and 4.0T). Finally, preliminary imaging tests in both phantoms and human subjects were conducted to demonstrate the achieved gradient uniformity and image quality.

METHODS

Axis Design

All coil designs were obtained using the method of constrained current minimum inductance (CCMI) (5). The CCMI method extends analytic minimum inductance target field techniques to solve for the minimum inductance coil design subject to constraints on both the magnetic field and current density (6).

The quantities of interest in edge gradient coil design are depicted schematically in Fig. 2: They are the length of the coil, the size of the ROU, and the proximity of the ROU to the edge of the coil. Each quantity is normalized to the coil radius, a , to obtain scale independent measures. The aspect ratio (AR) is defined as the ratio of the length of the coil to the coil diameter. The relative ROU ($RROU$) is the length of the ROU divided by the coil radius. ROU length was chosen as a simple way to quantify the size of the ROU because the ROU diameter is generally larger than, and scales with, this length. The distance from the outer edge of the ROU to the outer edge of the coil, divided by the radius, is defined as δ . Negative values of δ indicate an ROU extending outside the coil. Gradient uniformity is defined in terms of the percent deviation in the magnitude of the derivative of B_z with respect to the relevant spatial direction defining that gradient axis. Unless stated otherwise, 30% deviation contours are used for quantification. The scale independent quantities (AR , $RROU$, δ) define a 3D parameter space over which coil performance is evaluated.

A figure-of-merit was used to quantify gradient performance (5,7):

$$M = \frac{\eta \cdot a^{2.5}}{\sqrt{L}} \quad [1]$$

where η is the gradient efficiency (in mT/m/A) within the edge ROU, L is the coil inductance, and a is the coil radius. M is independent of both coil radius and the number of wires used to discretize the current density.

Of practical importance is how to parameterize the constraint space input to the CCMI algorithm. The positioning of the constraints for both transverse and longitudinal axes is shown in Fig. 3a. The aspect ratio is specified by the position of the current constraints. The field constraints are placed at a radius c and positioned with spacing d along the z direction. The combination of these two constraint parameters effectively controls the size of the resulting $RROU$. The distance from the outermost field constraint to the innermost current constraint is defined as e , which controls the resulting δ . Field constraints are only required on the plane defined by $\phi = 0$ because in the implementation of the CCMI algorithm, the azimuthal variation of the current density is assumed to be either sinusoidal (transverse axes) or constant (longitudinal axes) (5).

The values of the field constraints for transverse and longitudinal axes are shown in Fig. 3b and c, respectively. For transverse axes, the relative values of the field constraints are constant along the z direction, thereby specifying a uniform transverse ROU. For longitudinal axes, the field constraint values vary linearly along the z direction; furthermore, the value of the smallest (i.e., outermost) field constraint is introduced as a separate parameter to control the relative offset of the field constraint values from zero. This constraint parameter is indicated as B_{offset} in Fig. 3c. This parameter is used because the field is not required to pass through zero at the center of the ROU as is normally the case for all central ROU designs and transverse edge ROU designs. The natural field fall-off from the coil provides the G_z gradient, and the field constraints are placed to increase its linearity. This effect is illustrated in Fig. 4.

Fabrication

The wire used for the coil was composed of 12 strands of 1.02-mm-diameter copper wire arranged in a Litz braiding to produce a wire with a rectangular cross section of $2.5 \times 7 \text{ mm}^2$ (New England Electric Wire Corporation). Individ-

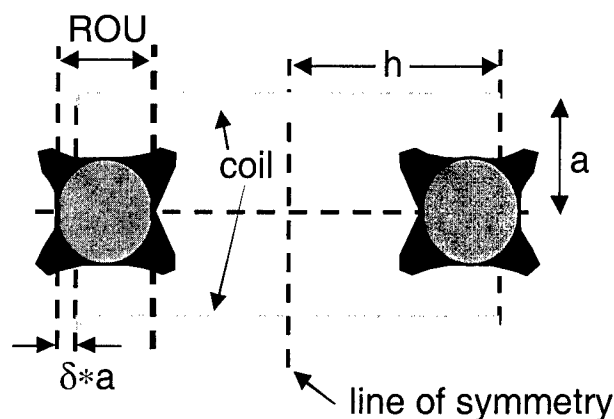


FIG. 2. Quantities of importance in edge ROU coil design are coil radius (a), length ($2h$), imaging region size (ROU), and imaging region position with respect to the edge of the coil ($\delta \cdot a$).

ual conducting elements were coated with insulation heat rated to 150°C. Litz wire was used in place of solid copper to reduce resistance at frequencies of several kilohertz, expected to be the dominant operating frequency of the coil for high-speed imaging sequences. The DC resistance of the wire was 2 mΩ/m. The multistrand formation of the Litz wire also improved its workability; by comparison, winding the transverse axis patterns with an equal area of solid copper wire was found to be very difficult.

The winding pattern was produced using a numerically controlled mill over the outside of the cylinders and the wire was hand-wound into the milled grooves. A light coating of epoxy was applied to hold the wire in place and to fix a type-E thermocouple at the location of maximum wire density. These thermocouples allow active temperature monitoring of the hottest areas of the coil. The pattern for each layer was wound with one continuous length of wire to avoid solder connections within the wall of the coil, the most probable site for thermal failure.

Copper tubing (7 mm diameter) capable of carrying forced-water cooling at flow rates of up to 11 l/min was plotted between the X and Y axes and the Y and Z axes of

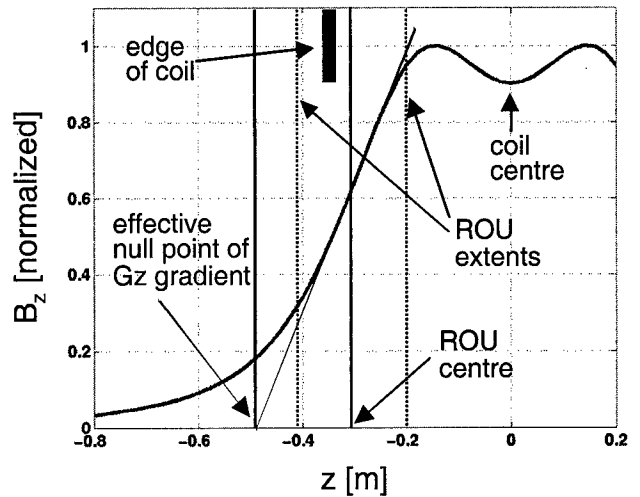


FIG. 4. Example representation of the B_z field profile (solid curve) along the z-axis of an edge longitudinal gradient coil, indicating the offset of ROU position from the coil center. The edge of the coil is indicated by the heavy bar. The gradient efficiency is determined by the field profile at the z coordinate of the ROU center. The center of the coil is at $z = 0$. Note that the effective null point of the gradient field is at neither the center of the ROU nor the center of the coil.

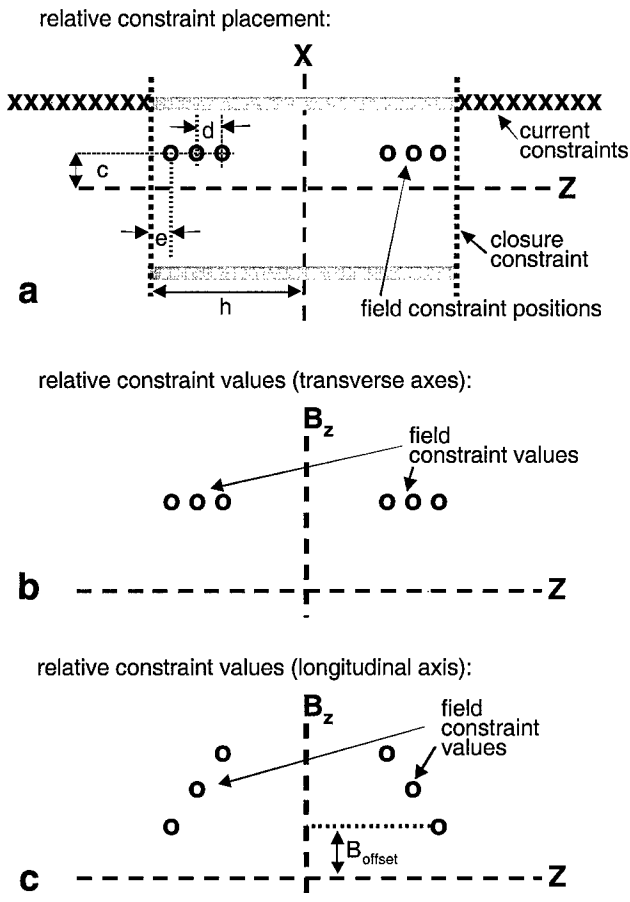


FIG. 3. Parameterization of input constraint space for CCMI algorithm. Constraint positions for both transverse and longitudinal axes are shown in **a**. Field constraint values for transverse and longitudinal axes are shown in **b** and **c**, respectively. Current constraint values are always set equal to zero. B_{offset} is the value of the smallest (i.e., outermost) field constraint.

the coil. The epoxy potting compound (Durapot 865, Cotronics Corporation, New York) was specially chosen to have a high thermal conductivity (2.8 W/m/K) allowing efficient heat transfer from the winding layers to the two cooling layers.

Before using the coil in an MR scanner, a fixation mechanism was built to prevent motion of the coil within the magnet bore during normal operation and in the event of any failure modes the coil might experience. An external frame was constructed to encase the coil, which was subsequently attached to the external housing of the main magnet. The frame held the coil from front to back as well as encasing it top to bottom and side to side. The frame was composed of 2.54-cm phenolic plates (front and back) and 5-cm × 10-cm beams (longitudinal). The bottom beams of the frame extended out the back of the magnet bore along the table tray and were attached to support beams mounted to the rear of the scanner. In Fig. 5, the completed gradient coil is shown being installed into the 1.5T scanner.

Heating Measurements

Coil heating was tested in a series of experiments in which 100A_{rms} was passed through all axes simultaneously, while water-flow rates of 0, 6, and 11 l/min were applied. These conditions were chosen as representing an extreme case of gradient coil operation. Heating was halted when internal coil temperatures increased by 50°C.

The model used to describe the temperature increase (ΔT) as a function of time is (8,9):

$$\Delta T(t) = \Delta T_{ss} \cdot (1 - e^{-t/\tau}) \quad [2]$$

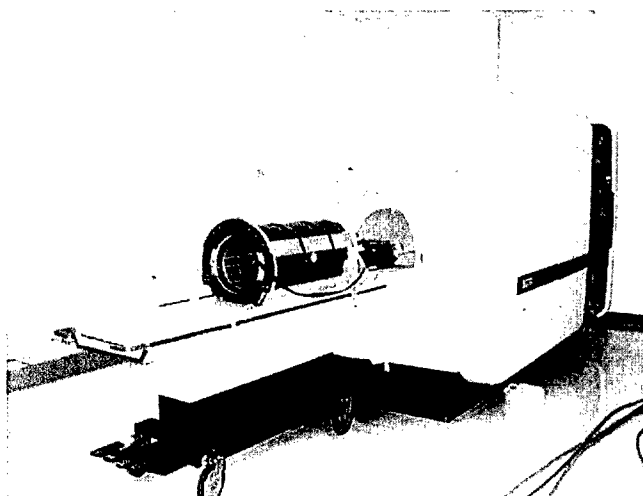


FIG. 5. The completed neck gradient coil being installed into the 1.5T GE Signa scanner. The coil was inserted from the front of the magnet and secured at the back. The coil was transported into and out of the magnet room using the standard scanner patient bed.

where ΔT_{ss} is the steady state temperature rise and τ is a time constant describing the rate at which steady state is achieved. Equation [2] was fit to the experimental data to obtain values for ΔT_{ss} and τ for each level of water cooling.

Electrical Measurements and Gradient Efficiency

Bench top measurements of both resistance and inductance were made at frequencies of 120 Hz, 1 kHz, and 10 kHz using a Hewlett-Packard 4262A LCR meter.

The completed coil was interfaced with both a Varian-Siemens Unity INOVA 4T whole body scanner (peak current: 250A, peak voltage: 600V), a 1.5T General Electric Signa Horizon with Echosped gradient amplifiers (peak current: 200A, peak voltage: 1200V; General Electric Medical Systems, Milwaukee, WI), and a 0.5T General Electric Signa Scanner (peak current: 84A, peak voltage: 200V). Various RF coils were constructed and tuned to resonate within the bore of the gradient coil.

The gradient efficiency for each axis was measured by imaging a grid phantom of known dimensions using a known current and an initial guess at the efficiency (i.e., the calculated values). The reconstructed image grid was used in conjunction with the known grid dimensions to adjust the gradient efficiency until the elements of the image were reconstructed to the correct dimension. The phantom was composed of a cylindrical container filled with water (19 cm diameter, 25 cm length), containing a plastic rectangular lattice with square in-plane grid elements $16 \times 16 \text{ mm}^2$. The phantom was larger than the expected ROU to allow determination of gradient inhomogeneities beyond the ROU.

Eddy Current Measurements and Compensation

Eddy currents were measured on the 4T scanner. For each axis, an RF solenoid containing a small, pure water sample was placed in two different positions, and the FIDs following an RF excitation after a gradient pulse were measured.

The derivative of the phase with respect to time of each FID gave an estimate of the instantaneous frequency, and therefore the local field, experienced by that coil as a function of time following the gradient pulse. By comparing the frequencies measured by the two solenoids and knowing the separation of the samples, the gradient and B_0 components of the eddy current fields were determined.

The transient fields were fitted to a multiexponential decay curve using the method of least-squares minimization. The amplitude of the gradient eddy current fields were expressed as a percentage of the applied gradient pulse. B_0 eddy current fields were expressed as a frequency shift normalized to the amplitude of the applied gradient pulse (i.e., in units of Hz/mT/m).

The 4T scanner is equipped with digital eddy current compensation allowing five different amplitude and time constant components to be added to gradient waveforms in order to compensate for the gradient field components. This scanner currently lacks a B_0 compensation coil and there was no ability to directly compensate for B_0 field transients. The values of the fit to the transient gradient field response were entered into the digital compensation control and the eddy currents measured again. This process was repeated iteratively until an acceptable degree of compensation was achieved.

Imaging

All human imaging was conducted on the 1.5T scanner, without any eddy current compensation. Because the inductances of the neck coil axes were significantly smaller than those of the body coil for this scanner (on average, $780 \mu\text{H}$ as compared to $1200 \mu\text{H}$), an inductor was added in series with each axis of the neck coil to prevent oscillations in the amplifier output current and minimize pre-emphasis errors.

On the 4T scanner, gradient eddy current compensation was applied as described above. No extra inductance was required because the system was capable of accommodating inductances in the range of $300 \mu\text{H}$ to $1400 \mu\text{H}$. A more robust fixation mechanism was implemented because of the increased forces on the coil. In its first implementation this fixation was not compatible with human imaging, and therefore all preliminary images collected were of small animals and phantoms.

RESULTS

Transverse Axis Design

Figure 6 shows a plot of M as a function of AR for a fixed $RROU$ size of 1.0 and three different values of δ (-0.2 , 0.0 , and 0.2). For each value of δ , increasing AR s result in higher values of M . The merit improvements plateau above certain AR s, the values of which are a function of δ .

The effects of moving the ROU with respect to the edge of the coil are more effectively visualized by examining the M contour plot of Fig. 7. The contour plot is over the axes of $RROU$ and δ , for a fixed AR of 2.3. The effect of increasing $RROU$ is generally to decrease M . For any fixed $RROU$, the dependency of M on δ displays a maximum at a value of δ , which is itself a weak function of the $RROU$.

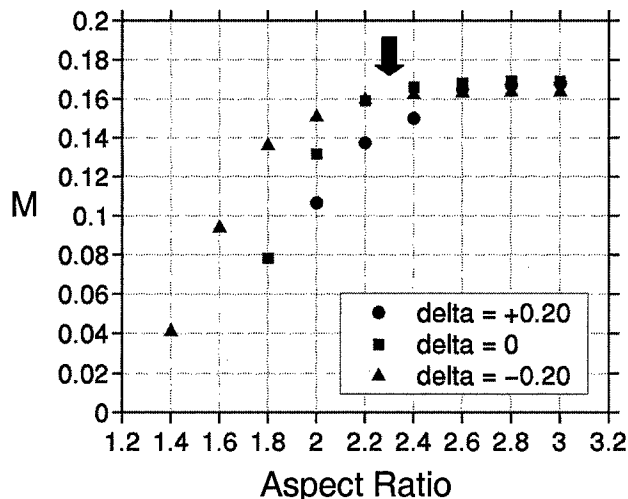


FIG. 6. Design merit (M) vs. aspect ratio (AR) for transverse coil designs of three δ values ($-0.20, 0, 0.20$). $RROU$ was held constant at 1.0. The solid arrow indicates the AR taken as constant for the plot of Fig. 7.

With this design space determined, the optimal configuration for this application could be identified. Based on Fig. 6, the aspect ratio of 2.3 (indicated on the plot by the solid arrow) was chosen as the smallest value for which no decrease in M was associated. For an axis radius of 16.5 cm, this corresponds to a coil length of 76 cm.

With the value of AR chosen, Fig. 7 was consulted to fix the properties of the ROU. For a 16.5-cm radius coil the ROU specifications mentioned in the introduction corre-

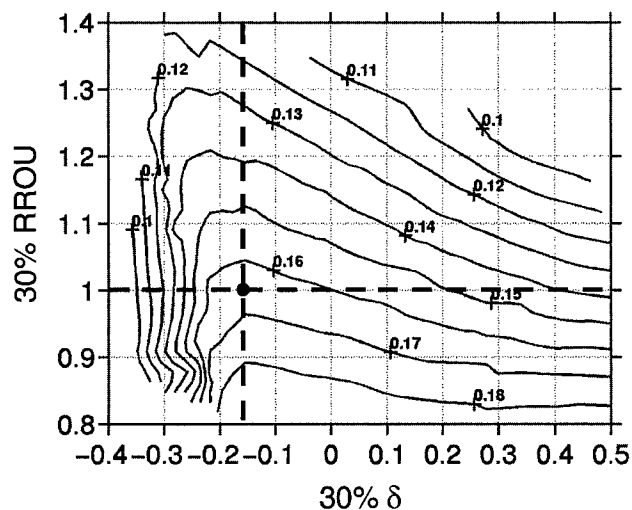


FIG. 7. A contour plot of M over the plane of constant $AR = 2.3$ through the transverse design parameter space. The horizontal axis indicates the position of the outer edge of the imaging region with respect to the edge of the coil as a fraction of the coil radius. The vertical axis indicates the length of the imaging region as a fraction of the coil radius. For a coil radius of 16.5 cm, the plot area above the horizontal dashed line is compatible with neck imaging. The highest performance design in the space above the ROU limit is indicated by the dot at the intersection of the vertical and horizontal dashed lines.

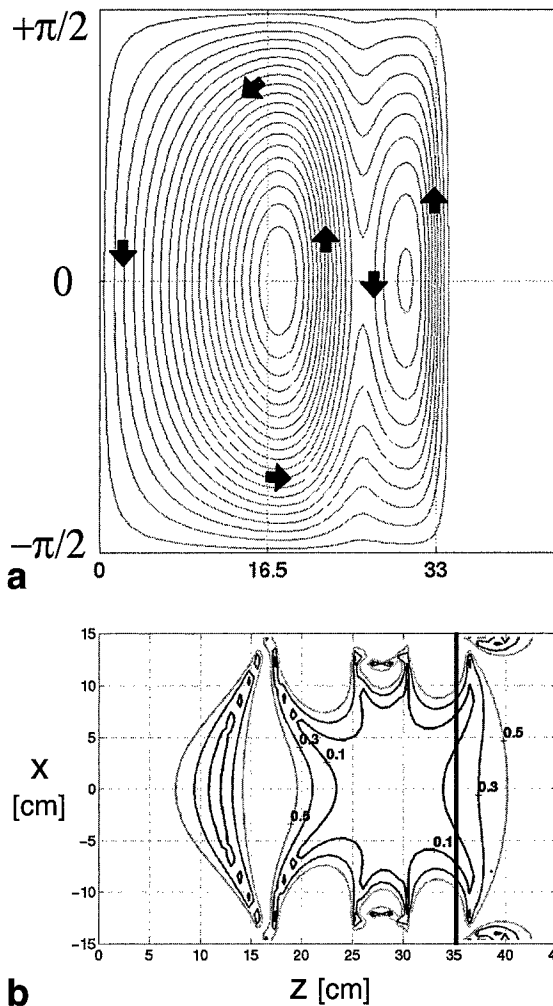


FIG. 8. Chosen transverse axis (G_x) design. **a**: Single quadrant wire pattern. Solid arrows indicate the relative current directions through the wire pattern. **b**: Calculated map of gradient uniformity over the transverse plane. The z -axes for both plots are to the same scale, and therefore the position of the ROU with respect to the wire pattern can be seen by comparing **a** and **b**. The solid bar in **b** indicates the edge of the physical coil. The G_y axis uses this same design.

spond to an $RROU$ of approximately 1.0; therefore, the allowed designs occupy the region above the horizontal dashed line defining $RROU = 1.0$. The highest performance design in the remaining region of the plot corresponds to a δ of -0.16 (indicated by the vertical line of Fig. 7). This value corresponds to an ROU projecting 2.6 cm beyond the inferior end of the coil. This meets the neck imaging criterion, and therefore the coil corresponding to the design space parameter coordinate $(AR, RROU, \delta) = (2.3, 1.0, -0.16)$ was chosen as the best transverse coil design for this application.

A single quadrant of the wire pattern corresponding to this design is shown in Fig. 8a. The calculated ROU extents for 10%, 30%, and 50% deviations from uniformity are shown in Fig. 8b. The calculated performance parameters for this design (for both the x and y axes) are summarized in Table 1.

Table 1
Calculated and Measured Coil Characteristics

		X	Y	Z
Radius [m]		0.1625	0.1825	0.2025
η [mT/m/A]	Calculated	0.42	0.35	0.37
	Measured	0.40	0.35	0.35
L [μ H]	Calculated [DC]	760	800	805
	120 Hz	780	820	880
	1 kHz	780	820	870
	10 kHz	770	810	860
R [m Ω]	Calculated [DC]	220	235	153
	120 Hz	227	230	160
	1 kHz	270	290	210
	10 kHz	-	-	-

Longitudinal Axis Design

Because imaging regions for all axes of a three-axis coil system must overlap for them to be useful as a group, decisions made regarding one axis have ramifications on the design of the others. Longitudinal designs display better performance than transverse designs; therefore, most effort was expended choosing the optimal transverse axis design. The longitudinal design was then simply required to be compatible with the AR and ROU placement.

The chosen design for the longitudinal axis is shown in Fig. 9. One quadrant of the wire pattern is shown in Fig. 9a. The calculated ROUs for 10%, 30%, and 50% deviations from uniformity are shown in Fig. 9b. The 30% ROU is approximately 17.5 cm long and its outer extent is 5 cm exterior to the coil. Although both of these quantities exceeded the minimal specifications of matching the transverse design ROU position and size, it was determined that over the longitudinal design space this configuration represented the highest merit. The relevant performance parameters for this design are summarized in Table 1.

Heating Measurements

The measured values for ΔT_{ss} and τ are shown in Table 2. Even without cooling, the coil could be run for over 15 min before temperatures increased by 50°C. With cooling, the coil could be operated indefinitely at 100A_{rms} with a temperature rise of less than 23°C.

Electrical Measurements

The measured values for resistance and inductance for the three axes are summarized in Table 1. The calculated values are included for comparison. The relatively slow increase of resistance with frequency is expected because of the Litz wire construction. The calculated resistance values are generally lower than the experimental results because they assume zero frequency and do not take into account lengths of connecting wire within the coil or the effects of imperfect electrical connections.

Eddy Current Measurements and Compensation

Table 3 summarizes the results of eddy current measurements for each gradient axis, before and after compensation. Cross-axis eddy current effects were also measured for all combinations of axes, and in every case were found,

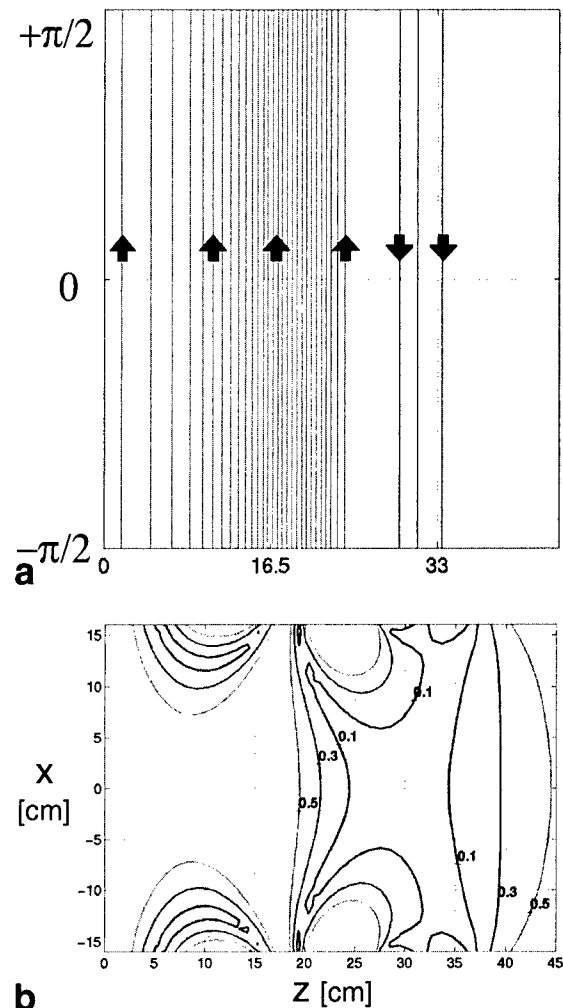


FIG. 9. Chosen longitudinal axis (G_z) design. **a**: Single quadrant wire pattern. **b**: Calculated map of gradient uniformity over the transverse plane. The z -axes for both plots are to the same scale, and therefore the position of the ROU with respect to the wire pattern can be seen by comparing **a** and **b**. The solid bar in **b** indicates the edge of the physical coil (determined by the extent of the transverse axes).

without compensation, to be smaller than 0.03% of the applied gradient. Because of the small amplitude, no cross-axis compensation was applied.

The eddy current results for the G_x and G_y axes are similar. Prior to compensation, both transverse axes were characterized by small residual gradient fields (less than 0.07%) with time constants of less than 100 msec. Compensation reduced these effects to less than 0.02%. The G_y axis displayed a small, negative B_0 eddy current response, whereas the G_x axis B_0 response was almost negligible.

Table 2
Heating Measurement Summary

Flow [l/min]	ΔT_{ss} [°C]	τ [s]
0	63.1	573
6	34.3	365
11	22.7	209

Table 3
Compensated and Uncompensated Eddy Current Measurements

Axis		Before compensation	After compensation
X	G_x	0.037% 63 ms	0.01%
	B_o	-0.07 Hz/mT/m 500 ms	-
Y	G_y	0.066% 34.4 ms	0.02%
	B_o	-0.55 Hz/mT/m 116 ms	-
Z	G_z	60 ms; 0.14% 980 ms 21.3 Hz/mT/m	0.1%
	B_o	100 ms; 22.4 Hz/mT/m 517 ms	-

For the G_z axis, the gradient eddy current component was bi-exponential with a maximum residual gradient of 0.44%. With compensation this was reduced to less than 0.1%. The B_o eddy current component for the G_z axis was observed to be much larger than either of the transverse axes and was also bi-exponential. Immediately following an 80 mT/m gradient pulse on the G_z axis, the eddy current induced field offset would be approximately 3500 Hz.

The proposed mechanism for this B_o eddy current effect is shown schematically in Fig. 10. Eddy current fields produced over the image region have a different spatial dependency than the primary imaging gradient field. The gradient component of the eddy current field does not have an effective null point (i.e., extrapolated zero cross-

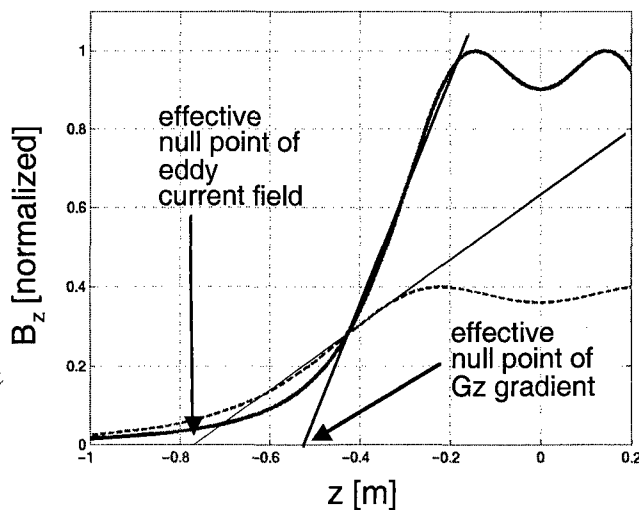


FIG. 10. Schematic comparison of G_z gradient field profile (solid curve) and corresponding eddy current-induced field profile (dashed curve). The effective null points of each profile are, in general, different. No amount of current can be passed through the gradient coil to compensate for the eddy current field shown above. If compensation is applied such that the gradient coil field compensates for the slope of the eddy current field, a large B_o offset would result.

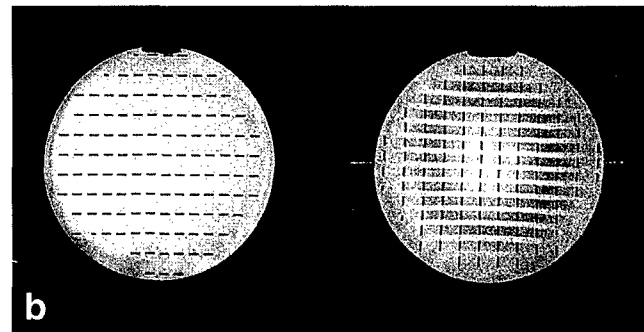
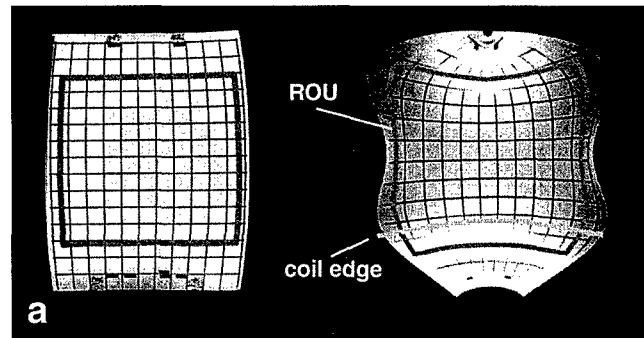


FIG. 11. Coronal (a) and axial (b) images of a cylindrical grid phantom collected using a standard body gradient coil (left) and neck gradient coil (right). Deviations from gradient uniformity result in image distortions in both cases. Individual grid elements are 16 mm square. The box indicated on the coronal images corresponds to an ROI of 16 cm square. The curved line in b indicates the relative position of the edge of the gradient coil.

ing) at the same location as the imaging gradient. There is therefore no current that can be applied to the gradient coil that will fully compensate for this transient eddy current. The best option would be to remove the linear variation while creating a significant field offset proportional to the difference in the positions of effective null points of the primary and eddy current-induced fields.

Imaging

Figure 11 compares images of the grid phantom collected with the neck gradient set to those collected using the whole body gradient set of the 1.5T scanner. Images were collected using a spin-echo sequence with the following parameters: TE/TR = 30/1000 msec, matrix size = 512 × 512, FOV = 36 × 36 cm² (24 × 24 cm² for axials), slice thickness = 5 mm, and number of averages = 1. The box overlaid on the coronal images indicates a region 16 cm square, corresponding to the size of the ROU over which less than 30% deviation was predicted. The most distorted grid element (in the upper corners of the box) in this region for the neck coil image was lengthened by 28% compared to the grid elements at the center of the image. The measured efficiencies at the center of the ROU for the G_x , G_y , and G_z axes were found to be 0.40 mT/m/A, 0.35 mT/m/A, and 0.35 mT/m/A, respectively. The coronal grid image obtained using the neck coil also has the edge of the coil

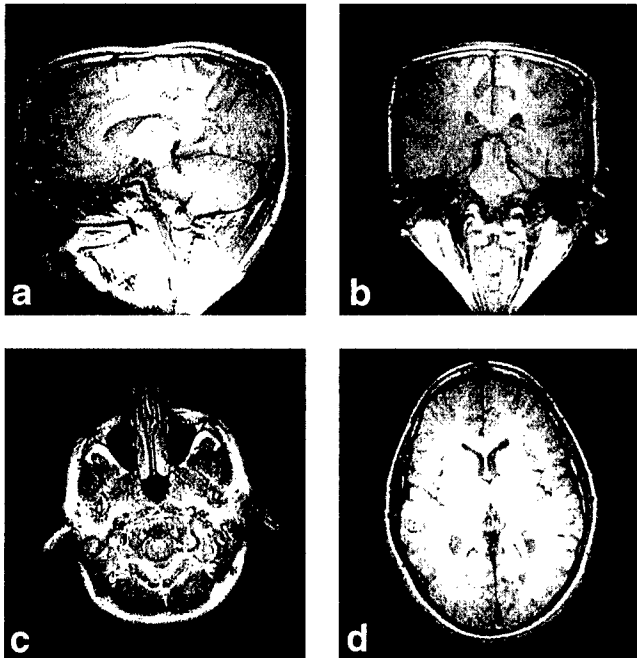


FIG. 12. Spin-echo images of the neck of a human volunteer collected at 1.5T using the neck gradient coil set. Sequence parameters common to all images were: TE/TR = 30/500 msec, number of averages = 2, matrix = 256×256 , slice thickness = 5 mm. The sagittal and coronal slices were collected with a 36-cm FOV, whereas the axial slices were collected using a 24-cm FOV. The subject was positioned such that his eyes were even with the edge of the coil. Image **c** corresponds to subject anatomy 2 cm beyond the physical edge of the coil. Image **d** corresponds to a position approximately 5 cm within the coil. A shielded birdcage RF coil was used in all cases.

indicated. The region of expected 30% deviation extends 2.5 cm beyond the edge of the coil, as predicted.

Figure 12 shows images of human subjects collected at 1.5T. Images were collected using a spin-echo sequence with the imaging parameters indicated in the figure captions. The subject was positioned with eyes at the physical edge of the coil such that the brain was within the ROU. Image distortions at the periphery of the head are clearly visible in both the sagittal and coronal images. The severe distortion in the neck region is expected, as the gradient strength drops quickly with the distance outside the coil. A shielded volume birdcage RF coil specifically tuned to operate within the gradient coil was used. The use of a copper mesh shielding for the RF coil created severe eddy currents, and as a result the maximum gradient strengths had to be limited to 44 mT/m for these scans.

Figure 13 shows a series of coronal and axial spin-echo images of the human neck collected in the same scanner. In these images the subject was positioned all the way into the coil until the shoulders came into contact with the coil edge. Two 3-inch RF surface coils were placed on either side of the neck and operated as a phased-array. The pulse sequence was not optimized for use in the neck, where motion is the cause of the ghosting artifacts visible on the coronal images.

DISCUSSION

The power of the CCMI method was fully exploited in the design of a very high strength three-axis gradient coil capable of imaging the human neck in the vicinity of the carotid arteries. The design was chosen as a compromise between speed and strength, intended to offer significant improvements in both fast-pulse sequences (such as EPI and FSE) as well as high-resolution diffusion and velocity-encoding sequences.

There are three good designs in the literature (reports in which gradient coils were designed, built, and tested on human subjects) against which this gradient coil can be directly compared, and they are summarized in Table 4. The innermost axis of each design has been listed in each case. The efficiency values have been scaled to correspond to a fixed inductance of 780 μ H for each design; however, the fact that the radii and ROU sizes of the respective designs are different should still be kept in mind when comparing the efficiency values. It is clear from Table 4 that the design presented here has advantages in imaging in the vicinity of the edge of the coil. This design is intrinsically more efficient than all but the Alsop design; furthermore, the edge design is the only one capable of

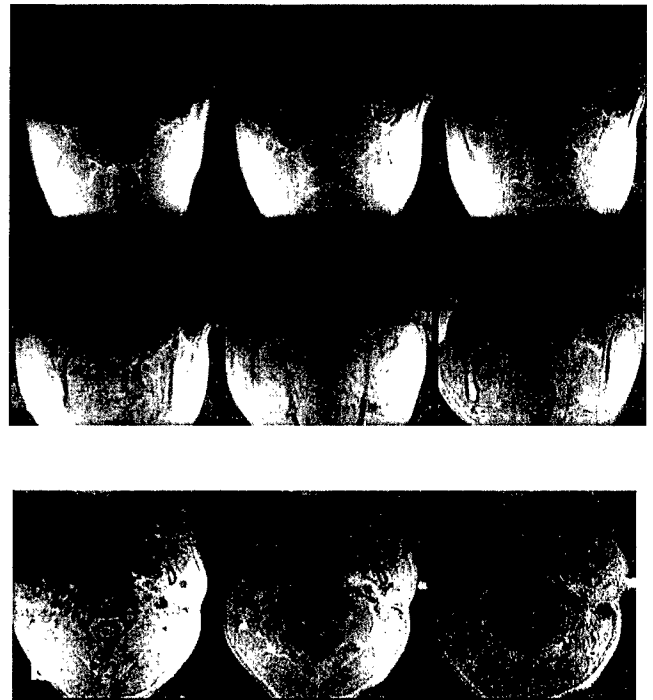


FIG. 13. Spin-echo images of a human volunteer collected at 1.5T using the neck gradient coil set. Sequence parameters common to all images were: TE/TR = 9/800 msec, number of averages = 1, FOV = 16×16 cm, matrix = 256×192 , slice thickness = 5 mm, slice spacing = 5 mm. The subject was positioned such that his shoulders were in contact with the edge of the coil. The axial slices in **b** were obtained with the left image collected approximately 6 cm in from the edge of the coil and the subsequent images moving further in. This is the vicinity of the carotid bifurcation. Two 3-inch surface RF coils were used in phased-array mode in all images. The signal falloff with slice position evident in **b** is due to the sensitivity falloff away from the surface RF coils.

Table 4
Selected Head Gradient Coil Designs From the Literature

Design	Radius (inner)	ROU (5%)	δ (5%)	L [μ H]	η [mT/m/A]
Abduljalil et al. (1994)	13.6 cm	~15 cm	~9 cm	780	0.35
Alsop et al. (1996)	16 cm	~16 cm	~9 cm	780	0.59
Bowtell et al. (1999)	19 cm	~18 cm	~10 cm	780	0.13
Edge design (Gx)	16 cm	~12 cm	~0 cm	780	0.40

imaging inferior to the carotid bifurcation in human subjects.

The attainment of edge gradient coil designs represents a significant advance; however, the construction and characterization of a workable three-axis coil set that is truly compatible with human scanning is equally important. The completed coil is capable of handling the continuous application of the full output of most clinical amplifiers with only modest water cooling. This ability is very important because it allows sequences to truly utilize the strength and speed improvements offered by this design.

The results of eddy current measurements conducted with this unshielded coil were for the most part encouraging. For the transverse axes, the induced eddy current gradient fields were measured to be very small prior to compensation, and negligible (for routine imaging applications) afterwards. The response of the z axis was dominated by a large transient B_z field component. It is possible to implement a B_z compensation coil on the 4T scanner and this is a likely direction for future work with this system.

The performance improvements available with this coil set were demonstrated in imaging experiments that progressed from phantoms to humans. The predicted uniformity was achieved over a region extending outside of the coil, and this was used to advantage in the collection of the human neck images. It was also demonstrated that the coil could provide usable images of the brain for subjects positioned with eyes just outside the physical edge of the coil. This should represent an interesting advantage for the fMRI applications referred to in the introduction. The issue of magnetostimulation thresholds in humans when using this coil has been investigated by the authors and will be reported in a separate publication.

ACKNOWLEDGMENTS

B.A.C. was supported by a Natural Sciences and Engineering Research Council of Canada postgraduate scholarship. B.K.R. holds the Barnett-Ivey-HSFO Research Chair from the Heart and Stroke Foundation of Ontario.

REFERENCES

- Steinman DA, Rutt BK. On the nature and reduction of plaque-mimicking flow artifacts in black blood MRI of the carotid bifurcation. *Magn Reson Med* 1998;39(4):635-641.
- Shinnar M, Fallon JT, Wehrli S, Levin M, Dalmacy D, Fayed ZA, Badimon JJ, Harrington M, Harrington E, Fuster V. The diagnostic accuracy of ex vivo MRI for human atherosclerotic plaque characterization. *Arteriosclerosis, Thrombosis, and Vascular Biology* 1999; 19(11):2756-2761.
- Callaghan PT. Principles of nuclear magnetic resonance microscopy. New York: Oxford University Press, 1991.
- Gati JS, Menon RS, Ugurbil K, Rutt BK. Experimental determination of the BOLD field strength dependence in vessels and tissue. *Magn Reson Med* 1997;38:296-302.
- Chronik BA, Rutt BK. Constrained length minimum inductance gradient coil design. *Magn Reson Med* 1998;39:270-278.
- Turner R. Minimum inductance coils. *J Phys E* 1988;21:948-952.
- Turner R. Gradient coil design: a review of methods. *Magn Reson Imag* 1993;11:903-920.
- Chu KC, Rutt BK. MR gradient coil heat dissipation. *Magn Reson Med* 1995;34:125-132.
- Chronik BA, Alejski A, Rutt BK. Design and fabrication of a three-axis multilayer gradient coil for magnetic resonance microscopy of mice. *MAGMA* 2000;10:131-146.
- Alsop DC, Connick TJ. Optimization of torque-balanced asymmetric head gradient coils. *Magn Reson Med* 1996;35:875-886.
- Abduljalil AM, Aletras AH, Robitaille P-ML. Torque free asymmetric gradient coils for echo planar imaging. *Magn Reson Med* 1994;31:450-453.
- Bowtell R, Peters A. Analytic approach to the design of transverse gradient coils with co-axial return paths. *Magn Reson Med* 1999;41: 600-608.



ELSEVIER

Magnetic Resonance Materials in Physics, Biology and Medicine 10 (2000) 131–146

MAGMA

Magnetic Resonance Materials in
Physics, Biology and Medicine

www.elsevier.com/locate/magma

Design and fabrication of a three-axis multilayer gradient coil for magnetic resonance microscopy of mice

Blaine Chronik^{a,c}, Andrew Alejski^c, Brian K. Rutt^{a,b,c,*}

^a Department of Physics and Astronomy, University of Western Ontario, Ont., Canada

^b Department of Diagnostic Radiology and Nuclear Medicine, University of Western Ontario, Ont., Canada

^c Imaging Research Laboratories, The John P. Robarts Research Institute, P.O. Box 5015, 100 Perth Drive, London, Ont., Canada N6A 5K8

Received 6 September 1999; received in revised form 3 January 2000; accepted 5 January 2000

Abstract

There is great interest in the non-destructive capabilities of magnetic resonance microscopy for studying murine models of both disease and normal function; however, these studies place extreme demands on the MR hardware, most notably the gradient field system. We designed, using constrained current minimum inductance methods, and fabricated a complete, unshielded three-axis gradient coil set that utilizes interleaved, multilayer axes to achieve maximum gradient strengths of over 2000 mT m⁻¹ in rise times of less than 50 μs with an inner coil diameter of 5 cm. The coil was wire-wound using a rectangular wire that minimizes the deposited power for a given gradient efficiency. Water cooling was also incorporated into the coil to assist in thermal management. The duty cycle for the most extreme cases of single shot echo planar imaging (EPI) is limited by the thermal response and expressions for maximum rates of image collection are given for burst and continuous modes of operation. The final coil is capable of the collection of single shot EPI images with 6 mm field of view and 94 μm isotropic voxels at imaging rates exceeding 50 s⁻¹. © 2000 Elsevier Science B.V. All rights reserved.

Keywords: Gradient coil; Magnetic resonance imaging; Microscopy; Multilayer; Mouse; Echo planar imaging; Power deposition

1. Introduction

High speed magnetic resonance (MR) microscopy in murine models of human disease and function is of fundamental importance in a range of biomedical research areas [1,2]. Non-destructive 'MR histology' of brain lesions in small animals [3,4], studies of the biophysical basis of fMRI in a murine model [5], in vivo diffusion-tensor microscopy [6], microscopic studies of in utero murine embryos [7], in vivo microscopic studies of the murine carotid artery [8], and murine cardiac magnetic resonance imaging (MRI) [9,10] are all active areas of research requiring in vivo magnetic resonance microscopy. Cardiac MRI in the mouse heart is technically very challenging because of the combination of small organ size (< 8 mm) and very fast heart rate (> 450 beats per min). The technical demands

placed on the system hardware in these applications are extreme, particularly the gradient coil requirements. The small size of the mouse is of course an advantage in that it allows the use of small, customized gradient coils. This paper discusses the special considerations involved in designing such mouse-specific coils, and details the design, construction, and imaging performance of one specific design.

Above all, very high gradient strengths are required to achieve the high spatial and temporal resolution necessary for advanced MRI of small animals. Using the fundamental relationship between gradient strength, sampling rate, and image field of view (FOV) [11], it is easily found that a 6 mm FOV requires a gradient strength of 2000 mT m⁻¹ when using a receive signal sweep width of 500 kHz, typical of the maximum sampling rate of recent generation MRI systems. This gradient strength is approximately two orders of magnitude greater than that produced by the whole-body gradients of current clinical scanners; therefore, it is clear that a customized gradient coil is necessary for high quality mouse organ imaging.

* Corresponding author. Tel.: +1-519-6635777, ext.: 33408; fax: +1-519-6633403.

E-mail address: brutt@irus.rii.on.ca (B.K. Rutt)

For any given amplifier and gradient coil combination, the maximum rise time of the gradient waveforms is proportional to the coil inductance (L). For this reason, coils are often designed with minimum inductance for a given gradient strength. This minimizes the total time spent in switching any gradient waveform train, thereby minimizing TR, TE, and other critical timing parameters. The switching speed requirements for high field mouse imagers are especially extreme. For example, at 7 T and above, the T2* of murine myocardial tissue is 9 ms or less and the T2* of gray and white matter are 18 and 12 ms, respectively [12,13]. Acquiring a 64-lobe echo planar imaging (EPI) train within 20 ms, using 500 kHz flat-top-only sampling and a 6 mm FOV, will require a minimum efficiency of 2000 mT m⁻¹ and a maximum inductance of 200 μH. This inductance limit is up to an order of magnitude lower than that of typical clinical gradient coils.

A final and often overlooked consideration is the gradient coil duty cycle, determined by the thermal response of the coil, which is in turn largely determined by the resistance of the coil load. Because many researchers wish to connect their mouse-sized gradient coil to a normal clinical gradient driver system, the coil should be capable of carrying high rms currents (in the range of 100 A). For resistances between 0.5 and 1 Ω, this corresponds to power deposition of 5–10 kW in a physically small coil (low thermal mass) and there is the potential for a significant heating problem and a limited duty cycle. Because of the small coil size needed to achieve the strength and speed, the area available for wire cross-section is greatly reduced. In the following sections, it will be demonstrated that simply scaling down an existing body gradient design is insufficient when this power deposition issue is considered. The way to achieve the required performance is to move to multilayer coil designs while using rectangular wire to maximize copper cross-section. This method in turn creates the need to specifically consider an interleaving strategy for organizing the many layers of the coil into a complete three-axis design. We outline a design strategy for interleaved multilayer, rectangular wire gradient coils in this paper, and show the experimental performance of a three-axis mouse-optimized coil created using this strategy.

2. Theory

2.1. Gradient coil scaling

As noted in Section 1, the advantage of a customized mouse gradient coil insert is that it can be built with a small radius just large enough to encompass the mouse and radiofrequency (RF) coil assembly. We decided to design our prototype coil with an inner physical radius

of 2.5 cm, and therefore the innermost winding layer of the coil would have a radius of approximately 3 cm. This is one order of magnitude smaller than the typical for normal whole body gradient coils. The first question we sought to answer was what sort of performance could be expected simply by scaling a human whole-body gradient coil down to mouse size.

The four most important quantities defining the performance of a gradient coil are the efficiency (η), inductance (L), resistance (R), and temperature rise (ΔT) for a given input current. The general laws for scaling these quantities from values at radius a_0 and peak winding density σ_{w0} (defined as the number of wires per centimeter used to wind the coil at the densest region of the wire pattern) to new radius a and density σ_w are [14]:

$$\eta = \eta_0 \left(\frac{\sigma_w}{\sigma_{w0}} \right) \left(\frac{a_0}{a} \right) \quad (1)$$

$$L = L_0 \left(\frac{\sigma_w}{\sigma_{w0}} \right)^2 \left(\frac{a}{a_0} \right)^3 \quad (2)$$

$$R = R_0 \left(\frac{\sigma_w}{\sigma_{w0}} \right) \left(\frac{a}{a_0} \right)^2 \left(\frac{A_{w0}}{A_w} \right) \quad (3)$$

where A_w is the cross-sectional area of the wire. Resistance is of importance in this application because of its influence on the thermal response of the coil. It should be noted that Eq. (3) is correct for dc resistances only, and that at high switching frequencies, both skin depth and wire proximity will affect the scaling. The average temperature increase of a coil is proportional to the resistance and inversely proportional to the total volume of the coil wall (assuming that the material properties remain constant with temperature). Assuming that the volume scales as the cube of the radius and that A_w scales inversely with the square of the winding density (as they would for uniformly scaled coil and wire dimensions), the change in temperature at any constant rms current is expected to scale as:

$$\Delta T = \Delta T_0 \left(\frac{\sigma_w}{\sigma_{w0}} \right)^3 \left(\frac{a_0}{a} \right). \quad (4)$$

Fig. 1 contains plots of η , L , and ΔT as a function of radius for several fixed values of winding density. The starting point used to generate these plots was a hypothetical body-sized gradient coil design with a radius of 30 cm, efficiency of 0.12 mT m⁻¹ A⁻¹, inductance of 1200 μH, resistance of 500 mΩ, temperature change of 5°C at an rms current of 100 A, and a maximum winding density of 2 cm⁻¹.

For a clinical amplifier system capable of delivering a peak current of 200 A, the gradient efficiency required to achieve 2000 mT m⁻¹ is 10 mT m⁻¹ A⁻¹. Examining Fig. 1a we note that a winding density of 16 cm⁻¹ or higher is required to achieve a gradient efficiency of 10 mT m⁻¹ A⁻¹ for a radius of 3 cm. This is itself a

limitation in that constructing such a dense wire pattern is quite difficult with standard methods; furthermore, the wire would have to be of such small cross-section as to preclude the high peak currents (of the order of 200 A) required. Construction methods developed in our laboratory currently produce a maxi-

imum wire density of approximately 8 cm^{-1} on a single transverse layer, but according to the efficiency plot this produces approximately half of the required strength. One way to reach higher effective density wire patterns with lower density fabrication methods is to divide the winding of a single layer across two or

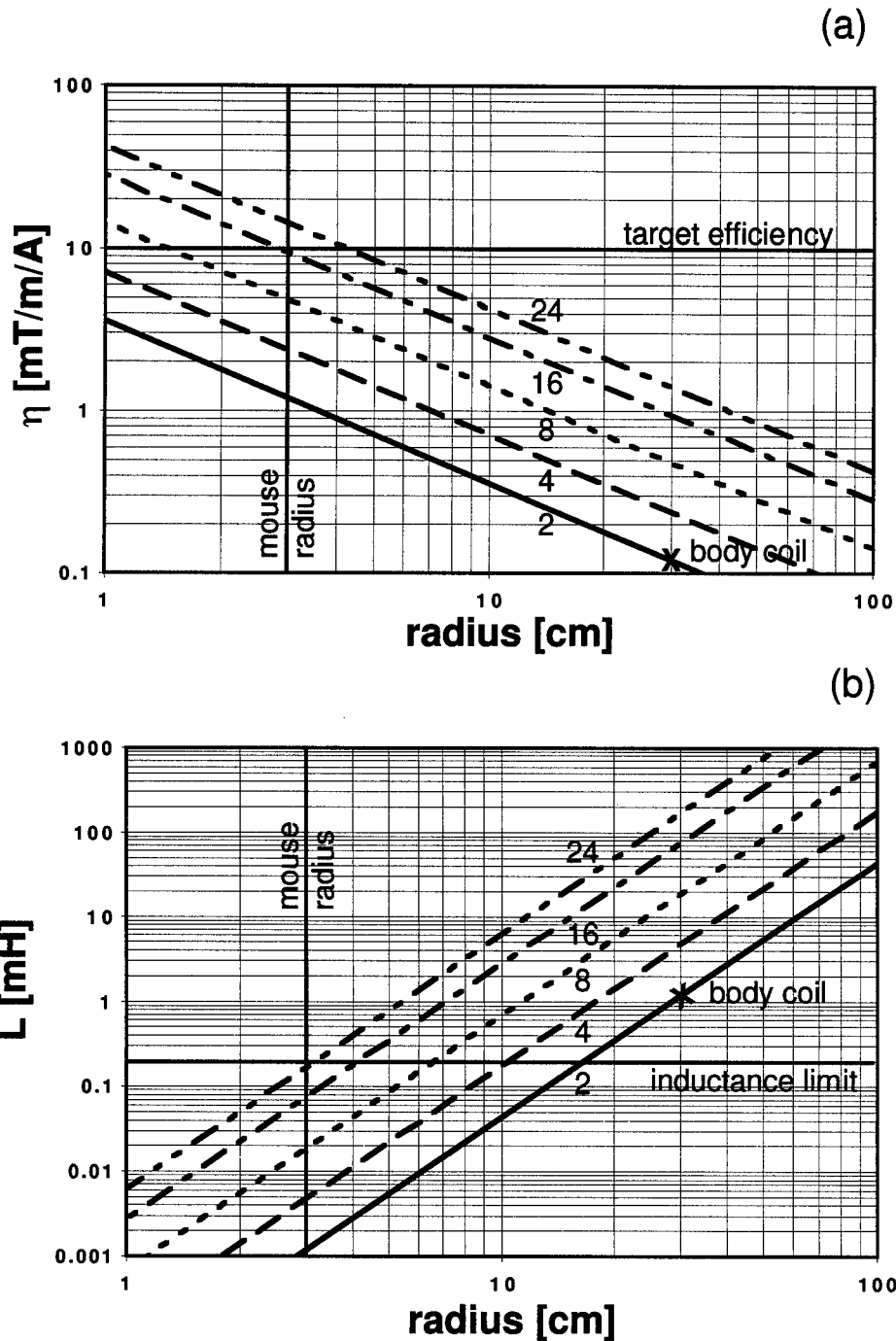


Fig. 1. Plots of (a) gradient coil efficiency; (b) inductance; and (c) average temperature rise, as functions of radius for five different fixed values of maximum winding density. The hypothetical body coil design upon which all the scalings are based is indicated by the cross and the effective radius of the proposed mouse coil is represented by the vertical line. The position of the target efficiency (a) and maximum allowed inductance (b) are indicated by the horizontal lines on the respective plots.

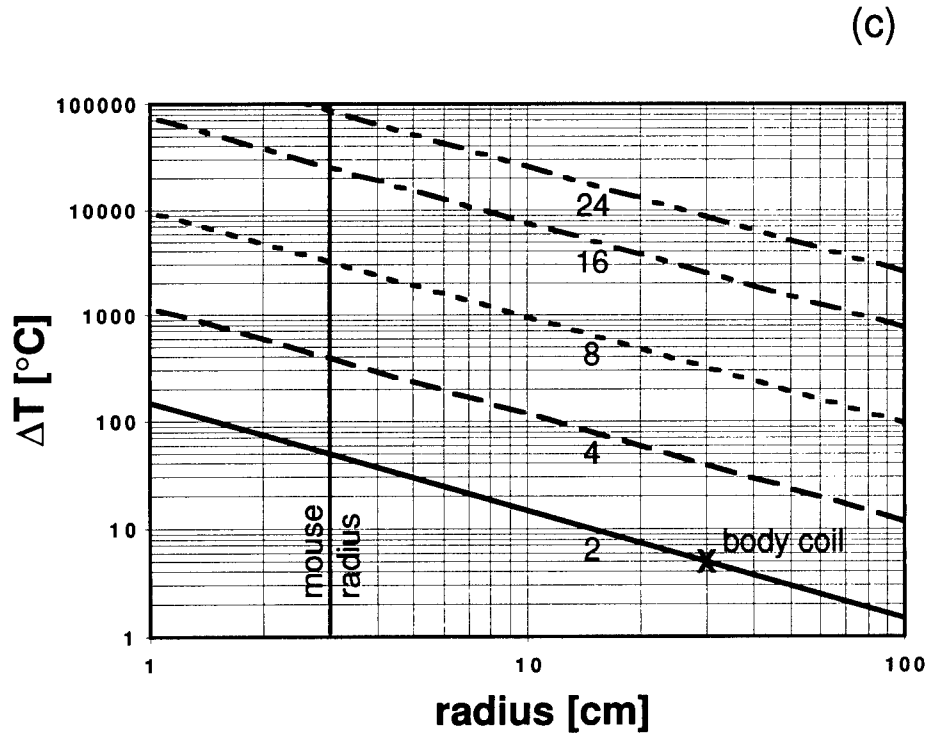


Fig. 1. (Continued)

more layers, each individual layer wound at the highest density achievable.

The inductance variation depicted in Fig. 1b indicates that coils at the highest σ_w values considered fall below the 200 μH upper limit allowed for this application. The figure indicates that a single layer design wound at 8 cm^{-1} would have an inductance of 20 μH at a 3 cm radius. To a first approximation, the inductance of a double layer 8 cm^{-1} coil operated in series is equivalent to that of an equal radius single layer design wound to 16 cm^{-1} , i.e. 80 μH at a 3 cm radius; therefore, it is expected that the two-layer configuration needed to achieve the efficiencies discussed in the previous paragraph will also result in inductance values below the specified upper limit.

The thermal response of small, high winding density coils represents the dominant practical limitation, as is evident from Fig. 1c. Scaled to the desired mouse coil radius, all winding densities result in steady-state coil temperature orders of magnitude higher than what would be tolerable. For this reason, we expect that all mouse coils meeting the specifications outlined will have extreme duty cycle limitations unless special effort is made to minimize the temperature increase. We argue in this paper that this consideration leads to a dominant requirement for minimum resistance configurations, which requires the combination of rectangular cross-section wire with multilayer designs in order to achieve the smallest resistance for a given effective winding density.

2.2. Heating

The temperature response of a gradient coil when driven by an rms current (I_{rms}) can be approximated by an exponential approach to an equilibrium temperature [15] and the following equation relating temperature (T) and time (t) applies to both heating and cooling of the coil:

$$T = T_0 + \Delta T_{\text{ss}} \left[1 - \exp\left(\frac{-t}{\tau}\right) \right] \quad (5)$$

where ΔT_{ss} is the steady-state temperature change at the measurement location, T_0 the temperature at the start of the measurement, and τ is a time constant characteristic of the axis and the degree of cooling applied. For the heating phase, a steady-state heating parameter can be defined:

$$k_{\text{h}} = \frac{\Delta T_{\text{ss}}}{I_{\text{rms}}^2 R} \quad (6)$$

where I_{rms} is the rms current applied and R is the resistance of the axis. To a first approximation, ΔT_{ss} is simply proportional to the input power while τ is independent of it [15]; therefore, assuming that resistance is constant over the range of temperatures in the experiment, k_{h} is a constant for each axis and rate of water cooling, and it can be used to calculate the steady-state temperature increase for any input power.

The fact that τ is independent of the input power means that it is an operationally independent parameter

that can be used to define the transition between two modes of coil operation. These two modes require individual consideration when calculating duty cycles. To achieve scan repetition (TR) times much less than τ , the coil may be operated in a burst mode, during which it is run at high power for a short time (t_b , burst time) and allowed to heat-up at an unsustainable rate (Fig. 2a). This would then have to be followed by a dead time, t_d , during which the coil is allowed to cool sufficiently before starting another burst phase. This operation mode would be required when imaging at very high rate is important but required only for short blocks of time; an example might be cardiac imaging. For this mode, the maximum number of single shot EPI images that can be collected during each burst phase was calculated as a function of the pulse sequence and coil thermal parameters such that the coil temperature increases were maintained at tolerable levels.

For scan times on the order of τ and longer, the coil must be run in a sustainable fashion, and the steady-

state thermal response is of primary importance. In this continuous mode (Fig. 2b), the minimum TR for repeated single shot EPI imaging was calculated as a function of the pulse sequence parameters such that the corresponding rms current resulted in a tolerable steady-state temperature increase. Burst and continuous mode operation are analyzed in more detail in the following paragraphs.

The purpose of burst mode operation is to allow the images to be collected at the minimum sequence repetition time defined by timing rather than by heating considerations. The length of time that this can be sustained (t_b) is determined by the rms current applied during the burst (I_{rms_b}), the temperature excursion allowed to develop during the burst (ΔT_b), and the heating parameters of the coil. Ignoring the heating contributions from the phase encode and slice select axes, the rms current that exists during each single shot EPI collection can be approximated as (see derivation in Appendix A):

$$I_{rms_b} \cong \left(\frac{2\pi SW}{\gamma \eta_r FOV_r} \right) \sqrt{\frac{N_p}{TR} \left\{ \frac{2 L_r}{3 V} \frac{2\pi SW}{\gamma \eta_r FOV_r} + \frac{N_r}{SW} \right\}^{1/2}} \quad (7)$$

where, SW is the receive signal sweep width, γ the gyromagnetic ratio of the nucleus, η_r the gradient efficiency of the readout axis, FOV_r the field of view in the direction of the readout axis, N_p the number of phase encode lines, TR the time between EPI collections, L_r the inductance of the readout axis, V the voltage applied during gradient slewing, and N_r the number of readout points collected. Applied for an infinite amount of time, this rms current would typically result in an extremely high steady-state temperature increase found by solving Eq. (6) for the temperature:

$$\Delta T_{ss_b} = k_h I_{rms_b}^2 R. \quad (8)$$

This steady-state temperature increase is used within Eq. (5) to obtain the coil temperature as a function of time. For burst mode operation, the initial slope of the temperature response is critical and the temperature curve can be approximated for $t_b \ll \tau$ to give:

$$\Delta T_b = \frac{\Delta T_{ss_b}}{\tau} t_b \quad (9)$$

where the temperature increase at any given instant is defined as $\Delta T_b = T - T_0$. The maximum number of images (N_{burst}) that can be collected within a single burst is simply the burst time divided by the minimum sequence TR. Solving for t_b via Eqs. (8) and (9) and dividing by TR we obtain:

$$N_{burst} = \frac{\Delta T_b}{(I_{rms_b})^2 R} \frac{\tau}{TR} \quad (10)$$

There is an implicit frequency dependence contained within the resistance in Eq. (10); however, as will be

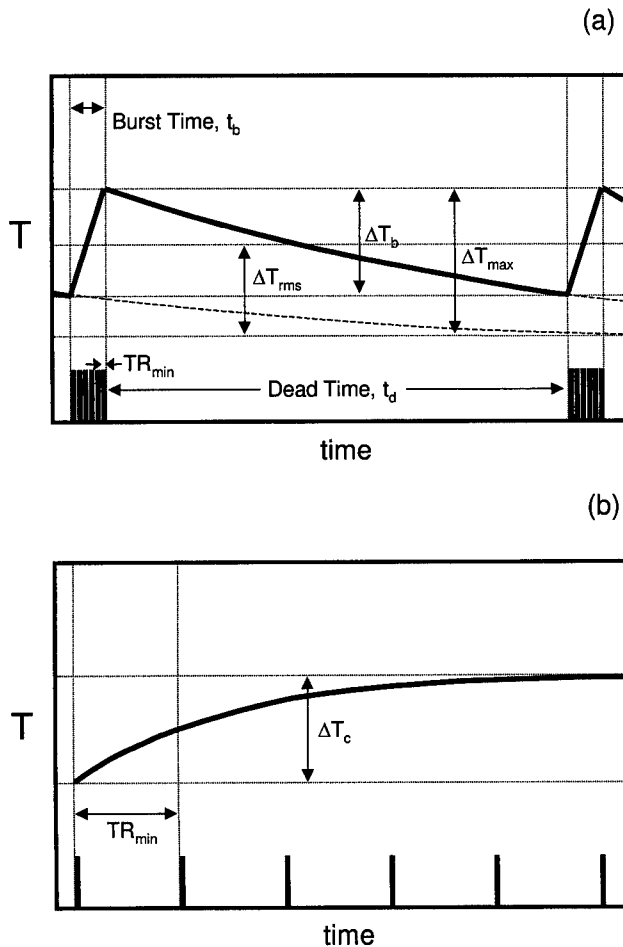


Fig. 2. Schematic diagrams of the temperature variation during (a) burst mode; and (b) continuous mode operation. Solid vertical bars at the bottom of each diagram represent the acquisition of a single EPI image.

noted in the following sections, the resistance of the specific wire used in this construction varied by approximately 5% over the frequency range (1–10 kHz) expected for MRI applications and therefore this effect was neglected.

Eqs. (7) and (10) yield the following general expression for the maximum number of images that may be collected as a function of the pulse sequence parameters, the maximum tolerable ΔT_b , and the readout axis heating parameters (k_h and τ):

$$N_{\text{burst}} = \frac{\Delta T_b}{N_p} \frac{\tau}{k_h R} \left(\frac{\gamma \eta_r \text{FOV}_r}{2\pi \text{SW}} \right)^2 \left\{ \frac{2 L_r}{3 V} \frac{2\pi \text{SW}}{\gamma \eta_r \text{FOV}_r} + \frac{N_r}{\text{SW}} \right\}^{-1} \quad (11)$$

Using this expression, N_{burst} was computed as a function of the FOV for different imaging parameters and choice of gradient axis used for readout. Note that TR has factored out of the expression. Although shorter TRs allow faster imaging, they also result in shorter allowable t_b ; therefore, the two effects cancel each other and the number of images allowed stays constant. The last piece of data that is necessary to characterize burst mode operation is the length of dead time (t_d) required between bursts. One simple specification is to require that the rms current calculated over an entire cycle ($t_b + t_d$) lead to an rms temperature increase (ΔT_{rms}) over baseline equal to ΔT_b , the burst time temperature increase (see Fig. 2a). In this case, the following simple relationship between t_b , t_d , and τ can be shown to hold:

$$t_b + t_d = \tau. \quad (12)$$

Eq. (12) indicates that imaging can only be done for a period of t_b once every heating time constant of the readout axis. The long-term average rate of image collection (i.e. averaged over many burst cycles) is independent of τ because although a smaller τ allows fewer images to be collected per burst (Eq. (10)), it also allows more burst periods per unit time (Eq. (12)) and the two effects cancel.

Continuous mode operation is governed simply by adjusting the single shot EPI image repetition time, TR, such that the coil can be sustainably operated. A tolerable steady-state temperature excursion, ΔT_c , must be chosen (Fig. 2b), and Eq. (6) is used to calculate the corresponding I_{rms} current. Eq. (7) is solved for TR and combined with Eq. (6) to yield:

$$\text{TR}_{\text{min}} = N_p \left(\frac{k_h}{\Delta T_c} \right) \left(\frac{\gamma \eta_r \text{FOV}_r}{2\pi \text{SW}} \right)^2 \left\{ \frac{2 L_r}{3 V} \frac{2\pi \text{SW}}{\gamma \eta_r \text{FOV}_r} + \frac{N_r}{\text{SW}} \right\}. \quad (13)$$

Using this expression, minimum TR was computed as a function of the FOV for different imaging parameters and choice of gradient axis used for readout.

3. Methods

3.1. Optimized layer design

With the need for multilayer, rectangular wire designs identified, there remains the issue of finding the best design for the individual layers. The three axes of a gradient coil set can be broken into two design groups, the transverse (X and Y) and the longitudinal (Z) axes. The X and Y axes use the same design, one obtained from the other via a 90° rotation about the longitudinal axis. The strategy for selecting the optimal design is the same for both transverse and longitudinal coils and we will focus on the former.

All designs were obtained using the method of constrained current minimum inductance (CCMI) reported previously [16]. Specifically, the CCMI method is a solution for the minimum inductance current density satisfying a set of field constraints, subject to a set of constraints on the current density itself. The current constraints define the region over which the current is allowed to flow and therefore specify the design's aspect ratio, defined as the ratio of the coil's total length to its diameter. The field constraints are placed in such a way as to define the region of uniformity (ROU). By varying both the arrangement of the field constraints and the limits of the current constraints, designs can be obtained for any combination of ROU and aspect ratio, and for each design the gradient efficiency, inductance and winding density can be calculated. The simplicity and computational efficiency of the CCMI method offer an unique opportunity to directly model all possible designs in the ROU and aspect ratio parameter space. By plotting design performance figures over this space at the winding density and radius of the desired coil, the entire range of achievable performance is made apparent while trade-offs between imaging region size and coil size can be rapidly visualized and understood. The choice of the optimal design then becomes a straightforward matter of locating the best coordinate in this space for the given application.

An additional complexity in our application was the requirement for a small side aperture (1 cm in diameter) for lateral sample/probe access. This feature required the application of current constraints (via CCMI) about the z centre of the design and the effects of this process will be described in more detail elsewhere.

3.2. Interleaving

In Section 2, it was noted that a multilayer configuration would be needed in this application to achieve the required gradient strengths. It was also suggested that rectangular wire would be of significant benefit in minimizing the resistance for any winding density, and therefore maintaining tolerable thermal response for the

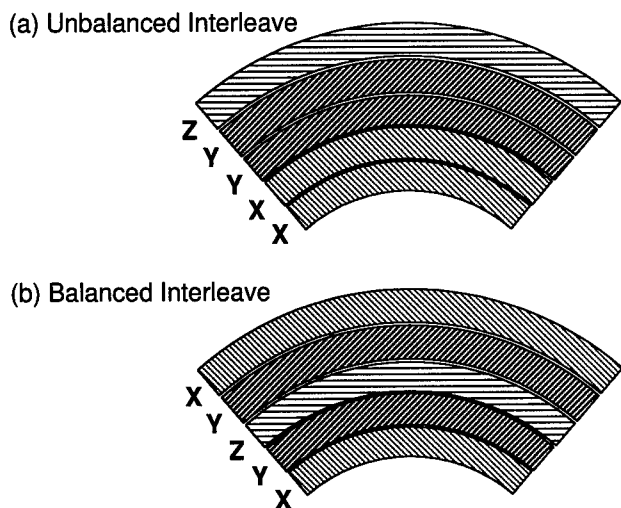


Fig. 3. Schematic diagrams of five layer, three-axis coils interleaved in (a) unbalanced; and (b) balanced configurations.

coil. The complicating issue in small radius, multilayer coils with rectangular wire is that the thickness of each winding layer becomes a significant fraction of the radius. This is not a major concern when only one axis of a gradient coil is being built; however, it becomes a problem when all axes of the coil are being considered together. In most imaging applications, it is often not useful to have one axis significantly stronger than the others. If a multilayer coil is simply wound consecutively from the first axis to the last as in Fig. 3a, the width of the layers will force the effective radius of the outermost axis to be significantly larger than the innermost, resulting in an appreciable performance imbalance. The alternate approach is to interleave the layering order in such a way as to equalize the strength, an example of which is shown in Fig. 3b. The interleaving question becomes that of determining the effects of different distributions of the layers of the three axes into the allowed radial positions.

In preliminary fabrication tests for this design, it was determined that an entire single layer, including return paths and potting considerations, could be achieved with a wall thickness of 7 mm. With the radius of the inner bore set at 2.5 cm and assuming a five-layer construction (the choice of a five-layer construction is explained in Section 4), the outer radius of the coil would be 6.0 cm. The effective wire pattern radius for each layer was chosen to be 2.75 mm larger than the inner radius of that layer, yielding radii of 2.775, 3.475, 4.175, 4.875, and 5.575 cm for layers one to five, respectively. There are 15 distinct possibilities for distributing the three axes over the five layers and each was modeled by scaling the chosen transverse and longitudinal coil designs to the above radii. The winding density was set at 8 cm^{-1} for each transverse layer and at 10 cm^{-1} for the longitudinal layer. The two

layers of each transverse axis were modeled as a series connection. The field gradients and inductances were calculated from the resulting wire patterns using Biot–Savart law and Neumann formula, respectively [17].

3.3. Fabrication

The fabrication process was developed and carried out completely within our laboratories over a 3-month period. Predominantly carried out by a single individual, the estimated total cost of the project was \$20 000 (CAD). The general procedure has been developed during the construction of several previous gradient coils and was customized as required for this project. Of special concern was the production of a very robust gradient coil capable of operating at high currents within a typical clinical scanner. For this reason special attention was paid to the potting procedures as described below.

The wire used was composed of 119 strands of 36 AWG copper wire arranged in a Litz braiding to produce a rectangular cross-section wire $0.8 \times 3.5 \text{ mm}^2$ in size with an equivalent gauge of 16 AWG (New England Electric Wire Corp., New England, USA). Individual conducting elements were coated with insulation heat rated to 150°C . Litz wire was used in place of solid copper to reduce resistance at frequencies of several kilohertz, expected to be the dominant operating frequency of the coil for high speed imaging sequences. The dc resistance of the wire was $13 \text{ m}\Omega \text{ m}^{-1}$. The multistrand formation of Litz wire also improved its workability, reducing wire memory and allowing a minimum bending radius of several millimeters. In comparison, winding the transverse axis patterns with equal-area solid copper wire was found to be exceedingly difficult.

The wire patterns for each layer were CNC milled into the outer surfaces of teflon cylinders using a three-axis cylindrical mill developed and constructed within our laboratories for the specific purpose of gradient coil fabrication. A complete pattern for a single transverse layer could be cut in approximately 6 h in a single pass. Grooves were milled 1.75 mm deep (half the height of the wire) and precisely 0.8 mm wide such that when the wire was pushed into the grooves, it would be held in the plastic former while extending 1.75 mm out of the cylinder wall.

The winding of the layers proceeded relatively slowly, typically taking a single person an average of 18 h to finalize each layer. After winding each layer, a light coating of epoxy was applied to help hold the wire in place and to fix a type-E thermocouple over the wire at the location of maximum wire density. These thermocouples allow active temperature monitoring of the hottest areas of the coil, thereby permitting thermal characterization of the coil as discussed below, as well

as the continual monitoring of the coil during operation to prevent accidental damage. The pattern for each layer was wound with one continuous length of wire to avoid the presence of solder connections within the wall of the coil, the most probable site for thermal failure in our experience. The five wound layers were then potted together into one single cylinder. A 1.5-cm thick layer containing 7 mm diameter copper tubing carrying forced water cooling at flow rates of up to 51 min^{-1} was potted around the exterior of the coil to form the outermost layer. The epoxy used for the potting (Durapot 865, Cotronics Corp., New York, USA) was specially chosen to have a very high thermal conductivity ($2.8 \text{ W m}^{-1} \text{ K}^{-1}$) so that the cylinder wall could effectively transfer heat from the wire layers to the outer cooling tubes. The epoxy was heated before potting to reduce its viscosity and the entire coil structure was mechanically agitated during the first few hours of

curing to assist the penetration of epoxy and prevent air pocket formation. The potting was accomplished in stages, one for each layer, with each stage requiring a minimum of 24 h to allow the epoxy to cure.

The aperture designed for the side of the coil was maintained during the potting procedure and then honed as a final step to assure an aperture clear bore diameter of 1 cm. Fig. 4 shows a photograph of the completed coil before the addition of the outermost cooling layer. Connections between layers were made via heavy-duty copper jumpers at the back of the coil. Thermocouple lead connectors were potted into the back wall of the coil for stability. The inner diameter was 5 cm, outer diameter was 15 cm, and total coil length (including cable connection posts and cooling connectors) was 25 cm. The completed coil weighed approximately 23 lbs.

3.4. Heating

Using thermocouples incorporated into the coil during construction, internal temperature measurements were made over time while passing 20 A dc through each axis in turn. Heating was halted when internal coil temperatures increased by 30°C . The cooling rate of the coil was measured by recording the internal temperature as a function of time after the cessation of current. The experiment was repeated for each axis for water flow rates of 0 and 4 l min^{-1} . Both ΔT_{ss} and τ were obtained by applying a least-squares fit to the experimental curves for each axis (Eq. (5)), during both heating and cooling phases.

3.5. Electrical measurements and imaging

Bench top measurements of both resistance and inductance were made at frequencies of 1 and 10 kHz using a Hewlett-Packard 4262A LCR meter.

The completed coil was directly interfaced with both a Varian-Siemens Unity INOVA 4T whole body scanner incorporating a Siemens As25 gradient driver system (peak current, 250 A; peak voltage, 600 V; Siemens Medical, Erlanger, Germany) and a 1.5 T General Electric Signa Horizon with Echospeed gradient amplifiers (peak current, 200 A; peak voltage, 1200 V, General Electric Medical Systems, Milwaukee, WI). In both scanners, 1150- μH inductors were connected in series with each axis of the coil to provide an impedance match to the amplifiers. Both systems are capable of being calibrated to the smaller impedance of the mouse coil; however, for the preliminary tests described in this paper this was not considered to be necessary. No eddy current compensation was applied for any of the sequences run. The coil was well fixed within the magnet bore in each circumstance. Individual solenoidal RF coils (18 and 34 mm in diameter)

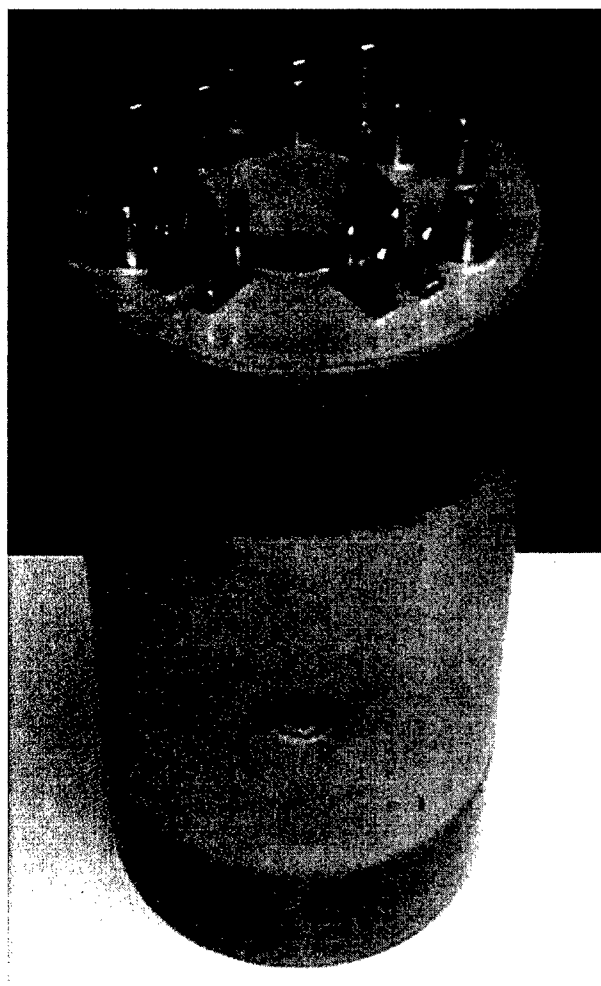


Fig. 4. Photograph of gradient coil prior to addition of outer cooling layer. Electrical jumpers connect layers within the X and Y axes in series. Six free brass electrical connections (two per axis) are visible at the top of the coil. Four thermocouple connectors are visible at the front of the top surface. The 1-cm aperture through the side is visible halfway up the front of the coil.

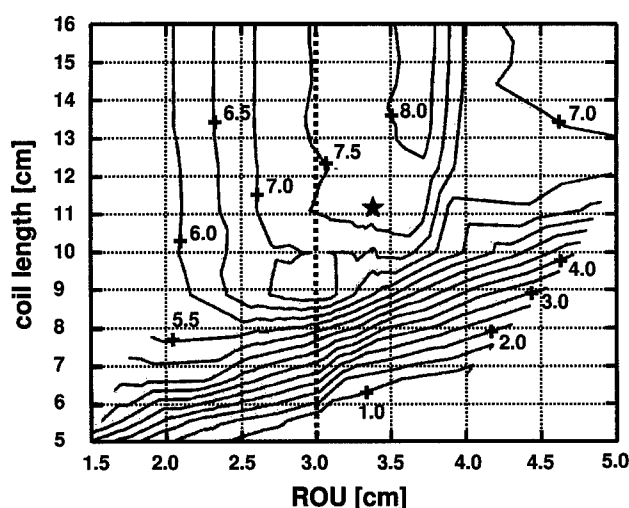


Fig. 5. Contour plot of the efficiency ($\text{mT m}^{-1} \text{A}^{-1}$) of the innermost transverse layer (radius, 2.775 cm) over axes of coil length and 30% ROU size. The position of the chosen transverse layer design is indicated by the star. The vertical line marks the minimal allowed ROU size for mouse imaging.

were constructed and tuned to resonate within the gradient coil bore for both field strengths.

The gradient efficiency was measured by imaging a precision grid phantom (square in plane grid elements of size $2 \times 2 \text{ mm}^2$) using a known current. After reconstruction, the image measurements were used in conjunction with the known phantom dimensions to adjust the gradient efficiency until the grid elements in the image were of the correct dimension.

4. Results

4.1. Optimized layer design and interleaving

Fig. 5 shows a contour plot of η in $\text{mT m}^{-1} \text{A}^{-1}$ over the parameter axes of ROU and coil length for a fixed winding density of 8 cm^{-1} and radius of 2.775 cm. The ROU for the purposes of this plot is taken to be the longitudinal length of the region within which the absolute value of the gradient inhomogeneity is less than 30%; however, the relative features of the plot are unchanged with the use of more stringent homogeneity specifications defining the ROU. For aspect ratios be-

low approximately 1.5 (coil length of approximately 8 cm on the plot), the general trend is that the most efficient designs correspond to the regions of smallest ROU and longest coil; however, the trend for aspect ratios above about 1.6 (coil length of approximately 9 cm on the plot) is that the designs get more efficient as both the coil length and ROU are increased. The dependency of η on coil length (aspect ratio) is essentially monotonic over the entire plot with increasing length resulting in more efficient designs.

For mouse imaging with minimal gradient distortion over the heart region ($< 1 \text{ cm}$ in diameter [10]) and correctable distortion over a region large enough to image the mouse body if desired ($\sim 3 \text{ cm}$ in diameter [10]) a region better than 1% homogeneity was required over 1 cm and 30% over 3 cm diameter spherical volumes (DSV). Taking 30% DSV as the primary homogeneity constraint, a line can be drawn on the design space contour plot (Fig. 5) to indicate the region of coils that can be considered. If there were length constraints for this coil, a horizontal line at that maximum length could also be added to further limit the region under consideration. In this application, there is no such constraint and the entire plot to the right of the 3 cm DSV line is allowed. The chosen design is at the point defined by a coil length of 11.1 cm and an ROU size of 3.3 cm (indicated by a star on Fig. 5). The higher efficiency region above and to the right of the selected design was excluded because of increased inductance values associated with that area of the space. The optimal layer design for the longitudinal axis was obtained in the same manner. The calculated values of σ_w , η , L and R are listed in the first row of Table 1 for the innermost winding radius of 2.775 cm. All other layers of both the X and Y axes were based on the design of Fig. 6a, each scaled to the appropriate radius while maintaining an approximately constant winding density of 8 cm^{-1} . The calculated performance value for each of these layers is also shown in Table 1. The wire patterns for a single octant of the transverse and longitudinal layers are shown in Fig. 6a and b, respectively. The layer ordering implicit in Table 1 is the optimal one as determined from the interleaving results described below.

Table 1
Summary of calculated results for individual layers

Layer	Radius (cm)	σ_w (cm^{-1})	η ($\text{mT m}^{-1} \text{A}^{-1}$)	L (μH)	R (m Ω)
1 (X)	2.775	8.3	7.8	12	67
2 (X)	3.475	8.1	6.1	23	104
3 (X)	4.175	10.0	11.0	97	200
4 (X)	4.875	7.8	4.2	60	201
5 (X)	5.575	8.2	3.9	98	275

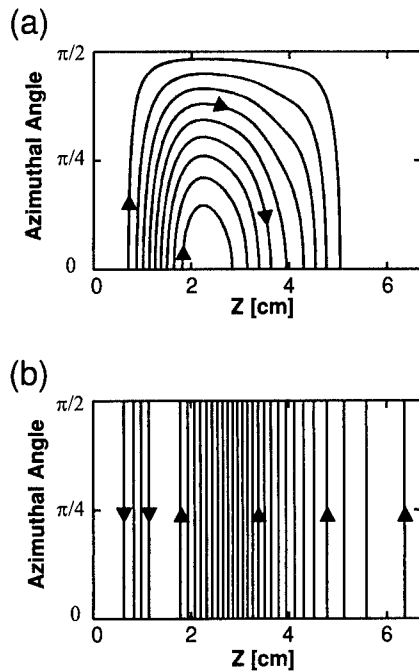


Fig. 6. Single octant wire patterns for the (a) transverse; and (b) longitudinal axes. Arrowheads indicate relative direction of current within each pattern. A region of current reversal is present on the longitudinal (z) axis only. The pattern in (a) is used for all transverse layers within the coil, shifted by 90° for the y -axis layers. The maximum winding density on the transverse and longitudinal patterns are 8 and 10 cm^{-1} , respectively.

Table 2
Calculated results for interleaving combinations

	η ($\text{mT m}^{-1} \text{ A}^{-1}$)			L (μH)		
	GX	GY	GZ	GX	GY	GZ
XXYYZ	13.9	9.2	8.2	60	161	231
XYXYZ	12.8	10.3	8.2	64	114	231
XYXZY	12.1	11.1	8.2	84	102	231
XXYZY	13.9	8.9	9.4	60	182	154
XYXZY	12.8	10.0	9.4	64	141	154
XYYZX	11.7	11.1	9.4	121	102	154
XXZYY ^a	13.9	8.1	11.0	80	259	97
XYZXY	12.1	10.0	11.0	84	141	97
XYZYX ^b	11.7	10.3	11.0	121	114	97
XZXYX	12.8	8.1	13.2	64	259	56
XZYXY	12.1	8.9	13.2	84	182	56
XZYXX	11.7	9.2	13.2	121	161	56
ZXXYY	11.1	8.1	16.5	102	259	28
ZXYXY	10.3	8.9	16.5	114	182	28
ZXYXX	10.0	9.2	16.5	141	161	28

^a Most imbalanced ordering.

^b Most balanced ordering.

Table 2 lists the calculated results for the possible layer orderings. The most unbalanced case (XXZYY) results in range of efficiency of 74% (X largest, Y smallest) and a range of inductance of 332% (Y largest X smallest). For the most balanced ordering (XYZYX),

the efficiency and inductance ranges were reduced to 14 and 25%, respectively. In this application, it was decided that the most balanced combination was best and therefore the XYZYX interleave was used.

We also investigated the benefit of adding additional layers to the designs. All possibilities were modeled, and the results summarized in Table 3. Looking at the most efficiency balanced example (XYZYXXYZ), it is seen that the average efficiency of the transverse axes increases by 29% while the average inductance increases by 242%. This may be warranted in situations where switching speed is not important or where larger inductance is needed to simplify interfacing the coil with existing amplifiers; however, in this application it was decided that the increases were not useful.

4.2. Electrical performance

The measured values for resistance and inductance of the individual layers as well as the complete axes are summarized in Table 4. The calculated values are also included for comparison. It should be noted that the relatively slow increase of resistance with frequency is expected because of the Litz wire construction. The calculated resistance values are generally lower than the experimental results because they assume zero frequency (dc) and they do not take into account the length of connecting wire within the coil or the effects of linking the wire to the brass connection posts. These effects are negligible for inductance, as indicated by the accuracy of the inductance calculation as compared to the measurements.

4.3. Heating

The results of temperature measurements as a function of time for the x axis during periods of heating and subsequent cooling are shown in Fig. 7. Superimposed on the data points are the best-fit curves based on Eq. (5). The heating curves for both the y and z axes are similar. The fitted values of ΔT_{ss} and τ for all measure-

Table 3
Calculated values for increased number of layers

	η ($\text{mT m}^{-1} \text{ A}^{-1}$)			L (μH)		
	GX	GY	GZ	GX	GY	GZ
XYZYX	11.7	10.3	11.0	121	114	97
XYZYXXYZ	15.1	13.4	18.9	419	396	1064
XYZYXXZY	15.1	13.1	19.7	419	444	891
XYZYXXYZ ^a	14.7	13.7	18.9	445	363	1064
XYZYXZXY	14.7	13.1	20.1	445	444	701
XYZYXXYZ	14.4	13.7	19.7	488	363	891
XYZYXXZY	14.4	13.4	20.1	488	396	701

^a The most efficiency balanced example.

Table 4
Calculated and measured electrical values

	L (μH)			R ($\text{m}\Omega$)		
	Calculated	1 kHz	10 kHz	Calculated	1 kHz	10 kHz
Layer 1	12	11.9	11.8	67	90	96
Layer 2	23	23.0	23.0	104	124	131
Layer 3	97	98.0	97.5	200	238	260
Layer 4	60	61.0	61.0	201	262	273
Layer 5	98	101.0	101.0	275	323	345
X axis	121	126.3	126.1	342	412	429
Y axis	114	118.4	118.2	305	380	400
Z axis	97	100.0	99.7	200	238	254

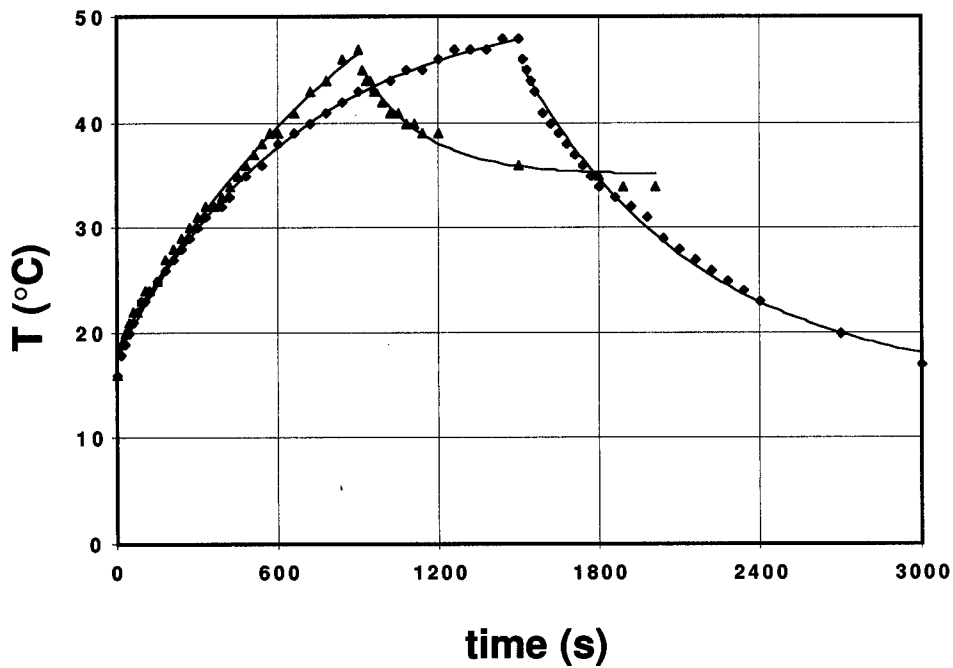


Fig. 7. Measured temperatures at the region of highest wire density on the X-axis over time while passing 20 A dc through the X-axis alone. Heating was stopped when the maximum temperature increased by 30°C. The solid triangles represent the response with no cooling applied, whereas the solid diamonds represent the response with 4 l min⁻¹ water cooling. The solid lines are the results of fitting Eq. (5) to the measured data. The response of the Y and Z axes were similar.

Table 5
Fit results for heating measurements

Axis	Flow (l min ⁻¹)	Phase	ΔT_{ss} (°C)	τ (s)	k_h (°C W ⁻¹)
X	0	Heating	49	1053	0.297
		Cooling	-11	236	
	4	Heating	34	666	0.204
		Cooling	-31	665	
Y	0	Heating	51	786	0.332
		Cooling	-17	317	
	4	Heating	40	631	0.274
		Cooling	-31	649	
Z	0	Heating	37	768	0.388
		Cooling	-17	253	
	4	Heating	21	430	0.228
		Cooling	-22	656	

ments are summarized in Table 5. Table 5 also includes the corresponding values of k_h , as defined in Eq. (6). The data indicates that the steady-state heating parameter, k_h , is decreased by an average of 46% with the addition of water cooling (46, 21 and 70% for the X , Y and Z axes, respectively). The heating time constant (τ_h) is always found to decrease with cooling, whereas the cooling time constant (τ_c) always increases (although only very slightly for z axis). The most important effect of cooling is evident by noting the difference in steady-state temperature decreases. These results suggest that without cooling the steady-state temperature of the coil, after the cessation of power, approaches on average approximately 15°C above ambient temperature. Of course, eventually the coil would cool to room temperature; however, this full return to baseline temperatures required several hours. In practice, this would represent a serious limitation to coil performance. The addition of cooling removed this limitation and resulted in cooling times very close to heating times (noted by the similarity between τ_h and τ_c with the inclusion of cooling).

Fig. 8 shows the number of single shot EPI images that can be collected at maximum rate (as determined by the pulse sequence) during each burst period as a function of FOV for each axis. The x axis allows the collection of the largest number of images before each dead time (14% more than the z axis, 57% more than the y axis); however, this is balanced by the fact that the entire burst plus dead time sequence can be repeated every 430 s when using the z axis, as compared

to 631 and 666 s for the Y and X axes, respectively. In practice, burst mode can not be accomplished repeatedly without water cooling because of the extremely long time required for the coil to cool.

Fig. 9 shows a plot of the minimum single shot EPI repetition time as a function of the readout FOV for the three individual axes. The z axis allows an imaging rate approximately two times that of y and 50% more than x over the full range of FOVs, while the x axis demonstrates an approximate 30% speed advantage compared to y . A similar analysis can be used to compare the performance of each axis with and without water cooling and it was found that the z axis showed a decrease in minimum TR by 70%, the x axis by 45%, and the y axis by 20% with the use of water cooling.

4.4. Preliminary imaging

Fig. 10 shows the first image collected, on the 4T scanner, of the grid phantom as described in Section 3. It was collected with a gradient-recalled echo sequence with the following parameters, TR, 50 ms; TE, 4 ms; flip angle, 11°; matrix size, 256 × 256; FOV, 4 × 4 cm²; slice thickness, 2 mm; and number of averages, 16. The image in the figure is cropped to highlight the grid phantom of size 26 mm square. A box was overlaid on the image to indicate a region of 1 cm² that corresponds to the size of the ROU over which less than 1% deviation was expected. It can be seen that no obvious image distortions occur over that area. The measured

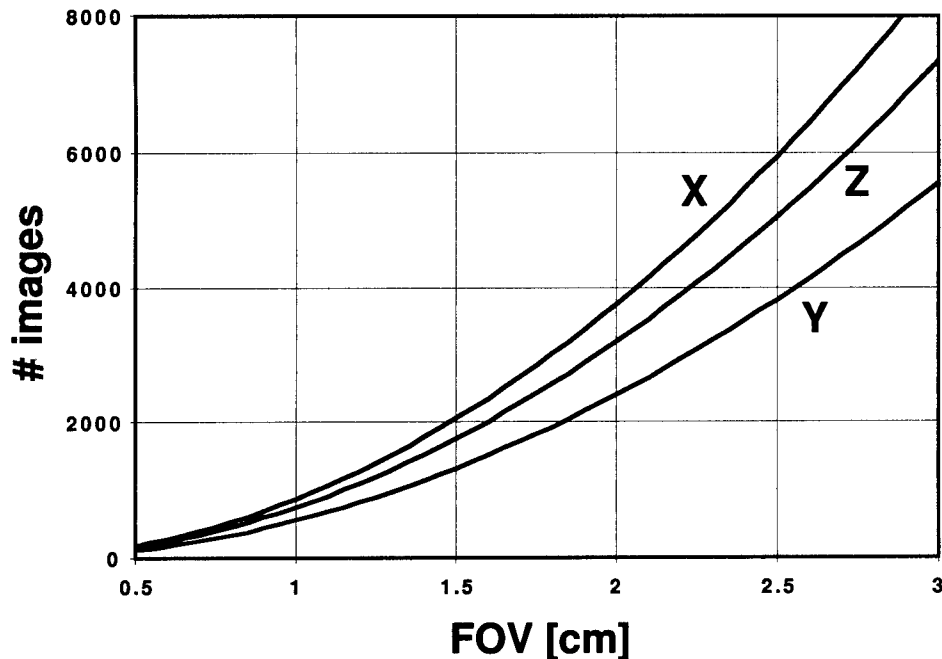


Fig. 8. The number of single-shot EPI images ($N_p = 64$, $N_r = 64$, SW = 500 kHz, $V = 400$ V, $\Delta T_b = \Delta T_{rms} = 10^\circ\text{C}$, water cooling = 4 l min⁻¹, and η_r , L_r , R and k_h are equal to the values for each axis as given in Tables 2 and 4) that can be collected by each axis during a single burst period, as a function of FOV.

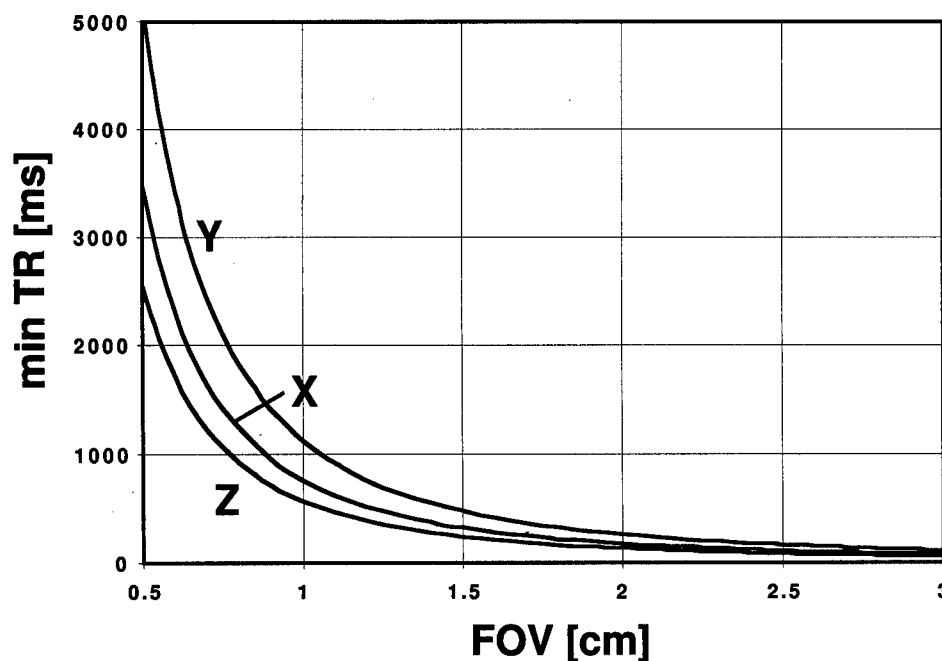


Fig. 9. The minimum TR for a single shot EPI image ($N_p = 64$, $N_r = 64$, SW = 500 kHz, $V = 400$ V, $\Delta T_c = 10^\circ\text{C}$, water cooling = 4 l min^{-1} , and η_r , L_r , R and k_h equal to the values for each axis as given in Tables 2 and 4) for continuous mode scanning, as a function of the FOV.

efficiencies at the coil center for the X, Y and Z axes were found to be 11.8, 11.0, and 11.2 $\text{m}^{-1} \text{A}^{-1}$, respectively.

Fig. 11 shows a proton-density-weighted fast spin-echo image of an excised rat brain collected on a GE 1.5T Signa scanner. The sequence parameters were, TR, 3500 ms; effective TE, 18 ms; matrix size, 256×192 ; FOV, $1.7 \times 1.7 \text{ cm}^2$; slice thickness, 0.625 mm; echo train length, 4; and number of averages, 24. Total imaging time was approximately 1 h and 15 min. The in-plane resolution was $65 \times 87 \mu\text{m}^2$. The smooth, round outer surface of the brain is due to the 14-mm diameter tube into which the brain was placed during imaging. The sample was in air during imaging and there are two obvious artifacts (one near the top centre of the image, another near the bottom centre, slightly left) that we believe are caused by air pockets in the sample. Another similar artifact can be seen within the brain on the right side of the image. This is also a susceptibility artifact, although not likely due to a trapped air bubble due to its location. Both these artifacts can be reduced by decreasing the echo spacing in the sequence; furthermore, a more careful sample preparation (e.g. suspending the sample in saline solution) would likely prevent air bubble formation.

5. Discussion

Although there are numerous publications describing gradient coil designs [18], descriptions of coils cus-

tomized for small animal imaging are lacking. A body of work does exist for the development of very small, extremely high strength designs for use in NMR diffusion studies in very small (typically less than 1 cm^3) samples [19–28]. The coils described for these studies are typically one or two axis designs and hence are not

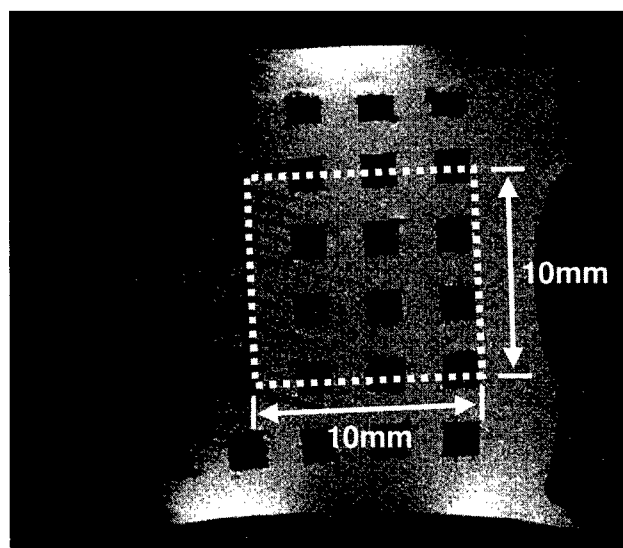


Fig. 10. Gradient echo image of a grid phantom collected with the mouse gradient coil at 4 T. Imaging parameters were TR/TE/flip angle, 50/4 ms/11°; number of averages, 16; FOV, $4 \times 4 \text{ cm}^2$; matrix, 256×256 ; resolution, $156 \times 156 \times 2000 \mu\text{m}^3$; collection time, 3 min 24 s. The image has been cropped to highlight the phantom of size $26 \times 26 \text{ mm}^2$. Dark squares within the grid are $2 \times 2 \text{ mm}^2$ and are separated by 2 mm. The dashed box represents an area $10 \times 10 \text{ mm}^2$ within which the gradient is uniform to better than 1%.

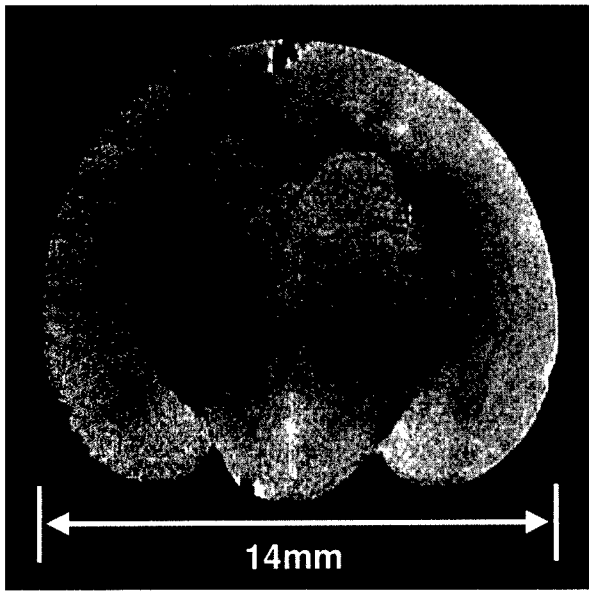


Fig. 11. Fast spin echo image of an excised rat brain collected at 1.5 T. Imaging parameters were, TR/TE, 3500/18 ms; echo train length, 4; number of averages, 24; FOV, $17 \times 17 \text{ mm}^2$; matrix, 256×192 ; resolution, $65 \times 87 \times 625 \mu\text{m}^3$; collection time, 1 h 15 min. The smooth, round outer surface of the brain is due to the 14-mm diameter tube into which the brain was placed during imaging.

suitable for microimaging studies [23–25]. Quadrupolar designs (for at most two axes) are the most popular in these applications [20,21,24–26,29,33,34], assuming that there is adequate room within the scanner bore for transverse coil alignment. Coils in the transverse orientation [29,33–35] and on-axis [30–32,36] have been reported that are large enough to be used for small animal studies while multilayer designs for single axes have been reported [14,27,28] for diffusion NMR studies, but there are no complete three-axis designs considered that apply multilayer design methods, nor have multilayer methods been applied to the design of coils large enough for small animal imaging. A survey of the literature indicates that the strongest on-axis gradient coils in use for mouse imaging produce gradients of up to 1000 mT m^{-1} [10]. The trade-offs between coil aspect ratio, imaging ROU, and coil performance have not been demonstrated previously, nor have the special considerations that must be taken into account to properly govern coil heating.

This paper demonstrates that the primary challenges to attaining the extreme gradient strength and speed requirements that accompany mouse imaging pertain to the thermal response of the coil. To alleviate the extreme heating problems predicted by the thermal scaling laws described in Section 2, efforts were made on several fronts to manage the temperature of the coil while maintaining the required strength and inductance. A multilayer approach was taken that allowed high efficiency designs with reduced winding density. The lower winding densities are vital in that they allow

larger cross-section wire to be used, thereby reducing resistance significantly. We developed fabrication methods that allow the use of rectangular Litz wire. The rectangular wire was wound on end, increasing the available copper area by a factor of four (for the particular wire used in this coil) as compared to square wire wound to the same density. The Litz wire was chosen for its resistance characteristics over the 1–10 kHz range, expected to be the dominant operating frequency for the high speed image acquisitions intended for this coil. All these measures contributed to reducing the resistance of each axis. Going further, we sought to reduce the temperature increases for any input power through the addition of water cooling. The epoxy used for the fabrication of the coil was specially chosen to have the highest thermal conductivity available. This maximized the transfer of heat from the wires to the water cooling layer. The potting procedure was specially developed to avoid the inclusion of any heat insulating materials that would hinder the removal of heat from the coil. Thermocouples were built into the coil to allow both the characterization of the heating response of the coil under various circumstances, as well as to facilitate continual thermal monitoring during operation. Finally, efforts were made to model the heating effects of two very different modes of operation. These efforts all contributed to attaining optimal performance with the final coil.

It is instructive to compare the thermal response as predicted by the initial scaling laws to the measured response of the completed coil. From Fig. 1, we saw that if the hypothetical body coil were simply scaled down to mouse size, a winding density of 16 cm^{-1} would have been required to achieve the target efficiency. The corresponding steady-state temperature increase at 100 A was seen to be approximately 25000° , clearly not feasible and underlining the need for a different approach. From the heating measurements made and summarized in Table 5, we saw that for an input rms current of 20 A, the average steady-state temperature increase of the axes was 32°C . Scaling this result to an input rms current of 100 A, the temperature increase of the axes is predicted to be approximately 800°C . Although still a much larger temperature increase, than tolerable, it is more than 30 times lower than that predicted by the uniform scaling law. This substantial improvement is due to the many steps taken to limit the heating of this mouse coil.

The results indicate that this coil design can be operated successfully in both burst and continuous modes. In different applications, both will be necessary and it is important to be able to optimize the coil duty cycle for either case. Burst mode will allow the collection of hundreds of successive $< 1 \text{ cm}$ FOV single shot 64×64 EPI images at rates of approximately 1 s^{-1} . These are of course the extreme cases with respect to

FOV. Practical operation will undoubtedly involve some compromise between FOV and imaging rates; the theory and results described in this paper can be applied to optimize the coil operation under any circumstance.

There are several ways that the coil design presented here can be improved. Firstly, minimum power instead of minimum inductance methods could have been applied and this may have reduced the axis resistance at the cost of increased inductance [18]. The reason that this was not done was that we have not implemented minimum power methods in conjunction with current constraints, as we have with CCMI. The use of current constraints is important to control the final size of the coil and was necessary to achieve the side-hole aperture specified. Secondly, more elegant minimum power 3D methods for multilayer gradient coils have been reported recently [14,28]. It would be possible to utilize those techniques to obtain an equivalent strength coil with lower resistance in place of simply scaling the size of a single design to the different layers. Again, this is expected to be at the cost of increased inductance. We focused primarily on improved fabrication methods to minimize the thermal problems in this coil; however, because temperature response remains the dominant limiting factor in this coil, additional design optimization efforts are warranted. Finally, active magnetic shielding could have been included in this design to improve its performance in small bore MRI systems.

6. Conclusion

This paper has demonstrated the most important issues in the design and operation of a very high strength gradient coil for small microscopy. With current generation amplifier hardware, this coil allows the collection of single shot EPI images at 6 mm FOV and 94 μm isotropic voxels at imaging rates exceeding 50 s^{-1} . This coil should allow improvements in in-vivo MR microscopy for a diverse range of applications.

Acknowledgements

The authors would like to thank Carl Gazdzinski for his work in analyzing the designs required to visualize the coil parameter space. We also thank Dr Greg Stanisz for his assistance with the heating measurements and Dr R.M. Henkelman for his valuable suggestions. BAC was supported by a Natural Sciences and Engineering Research Council of Canada postgraduate scholarship. This work was supported in part by the Medical Research Council of Canada grant GR-14973.

Appendix A. Derivation of rms current during EPI sequence

The rms current during a single shot EPI sequence is derived as follows. Starting from the fundamental relationship between readout FOV, SW, and G :

$$\frac{\gamma}{2\pi} G_r \text{FOV}_r = \text{SW} \quad (\text{A1})$$

and applying the definition of the readout gradient efficiency (η_r):

$$G_r = \eta_r I_r \quad (\text{A2})$$

yields an expression for the maximum current required during the readout portion of each gradient lobe (I_r):

$$I_r = \frac{2\pi}{\gamma} \frac{\text{SW}}{\eta_r \text{FOV}_r}, \quad (\text{A3})$$

where FOV_r is the extent of the field of view in the direction of the readout axis. The mean-square current over a complete, single shot EPI application is given by the integral of the squared current over a single readout lobe, multiplied by the number of lobes (equal to the number of phase encode lines required, N_p), divided by the sequence repetition time (TR):

$$I_{\text{rms}}^2 = \frac{N_p}{\text{TR}} \left(2 \int_0^{\tau_r} I(t)^2 dt + I_r^2 T_r \right). \quad (\text{A4})$$

The first term is the contribution from both ramps of each lobe, whereas the second term expresses the contribution from the flat-top portion of the lobe. T_r is the duration of the flat-top, given by the number of readout points collected, divided by the readout sweep width:

$$T_r = \frac{N_r}{\text{SW}}. \quad (\text{A5})$$

For a trapezoidal readout lobe, the linear current variation over a rise time of τ_r is:

$$I(t) = \frac{I_r}{\tau_r} t. \quad (\text{A6})$$

The rise time can be expressed as:

$$\tau_r = \frac{L_r}{V} I_r \quad (\text{A7})$$

where L_r is the inductance of the readout gradient axis, V the applied voltage, and I_r the required readout current. Integrating Eq. (A4) and combining the result with Eqs. (A5), (A6) and (A7) yields:

$$I_{\text{rms}}^2 = \frac{N_p}{\text{TR}} \left\{ \left(\frac{I_r}{\tau_r} \right)^2 \frac{2\tau_r^3}{3} + I_r^2 \frac{N_r}{\text{SW}} \right\}. \quad (\text{A8})$$

Simplifying the resulting expression to obtain the rms current gives:

$$I_{\text{rms}} = I_r \sqrt{\frac{N_p}{\text{TR}} \left\{ \frac{2 L_r}{3 V} I_r + \frac{N_r}{\text{SW}} \right\}^{1/2}} \quad (\text{A9})$$

Finally, Eqs. (A3) and (A9) are combined to yield an expression for the rms current as a function of the pulse sequence, readout gradient coil, and amplifier parameters:

$$I_{\text{rms}} = \frac{2\pi\text{SW}}{\gamma\eta_r\text{FOV}_r} \sqrt{\frac{N_p}{\text{TR}} \left\{ \frac{2 L_r}{3 V} \frac{2\pi\text{SW}}{\gamma\eta_r\text{FOV}_r} + \frac{N_r}{\text{SW}} \right\}^{1/2}} \quad (\text{A.10})$$

The above expression is specific to trapezoidal EPI readout trains.

References

- [1] Chien KR. Genes and physiology: molecular physiology in genetically engineered animals. *J Clin Invest* 1996;97:901–9.
- [2] Johnson GA, Benveniste H, Engelhardt RT, Qiu H, Hedlund LW. Magnetic resonance microscopy in basic studies of brain structure and function. *Ann New York Acad Sci* 1997;820:139–48.
- [3] Lester DS, Lyon RC, McGregor GN, Engelhardt RT, Schmued LC, Johnson GA, Johannessen JN. 3-Dimensional visualization of lesions in rat brain using magnetic resonance imaging microscopy. *Neuroreport* 1999;10:737–41.
- [4] Kooy RF, Reyniers E, Verhoye M, Sijbers J, Bakker CE, Oostra BA, Willems PJ, Van Der Linden A. Neuroanatomy of the fragile X knockout mouse brain studied using high resolution magnetic resonance imaging. *Eur J Hum Genet* 1999;7:526–32.
- [5] Grune M, Pillekamp F, Schwindt W, Hoehn M. Gradient echo time dependence and quantitative parameter maps for somatosensory activation in rats at 7 T. *Magn Reson Med* 1999;42:118–26.
- [6] Fenycs DA, Narayana PA. In vivo diffusion tensor imaging of rat spinal cord with echo planar imaging. *Magn Reson Med* 1999;42:300–6.
- [7] Smith BR, Shattuck MD, Hedlund LW, Johnson GA. Time-course imaging of rat embryos in utero with magnetic resonance microscopy. *Magn Reson Med* 1998;39:673–7.
- [8] Arnder L, Zhou X, Cofer G, Hedlund LW, Johnson GA. Magnetic resonance microscopy of the rat carotid artery at 300 MHz. *Invest Radiol* 1994;29:822–6.
- [9] Rose SE, Wilson SJ, Zelaya FO, Crozier S, Doddrell DM. High resolution high field rodent cardiac imaging with flow enhancement suppression. *Magn Reson Imaging* 1994;12:1183–90.
- [10] Slawson SE, Roman BB, Williams DS, Koretsky AP. Cardiac MRI of the normal and hypertrophied mouse heart. *Magn Reson Med* 1998;39:980–7.
- [11] Callaghan PT. Principles of Nuclear Magnetic Resonance Microscopy. New York: Oxford University Press, 1991.
- [12] Cremillieux Y, Ding S, Dunn JF. High-resolution in vivo measurements of transverse relaxation times in rats at 7 T. *Magn Reson Med* 1998;39:285–90.
- [13] Meyerand ME, Cremillieux Y, Wadghiri YZ, Azzawi A, Hoopes PJ, Dunn JF. In vivo gradient echo microimaging of rodent spinal cord at 7 T. *Magn Reson Med* 1998;40:789–91.
- [14] Bowtell R, Robyr P. Multilayer gradient coil design. *J Magn Reson* 1998;131:286–94.
- [15] Chu KC, Rutt BK. MR gradient coil heat dissipation. *Magn Reson Med* 1995;34:125–32.
- [16] Chronik BA, Rutt BK. Constrained length minimum inductance gradient coil design. *Magn Reson Med* 1998;39:270–8.
- [17] Reitz JR, Milford FJ, Christy RW. Foundations of Electromagnetic Theory, 4th ed. New York: Addison-Wesley, 1989.
- [18] Turner R. Gradient coil design: a review of methods. *Magn Reson Imaging* 1993;11:902–20.
- [19] Parker RS, Zupancic I, Pirs J. Coil system to produce orthogonal, linear magnetic field gradients. *J Phys E: Sci Instrum* 1973;6:899–900.
- [20] Webster DS, Marsden KH. Improved apparatus for the NMR measurement of self-diffusion coefficients using pulsed field gradients. *Rev Sci Instrum* 1974;45:1232–4.
- [21] Odberg G, Odberg L. On the use of a quadrupole coil for NMR spin-echo diffusion studies. *J Magn Reson* 1974;16:342–7.
- [22] Zupancic I, Pirs J. Coils producing a magnetic field gradient for diffusion measurements with NMR. *J Phys E: Sci Instrum* 1976;9:79–80.
- [23] Cho ZH, Ahn CB, Juh SC, Lee HK, Jacobs RE, Lee S, Yi JH, Jo JM. Nuclear magnetic resonance microscopy with 4- μm resolution: theoretical study and experiment results. *Med Phys* 1988;15:815–24.
- [24] Schoeniger JS, Blackband SJ. The design and construction of a NMR microscopy probe. *J Magn Reson B* 1994;104:127–34.
- [25] Rofe CJ, Van Noort J, Back PJ, Callaghan PT. NMR microscopy using large, pulsed magnetic field gradients. *J Magn Reson B* 1995;108:125–36.
- [26] Oishi O, Miyajima S. New PFG NMR spectrometer with a rotatable quadrupole coil for the measurement of an anisotropic self-diffusion coefficient tensor. *J Magn Reson A* 1996;123:64–71.
- [27] Snaar JE, Robyr P, Bowtell R. Strong gradients for spatially resolved diffusion measurements. *Magn Reson Imaging* 1998;16:587–91.
- [28] Bowtell R, Crozier S, Beck B, Blackband S. Multi-layer transverse gradient coils. In: Proceedings of the ISMRM, 1999:468.
- [29] Bowtell R, Mansfield P. Screened coil designs for NMR imaging in magnets with transverse field geometry. *Meas Sci Tech* 1990;1:431–9.
- [30] Wong EC, Jesmanowicz AJ, Hyde JS. High-resolution, short echo time MR imaging of the fingers and wrist with a local gradient coil. *Radiology* 1991;181:393–7.
- [31] Eccles CD, Crozier S, Roffman W, Doddrell DM, Back P, Callaghan PT. Practical aspects of shielded gradient coil design for localised in vivo NMR spectroscopy and small-scale imaging. *Magn Reson Imaging* 1994;12:621–30.
- [32] Blackband SJ, Chakrabarti I, Gibbs P, Buckley DL, Horsman A. Fingers: three-dimensional MR imaging and angiography with a local gradient coil. *Radiology* 1994;190:895–9.
- [33] Chu KC, Rutt BK. Quadrupole gradient coil design and optimization: a printed circuit board approach. *Magn Reson Med* 1994;31:652–9.
- [34] O'Dell WG, Schoeniger JS, Blackband SJ, McVeigh ER. A modified quadrupole gradient set for use in high resolution MRI tagging. *Magn Reson Med* 1994;32:246–50.
- [35] Maier CF, Chu KC, Chronik BA, Rutt BK. A novel transverse gradient coil design for high-resolution MR imaging. *Magn Reson Med* 1995;34:604–11.
- [36] Doty FD. MRI gradient coil optimization. In: Blumler P, Blumich B, Botto R, Fukushima E, editors. Spatially Resolved Magnetic Resonance: Methods, Materials, Medicine, Biology, Rheology, Geology, Ecology, Hardware. New York: Wiley-VCH, 1999:647–74.

Appendix II

The pulse sequence and the analysis program developed for this grant were tested with two substances – water and acetone - whose diffusion coefficients are well documented. The theoretical and experimentally determined results are shown below for diffusion encoding along six unique directions:

Water:

The theoretical value of the diffusion coefficient of water is between 2.12×10^{-3} and $2.63 \times 10^{-3} \text{ mm}^2/\text{s}$ at 21.7 C° .

<u>Diffusion Encoding Direction</u>	<u>Diffusion Coefficient (mm^2/s)</u>
xy	$2.03 \pm 0.02 \times 10^{-3}$
-xy	$2.10 \pm 0.09 \times 10^{-3}$
xz	$2.08 \pm 0.10 \times 10^{-3}$
-xz	$1.97 \pm 0.06 \times 10^{-3}$
yz	$2.07 \pm 0.04 \times 10^{-3}$
-yz	$2.07 \pm 0.11 \times 10^{-3}$

Acetone:

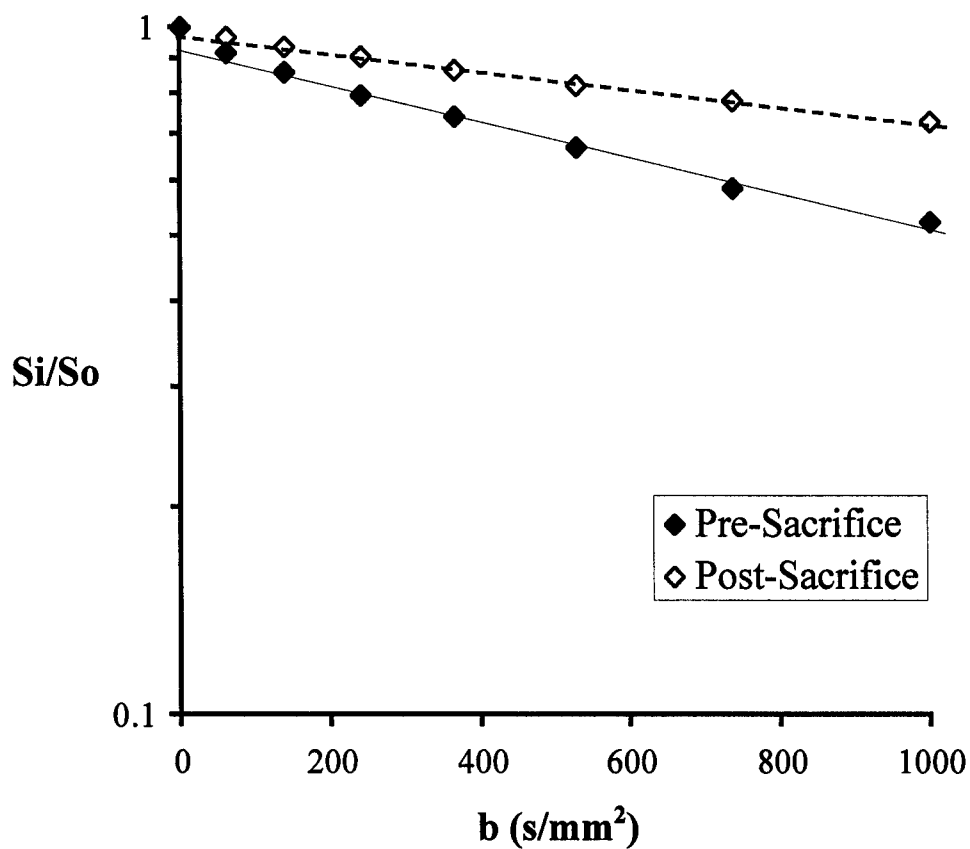
The theoretical value of the diffusion coefficient of acetone is between 3.88×10^{-3} and $4.43 \times 10^{-3} \text{ mm}^2/\text{s}$ at 21.7 C° .

<u>Diffusion Encoding Direction</u>	<u>Diffusion Coefficient (mm^2/s)</u>
xy	$4.47 \pm 0.04 \times 10^{-3}$
-xy	$4.59 \pm 0.05 \times 10^{-3}$
xz	$4.62 \pm 0.03 \times 10^{-3}$
-xz	$4.30 \pm 0.05 \times 10^{-3}$
yz	$4.47 \pm 0.06 \times 10^{-3}$
-yz	$4.55 \pm 0.06 \times 10^{-3}$

Reference: Bammer R, *et al.* Diffusion-weighted imaging with navigated interleaved echo-planar imaging and a conventional gradient system. *Radiology* **211**:799 (1999).

Appendix III

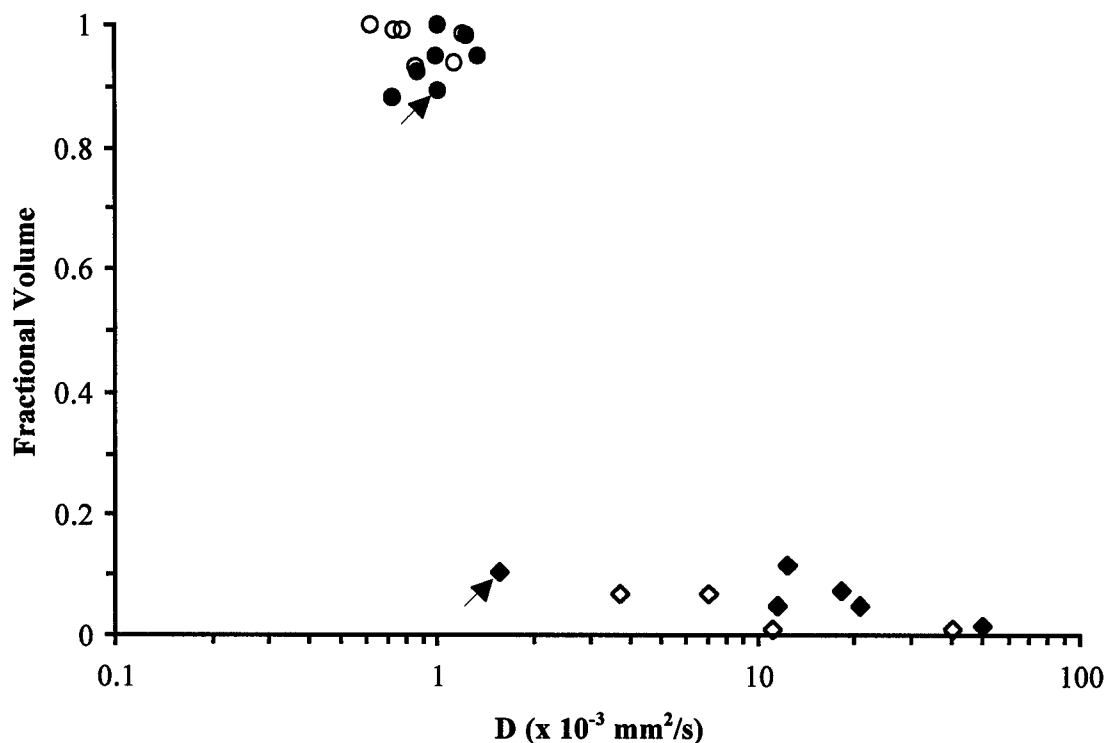
Figure 1



Diffusion decay curves obtained from one tumour pre-sacrifice (closed symbols) and post-sacrifice (open symbols). The straight lines show the deviation of the curves from mono-exponential behaviour for the pre-sacrifice (solid line) and post-sacrifice (dashed line) cases. Note that for both cases, the decay curves are at least bi-exponential and that the post-sacrifice curve does not decay as quickly at the outset as the pre-sacrifice curve.

Appendix III

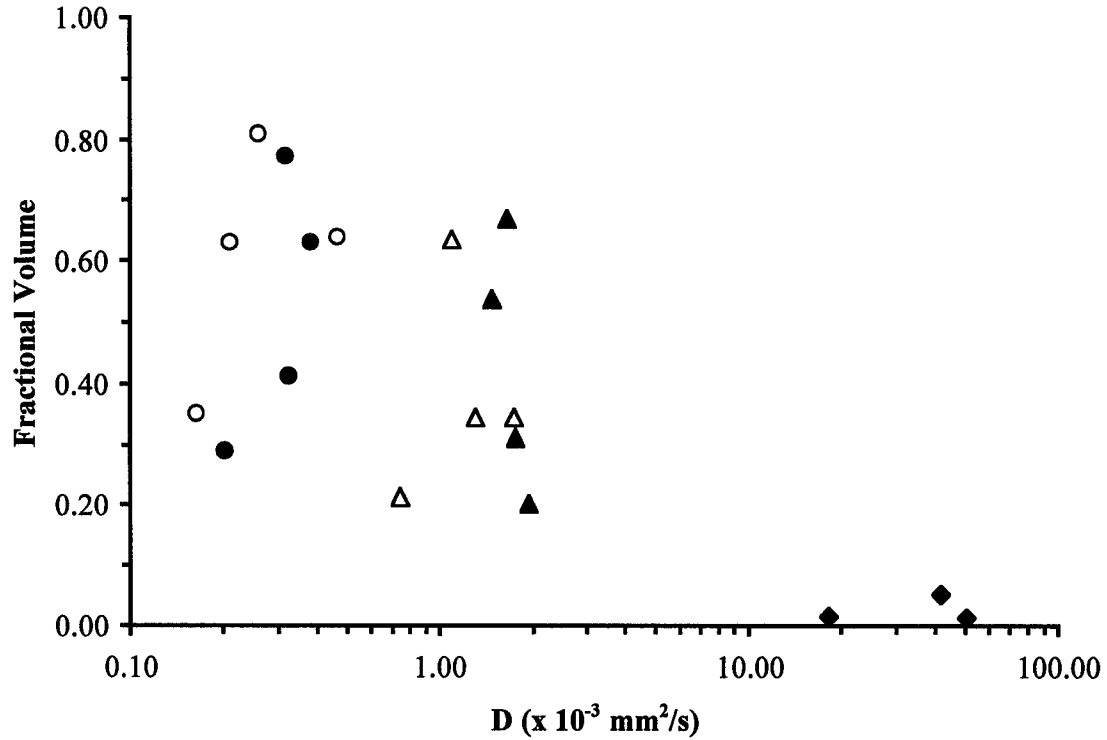
Figure 2



Plot of the diffusion coefficients obtained from decay curves with a maximum b-value of 1000 s/mm². Diffusion coefficients were derived from decay curves acquired from seven tumours pre-sacrifice (closed symbols) and post-sacrifice (open symbols). In five of the seven cases, both a low diffusion coefficient (circles) and a high diffusion coefficient (diamonds) were found for the pre-sacrifice curves. In one case, only a low diffusion coefficient was found, and in another case, two coefficients were found but they were not well differentiated (low and high coefficients are marked above by arrows). Post-sacrifice, two diffusion coefficients were still found in four of the decay curves, but the higher coefficient was now intermediate between the pre-sacrifice, high and low coefficients. These results suggested that a third diffusion rate is present.

Appendix III

Figure 3



Plot of the diffusion coefficients obtained from decay curves with a maximum b-value of 5000 s/mm². Diffusion coefficients were derived from decay curves acquired from four tumours pre-sacrifice (closed symbols) and post-sacrifice (open symbols). In three of the four cases, three diffusion coefficients were found for the pre-sacrifice curves - low (circles), intermediate (triangles) and high diffusion coefficients (diamonds). In one case, only low and intermediate diffusion coefficients were found. Post-sacrifice, low and intermediate diffusion coefficients were still seen, but the higher coefficient was absent in each case.



DEPARTMENT OF THE ARMY
US ARMY MEDICAL RESEARCH AND MATERIEL COMMAND
504 SCOTT STREET
FORT DETRICK, MARYLAND 21702-5012

REPLY TO
ATTENTION OF:

MCMR-RMI-S (70-1y)

28 July 03

MEMORANDUM FOR Administrator, Defense Technical Information
Center (DTIC-OCA), 8725 John J. Kingman Road, Fort Belvoir,
VA 22060-6218

SUBJECT: Request Change in Distribution Statement

1. The U.S. Army Medical Research and Materiel Command has reexamined the need for the limitation assigned to technical reports written for this Command. Request the limited distribution statement for the enclosed accession numbers be changed to "Approved for public release; distribution unlimited." These reports should be released to the National Technical Information Service.

2. Point of contact for this request is Ms. Kristin Morrow at DSN 343-7327 or by e-mail at Kristin.Morrow@det.amedd.army.mil.

FOR THE COMMANDER:

Encl


PHYLLIS M. RINEHART
Deputy Chief of Staff for
Information Management

ADB233865	ADB264750
ADB265530	ADB282776
ADB244706	ADB286264
ADB285843	ADB260563
ADB240902	ADB277918
ADB264038	ADB286365
ADB285885	ADB275327
ADB274458	ADB286736
ADB285735	ADB286137
ADB286597	ADB286146
ADB285707	ADB286100
ADB274521	ADB286266
ADB259955	ADB286308
ADB274793	ADB285832
ADB285914	
ADB260288	
ADB254419	
ADB282347	
ADB286860	
ADB262052	
ADB286348	
ADB264839	
ADB275123	
ADB286590	
ADB264002	
ADB281670	
ADB281622	
ADB263720	
ADB285876	
ADB262660	
ADB282191	
ADB283518	
ADB285797	
ADB269339	
ADB264584	
ADB282777	
ADB286185	
ADB262261	
ADB282896	
ADB286247	
ADB286127	
ADB274629	
ADB284370	
ADB264652	
ADB281790	
ADB286578	